MASTERARBEIT | MASTER'S THESIS

Titel | Title

Characterizing the chemical reactivity and biological activity of a catalytic metallodrug by mass spectrometry

verfasst von | submitted by

Sofie Damian BSc

angestrebter akademischer Grad | in partial fulfilment of the requirements for the degree of

Master of Science (MSc)

Wien | Vienna, 2025

Studienkennzahl lt. Studienblatt | Degree programme code as it appears on the student record sheet:	UA 066 862
Studienrichtung lt. Studienblatt | Degree programme as it appears on the student record sheet:	Masterstudium Chemie
Betreut von | Supervisor:	Assoz. Prof. Dr. Samuel Meier-Menches

Acknowledgements

First and foremost, I would like to thank my supervisor Sam, for the invaluable guidance and support throughout the course of my thesis. During this time, I was able to learn an incredible amount from him. It has been a privilege to complete my master's thesis under the supervision of such a dedicated mentor.

I would also like to express my gratitude to Andrea, for sharing her important and valuable knowledge with us master's students, particularly regarding the timsTOF and Perseus, as well as for the enjoyable and entertaining lunchtime conversations.

My sincere thanks go as well to Thomas, who was always available to help with any problem and somehow always had a solution ready. Thanks to him we (almost) never lost our nerves, no matter how hopeless our samples might have looked at times.

A special thank you goes to my laminar and spheroid partner, Valentina, with whom every experiment was a pleasure. I would happily and without hesitation do another hundred MTTs and sample processing experiments with you!

I would also like to thank the entire Meier-Menches and Gerner research groups, as well as my fellow master's students, for creating the most pleasant and supportive working atmosphere I could have imagined. I am very grateful for every bit of help and for all the shared knowledge from other areas of bioanalytical chemistry.

Furthermore, I would like to thank my boyfriend Tommy for his endless support, love and patience even during challenging moments. You always knew how to lift me up and motivate me to keep going.

And finally, I want to thank my parents Ana and Marinel and my brother Sergio for always believing in me and supporting me throughout my life.

Abstract

This Master thesis focuses on the characterization of an investigational iridium(III) metallodrug (**Ir1**) with respect to its chemical reactivity and biological activity in the colorectal cancer cell line SW480. The present study was motivated by the growing interest in transition metal complexes enabling catalytic reaction in cells. To investigate the catalytic mechanism of hydride transfers of **Ir1**, an interaction study was performed with the reactive aldehyde 4-hydroxynonenal (4-HNE) and several hydride/deuteride donors in a time-dependent manner by liquid chromatography-tandem mass spectrometry (LC-MS/MS). The consumption of 4-HNE over 20 hours was observed in the presence of **Ir1** and hydride/deuteride donors, accompanied by the formation of the corresponding alcohol products. Viability assays were then conducted with **Ir1** in SW480 cancer cells to determine concentrations to inhibit growth from 10% to 90% (IC_{10}-IC_{90}). SW480 cells were treated with **Ir1** for 24 hours in a dose-dependent manner, whole cell lysates were generated and after proteolytic digestion, the samples were analyzed by nano-flow LC-MS/MS using a timsTOF Pro mass spectrometer. The resulting proteomic data revealed a clear dose dependent response. Particularly, intermediate doses (IC_{40}–IC_{60}) induced proteins associated with oxidative stress, mitochondrial remodeling, and cell cycle regulation. Apoptosis related processes became more dominant at higher doses (IC_{70}-IC_{90}), including Bax associated pathways. Among others, **Ir1** influenced three major biological processes: stress response signaling (NRF2 and heat shock pathways), apoptosis, and metabolic remodeling (Glycolysis, Pentose-Phosphate Pathway, and One-carbon metabolism) that may be indicative of the transfer hydrogenation capability of **Ir1**. By acting as a reducing agent, **Ir1** was supposed to have antagonistic effects with arsenic trioxide (ATO), which induces reactive aldehyde species. Indeed, an antagonism of this combination was verified in viability assays with a combination index of around 1.1. Proteomic profiling of the combination treatment significantly upregulated 306 proteins, compared to the single agent treatments. Functional annotation confirmed the association of these proteins with unfolded protein response, heat shock mechanisms, and apoptotic processes. Finally, oxidative stress induction was assessed using the 2',7'-dichlorodihydrofluorescein diacetate (DCFH-DA) assay in SW480 cancer cells after acute treatment with **Ir1** and ATO, as well as their combination. ATO did not induce peroxide-based reactive oxygen species (ROS), whereas **Ir1** and the **Ir1**+ATO combination were potent ROS inducers. Cell-free studies revealed that these signals were not due to cellular ROS generation but to a direct chemical reaction between **Ir1** and the DCFH-DA dye, which seems to serve as a hydride donor. Thus, the increase in DCFH-mediated fluorescence represents direct evidence of the catalytic activity of **Ir1** in SW480 cells. The findings of this work contribute to a deeper understanding of how catalytic metallodrugs can reshape cellular proteomes and stress networks.

Zusammenfassung

Diese Masterarbeit untersucht die Charakterisierung eines Iridium(III)-Metallwirkstoffs (**Ir1**) hinsichtlich seiner chemischen Reaktivität und biologischen Aktivität in der kolorektalen Krebszelllinie SW480. Das Projekt wurde durch das zunehmende Interesse an Übergangsmetallkomplexen motiviert, die katalytische Reaktionen in Zellen ermöglichen. Zur Aufklärung des katalytischen Hydridtransfer-Mechanismus von **Ir1** wurde eine Interaktionsstudie mit dem reaktiven Aldehyd 4-Hydroxynonenal (4-HNE) sowie verschiedenen Hydrid/Deuterid-Donoren durchgeführt. Mittels LC-MS/MS wurde zeitabhängig gezeigt, dass 4-HNE in Anwesenheit von **Ir1** und Hydrid/Deuterid-Donoren über 20 Stunden verbraucht wurde, begleitet von der Bildung der entsprechenden Alkohole. Anschließend wurden Viabilitätsassays in SW480-Zellen zur Bestimmung der IC_{10}–IC_{90}-Werte durchgeführt. Nach 24-stündiger dosisabhängiger **Ir1**-Behandlung wurden Gesamtzelllysate generiert, proteolytisch verdaut und mittels Nano-LC-MS/MS auf einem timsTOF Pro analysiert. Die Proteomdaten zeigten eine klare dosisabhängige Antwort. Mittlere Konzentrationen (IC_{40}–IC_{60}) induzierten Proteine, die mit oxidativem Stress, mitochondrialer Umgestaltung und Zellzyklusregulation verknüpft sind. Höhere Konzentrationen (IC_{70}–IC_{90}) aktivierten vermehrt Apoptose bezogene Prozesse, einschließlich Bax-assoziierter Signalwege. **Ir1** beeinflusste insbesondere drei zentrale biologische Prozesse: Stressantwort-Signalwege (NRF2- und Hitzeschockmechanismen), Apoptose sowie metabolische Umprogrammierung (Glykolyse, Pentosephosphatweg, Ein-Kohlenstoff-Stoffwechsel). Diese Veränderungen deuten auf die Transferhydrierungsfähigkeit von **Ir1** hin. Da **Ir1** als Reduktionsmittel wirkt, wurde ein antagonistischer Effekt mit Arsentrioxid (ATO), das reaktive Aldehyde erzeugt, erwartet. Viabilitätsassays bestätigten diesen Antagonismus mit einem Kombinationsindex von ca. 1.1. Die proteomische Analyse der **Ir1**+ATO-Kombination zeigte eine signifikante Hochregulierung von 306 Proteinen im Vergleich zu den Einzelbehandlungen. Funktionelle Annotation ordnete diese Proteine der Ungefaltete-Protein-Antwort, Hitzeschockmechanismen und apoptotischen Prozessen zu. Die Induktion oxidativen Stresses wurde mithilfe des DCFH-DA-Assays nach akuter Behandlung mit **Ir1**, ATO und ihrer Kombination untersucht. ATO erzeugte keine Peroxid basierten ROS, während **Ir1** und die Kombination starke ROS-Signale lieferten. Zellfreie Experimente zeigten jedoch, dass diese Signale nicht auf zelluläre ROS zurückzuführen sind, sondern auf eine direkte chemische Reaktion zwischen **Ir1** und dem DCFH-DA-Farbstoff, der offenbar als Hydriddonor fungiert. Der Anstieg der DCFH-Fluoreszenz stellt somit einen direkten Nachweis der katalytischen Aktivität von **Ir1** in SW480-Zellen dar. Die Ergebnisse dieser Arbeit erweitern das Verständnis darüber, wie katalytische Metallwirkstoffe zelluläre Proteome und Stressnetzwerke beeinflussen können.

Table of contents

1. Introduction

1.1 Iridium-based anticancer therapy

Metal-based chemotherapeutics are an actively explored research area in anticancer drug discovery.[1] While platinum agents such as cisplatin have historically dominated clinical practice, their continuing success is only limited due to resistance development and adverse effects.[2] This has motivated the search for alternative transition metal complexes with anticancer properties following different modes of action, among which iridium compounds have emerged as a promising compound familiy.[2,3]

Iridium distinguishes itself from other members of the platinum group metals, such as ruthenium, rhodium, palladium and osmium by offering a unique combination of broad functional-group tolerance, high aqueous stability and kinetic inertness. These features allow the formation of highly stable metallic coordination complexes, especially in the +3 oxidation state, which is more stable in biological environments compared to the +1 oxidation state.[2]

The coordination motif of iridium(III) is partially responsible for its therapeutic potential. The metal readily adopts coordination numbers of 4 and 6 and shows a strong preference for nitrogen-donor ligands. These structural properties help with the construction of organoiridium complexes with various bioactive ligands, which in turn enables fine-tuning of chemical reactivity and kinetic stability in biological systems.[2] Iridium complexes do not rely on a single cytotoxic mechanism, instead they operate through a variety of pathways, including catalytic interference with cellular redox homeostasis, direct interaction with protein kinases, and regulation of non-apoptotic signaling. Some Ir(III) species target DNA, while others primarily act at the mitochondrial level, inducing apoptosis through the generation of reactive oxygen species (ROS).[2] The redox-mediated mechanism is particularly characteristic. By disturbing cellular oxidation-reduction balance through electron transfer processes, Ir-complexes function as catalytic metallodrugs.[4] Chloroiridium(III) compounds, for example, have been described as redox-active agents capable of triggering apoptosis via mitochondrial ROS production, while exhibiting relatively low systemic toxicity compared to platinum based drugs.[2]

Furthermore, Ir(III) complexes can be used for theranostic approaches. Their photophysical and luminescence properties, including high quantum yields, long emission lifetimes, large Stokes shifts, remarkable photostability, and cell permeability make them suitable not only for treatment but also for diagnostic purposes.[3,5] Theranostic agents are expected to meet several criteria such as allowing real-time monitoring of therapeutic responses, enabling patient-specific treatment adjustments, and ideally combining diagnosis and therapy in early-stage disease.[5] Ir-complexes are particularly attractive in this regard for photodynamic therapy (PDT) and photothermal therapy (PTT). In PDT, photosensitizers generate ROS upon irradiation, thereby inducing localized cell damage. In contrast, PTT relies on the conversion of light energy into heat, destroying cancer cells by thermal ablation.[5,6] By integrating these diagnostic and therapeutic

modalities, Ir-based complexes represent a promising step towards highly selective and personalized oncology treatments.[5]

The catalytic redox chemistry of Ir-complexes has been further explored in the context of their ability to accept hydrides from cofactors such as NADH, thereby linking their activity directly to ROS production.[7] Cyclopentadienyl ligands, in particular, dramatically accelerate ligand exchange rates, enhancing catalytic turnover by several orders of magnitude.[7] This feature not only differentiates organoiridium complexes from platinum-based drugs but also provides a molecular explanation for their distinct mechanism of action. Rather than acting as stoichiometric DNA binders, iridium complexes behave more like intracellular catalysts, sustaining cytotoxicity activity by perpetuating redox imbalance within cancer cells.[8]

Building on this idea, iridium-based small molecule intracellular metal catalysts (SIMCats) have been proposed, as artificial analogues of natural reductase enzymes. These SIMCats are capable of detoxifying reactive aldehyde species (RASP), cytotoxic byproducts generated through lipid peroxidation, carbohydrate oxidation, lysine deamination, drug metabolism or environmental exposure. Among these, α,β-unsaturated aldehydes such as 4-hydroxy-2-nonenal (4-HNE) are especially harmful due to their ability to form non-specific covalent adducts with proteins and nucleic acids, contributing to cellular dysfunction and disease progression.[8,9]

In healthy cells, endogenous defense mechanisms, including aldehyde dehydrogenases (ALDH), aldo-keto reductases (AKR), and glutathione conjugation pathways, normally limit RASP accumulation.[8,10] However, these systems are hampered under conditions of oxidative stress, which are common in cancer and other disorders.[8,11] Ir-SIMCats mimic enzymatic detoxification by catalyzing the transfer of hydrides from donors such as formate or NADH to aldehyde acceptors, converting them into less toxic alcohols. As long as they remain catalytically active inside the cell, SIMCats can provide long-lasting protection against aldehyde-induced damage. Their activity correlates with cellular uptake and lipophilicity, with certain complexes showing higher efficiency due to increased membrane permeability.[8] Strategies for detoxification of aldehyde-associated diseases are shown in **Figure 1**. SIMCats are promising because they enable the catalytic conversion of toxic aldehydes into alcohols.[12]

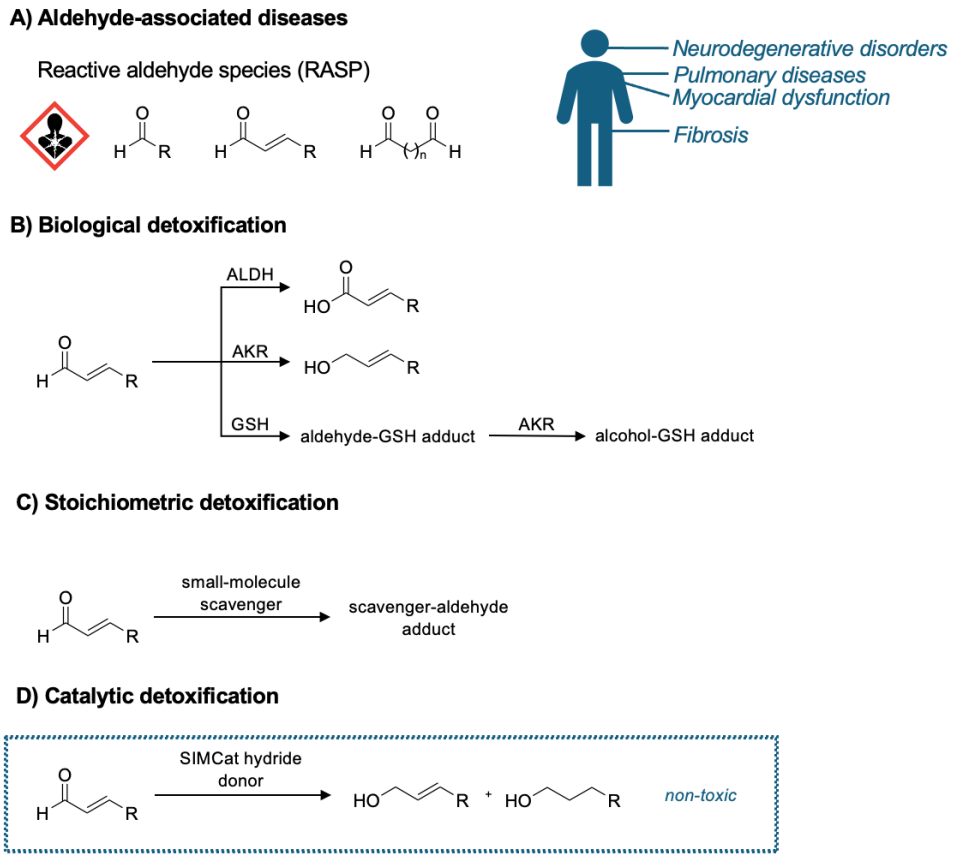

***Figure 1**: Strategies for detoxification of aldehyde-associated diseases (A) covering biological (B), stoichiometric (C) and catalytic (D) approaches. Scheme adapted from Jana et al. [8]*

1.2 Arsenic trioxide as anticancer agent

In parallel to the advances in iridium chemistry, arsenic trioxide (As_2O_3, ATO) has regained attention as an effective anticancer drug in clinical practice. In fact, ATO represents one of the few clinically approved metal(loid)s for cancer therapy.

Historically infamous as a toxic agent, also nicknamed the "king of poison", ATO has been successfully repurposed for the treatment of acute promyelocytic leukemia (APL).[13] It represents a rare subtype of leukemia, which arises from chromosomal translocation, in which segments of the two chromosomes 15 and 17, t(15;17)(q22;q21), are exchanged, resulting in the promyelocytic leukemia protein – α retinoic acid receptor (PML-RARα) fusion protein.[14] This genetic alteration disrupts the normal maturation of white blood cells, making them unable to use retinoic acid (vitamin A). Consequently, patients with APL are typically treated with retinoids, compounds derived from vitamin A, that can restore differentiation capacity.[15]

In clinical use, ATO is typically administered intravenously at doses of 0.15-0.3 mg/kg. In combination with all trans retinoic acid (ATRA), it has yielded impressive outcomes, with three-year disease-free survival rates exceeding 96% and long-term relapse rates lower than conventional chemotherapy regimens.[13] However, extended exposure to arsenic-based compounds may contribute to the development of secondary diseases

including kidney cancer, cirrhosis and various neurological disorders.[13] Its mechanism of action is multifaceted, involving both extrinsic and intrinsic apoptotic pathways. The extrinsic pathway is initiated by the binding of death ligands such as FasL or TNF by their corresponding receptors, leading to caspase activation and DNA fragmentation. In the intrinsic pathway, ATO disrupts redox balance by elevating ROS levels and depleting intracellular glutathione (GSH). This oxidative stress damages mitochondrial integrity, promotes the release of cytochrome C and activates pro-apoptotic Bcl-2 family proteins such as Bac and Bid, ultimately driving apoptosis.[13,16]

Beyond apoptosis, ATO has demonstrated anti-angiogenic effects, reported by Sun et al.[17] They found that ATO induces the expression of a transcription factor called FoxO3a, which leads to anti-angiogenic effects. However, despite these promising mechanisms, the clinical translation of ATO beyond hematological malignancies remains limited. Its rapid renal clearance short plasma half-life, and high systemic toxicity, restrict its application in solid tumors.[13]

To overcome these challenges, nanomedicine-based drug delivery systems have been developed to encapsulate ATO within macroscopic carriers, such as liposomes or nanoparticles, amongst others. These strategies prolong ATO circulation, enhance tumor accumulation and reduce off-target toxicity.[13] Furthermore, synergistic effects have been reported when ATO is combined with other chemotherapeutic agents, including vincristine, vinblastine and lithium chloride, indicating combination therapies as a viable strategy for enhancing efficacy while minimizing dose-dependent side effects.[13]

1.3 Synergism and Antagonism within combination therapies

The combined use of drugs in cancer therapy has long been recognized as a strategy to improve treatment efficacy, overcome resistance and reduce the toxic burden of individual agents. However, interactions between drugs are complex and can lead to outcomes that deviate substantially from a simple additive effect. These interactions are generally classified as antagonistic, additive or synergistic.[18,19] In this thesis, the **Ir1**-ATO combination was selected to demonstrate that the pairing of the reducing agent (**Ir1**) with an oxidizing agent (ATO) can lead to antagonistic effects in cells. The motivation for this experiment was therefore mechanistic in nature rather than aimed at identifying a clinically relevant combination therapy.

1.3.1 Additive and antagonistic effect

Additive or non-interactive combinations are those in which the effect of two compounds equal the sum of their individual actions. Antagonistic interactions yield an outcome that is lower than expected, Conversely, antagonism is often seen as a drawback. However, antagonistic interactions may reduce the selective pressure that drives the emergence of resistance, as demonstrated in microbial systems where antibiotic combinations delayed resistance evolution.[20,21] In many cases, the second drug still provides a therapeutic

contribution, albeit smaller than what would be expected from additivity. Only in extreme cases, described as “super-antagonism”, is a drug combination counterproductive.[20]

1.3.2 Synergistic effect

Synergy is especially attractive in oncology because it allows for the reduction of drug dosages to reduce systemic toxicity, while maintaining or even increasing antitumor potency. Synergistic mechanisms can involve complementary drug action, prevention of counteractive processes, or mechanisms whereby one drug enhances the uptake or bioavailability of another.[19] Positive interactions of this kind are also referred to as potentiation, as they enhance therapeutic activity beyond what either compound would achieve alone.[18] Synergistic drug interactions in oncology can be conceptually linked to synthetic lethality.[22] While synergy refers to pharmacological combinations that enhance therapeutic efficacy beyond additive effects, synthetic lethality describes genetic or molecular interactions where simultaneous perturbation of two pathways leads to cell death.[23] This principle has been successfully exploited in cancer therapy, for example with PARP inhibitors in BRCA-mutated tumors, representing a clinically validated case of synergy through synthetic lethality.[24]

1.3.3 Reference models

Evaluating whether a combination is synergistic or antagonistic requires the use of reference models. These models provide a “null hypothesis” of no interaction with which the obtained experimental data can be compared.[18,25] The most established frameworks include Bliss independence and Loewe additivity, both of which rest on distinct biological and mathematical assumptions.[18] To evaluate drug synergy or antagonism, the combination index (CI) needs to be determined. It is calculated from viability curves or drug toxicity. A CI <1 is considered as an antagonistic effect, and a CI >1 as a synergistic effect.[21]

Bliss independence

Bliss independence treats drugs as if they act independently on separate targets. It calculates effects as probabilities between 0 and 1, assuming exponential dose-response relationships and no interference between drugs. This model is useful when the mechanisms of action are distinct and independent, but its applicability is limited to cases where effects can be accurately described probabilistically. Bliss also struggles in so-called “sham mixture” scenarios, where the assumption of independence is violated.[19,25] The mathematical framework for Bliss independence can be seen in **Equation 1** and **Equation 2.**

Equation 1: *Calculation of the effect E_{AB} given by doses a and b for Bliss independence.[25]*

$$E_{AB} = E_A + E_B * (1 - E_A)$$

Equation 2: *Calculation of the combination index for Bliss Independence.*

$$CI = \frac{E_A + E_B + E_A E_B}{E_{AB}}$$

Loewe additivity

In contrast, the Loewe additivity model is dose-effect based and defines additivity through the concept of isoboles. It operates under the "sham mixture" principle, assuming that a drug cannot interact with itself, and under the dose equivalence principle, which postulates that a dose of drug A can be substituted by an equivalent dose of drug B and vice versa to yield the same effect (a_b or b_a in **Equation 3**). This requires constant potency ratios and identical maximal effects across drugs.[19,25] In practice, these assumptions are often difficult to meet. Potency ratios are rarely constant, and obtaining precise dose-response curves is both resource-intensive and prone to error. Furthermore, many drugs deviate from the straight-line isobole expected by the Loewe model, particularly when dose-response relationships are complex.[25] The Loewe additivity mathematical framework is noted in **Equation 3** and **Equation 4**.

Equation 3: *Calculation of the effect E_{AB} given by doses a and b for Loewe additivity.(a = actual dose of substance A, b = actual dose of substance B, a_b = equivalent dose of substance A that corresponds to the effect of drug B, b_a = equivalent dose of substance B that corresponds to the effect of drug A).* [25]

$$E_{AB} = E_A(a + a_b) = E_B(b + b_a)$$

Equation 4: *Calculation of the combination index for Loewe additivity.*[25]

$$CI = \frac{a}{A} + \frac{b}{B}$$

Zero Interaction Potency

Recognizing the limitations from Bliss and Loewe, researchers have developed a hybrid approach called Zero Interaction Potency (ZIP). ZIP integrates aspects of both Bliss and Loewe by focusing on changes in the shape and potency of dose-response curves. The underlying assumption is that if two drugs truly do not interact, the combined curve should remain unaltered in terms of slope and half-maximal effective concentration (EC_{50}). By comparing experimental outcomes against this expectation, ZIP can identify both synergistic and antagonistic interactions across different concentration ranges. Its utility is evident in high-throughput combination screenings, where it enables the systematic detection of various interaction types. However, the model's accuracy depends on the quality of the dose-response data. Poor curve fitting, deviations from expected log-logistic behavior, or unreliable experimental results can compromise the validity of ZIP analyses.[27] The underlying equation for calculating the effect E_{AB} for the ZIP model can be seen in **Equation 5**.

Equation 5: *Calculation of the effect E_{AB} given by doses a and b for ZIP.*[25,27]

$$E_{AB} = \frac{(\frac{[A]}{EC_{50,A}})^{\lambda A}}{1+(\frac{[A]}{EC_{50,A}})^{\lambda A}} + \frac{(\frac{[B]}{EC_{50,B}})^{\lambda B}}{1+(\frac{[B]}{EC_{50,B}})^{\lambda B}} - \frac{(\frac{[A]}{EC_{50,A}})^{\lambda A}}{1+(\frac{[A]}{EC_{50,A}})^{\lambda A}} * \frac{(\frac{[B]}{EC_{50,B}})^{\lambda B}}{1+(\frac{[B]}{EC_{50,B}})^{\lambda B}}$$

A persistent challenge in this field is the inconsistency of model outcomes. In some cases, Bliss may classify a combination as synergistic while Loewe identifies it as antagonistic. To address this problem, Tang et al.[28] proposed a distinction between “strong synergy”, where both models agree, and “weak synergy”, where only one model supports the interaction.[18] This approach reduces interpretive bias and provides a more refined categorization of combination effects. Nevertheless, it is generally agreed that all synergy models should be treated primarily as hypothesis-generating tools, guiding the prioritization of drug combinations for further validation rather than serving as definitive proof of interaction.[18,25]

Beyond model-specific considerations, the broader biological context of drug interactions must also be acknowledged. Modern cancer therapies such as surgery, chemotherapy, radiotherapy, or combinations thereof, still face the challenge of resistance and severe side effects. Combination therapies are pursued to overcome those issues, but the evaluation of synergy and antagonism in oncology is often inconsistent. Often results are being interpreted as synergistic based on simple experimental comparisons without applying mathematical frameworks. This practice risks misclassification and oversimplification[25], underscoring the need for more rigorous application of reference models in preclinical research.

Recent contributions have also emphasized that the outcome of drug combination is influenced by network topology and the complexity of cellular signaling.[29] Drugs acting within the same pathway or overlapping networks may produce unexpected antagonism, while those acting on complementary or compensatory mechanisms may yield synergy. This complexity further complicates the task of standardizing models and interpreting results. In response, computational frameworks have been developed to optimize therapy by integrating diverse models, in some cases even transforming predictions of antagonism into opportunities for therapeutic synergy.[30]

1.4 Nano liquid chromatography-tandem mass spectrometry

The application of nano-flow high-performance liquid chromatography coupled to tandem mass spectrometry (nanoHPLC-MS/MS) is essential in modern proteomics. Recent advances in mass spectrometry have considerably enhanced analytical capabilities and the depth of the accessible and quantifiable proteome. Developments such as the Orbitrap mass analyzer and novel fragmentation methods have enabled new experimental strategies in proteomic investigations.[31,32]

In principle, mass spectrometry determines the m/z ratio of ions in the gas phase. For this purpose, the instrument comprises three main components: the ion source, the mass analyzer and the detector. In the ion

source, molecules are transferred from the liquid into the gas phase and are then ionized. These ions are then separated according to their m/z ratio by the analyzer and subsequently registered by the detector, which quantifies ion abundances for each m/z value.[31]

Because biological samples are complex, chromatographic separation is required prior to MS analysis. In this work, a Dionex3000 nano-HPLC system was employed. Chromatography achieves separation based on differential partitioning of analytes between a stationary and a mobile phase.[33] An important parameter in this context is the injected sample volume, overloading the system can severely impair separation quality. Therefore, the use of minimal sample volume is essential. State-of-the-art nLC platforms are equipped with automated injection modules and splitless pump systems, ensuring reproducible flow rates without solvent loss.[33,34] Additionally, nLC operates with narrow columns and very low flow rates in the sub µL/min range.[33] Overall, nLC has established itself as a highly sensitive and reliable separation method, particularly in proteomics and peptide sequencing, as it enabled the precise analysis of small quantities of analytes.[34]

1.4.1 Ionization

After chromatographic separation, the peptides eluting from the nano-LC column are introduced into the mass spectrometer, where the first essential step is ionization. In the here reported experiments, a timsTOF Pro instrument (Bruker) was used, which uses electrospray ionization (ESI). ESI is particularly suitable for converting biomolecules, including peptides and proteins, into gas-phase ions under mild conditions.[35] As a "soft" ionization method, it generates only limited fragmentation, thereby preserving the molecular structure of the analytes while requiring only small sample amounts for detection.[36]

In the nano-HPLC-ESI setup, analytes pass through a heated capillary into the ionization source, where a high voltage is applied. This produces a fine spray of charged droplets, the polarity of which depends on the applied voltage. As solvent evaporates, the droplets shrink, leading to the release of analyte ions into the gas phase. While intact proteins may remain partially entrapped within nanodroplets, peptides originating from proteolytic digestion are efficiently ionized, facilitating their downstream analysis.[37] The timsTOF Pro uses the "Captive Spray" as an nESI source, which differs considerably from the other nES setups. The creation of a rotational airflow around the Taylor cone promotes efficient movement of ions, allowing high sensitivity even at different nanoflow settings. At the same time, this setup supports a uniformly sustained spray throughout the chromatographic gradient, which contributes to stable and reproducible measurements.[38]

1.4.2 Mass Analyzer

Once ionized, analytes enter the mass analyzer, which separates them according to their m/z ratio.[31] Various analyzer types exist, but this thesis focuses on the time-of-flight (TOF) system. TOF analyzers operate on the principle that ions, accelerated to the same kinetic energy, travel through a drift tube at velocities inversely related to the square root of their mass. Consequently, lighter ions reach the detector more rapidly than

heavier ones. This relationship can be derived from the fundamental expression of kinetic energy (**Equation 6**), which shows the dependence on ion mass, when solved for velocity.[39]

Equation 6: *Formula for the kinetic energy (E).*[39]

$$E = \frac{1}{2} * m * v^2$$

In practice, factors such as differences in ion generation, initial positions and kinetic energy variations can impair resolution and lead to peak broadening.[40] To minimize these effects, modern TOF instruments incorporate reflectrons, which compensate for energy dispersion and improve mass accuracy.[41] Despite these challenges, TOF analyzers offer distinct advantages, including wide mass ranges, high scan speeds and the ability to generate continuous spectra.[40]

1.4.3 Fragmentation technique

For peptide sequencing, fragmentation techniques are essential. The timsTOF Pro system applies parallel accumulation-serial fragmentation (PASEF), a method that allows for rapid MS/MS acquisition for efficient duty cycles. During PASEF, ions are accumulated within the trapped ion mobility spectrometry (TIMS) device and subsequently released in a mobility-dependent sequence. The quadrupole rapidly switches between precursors within a single TIMS scan, enabling highly efficient fragmentation.[42,43]

Fragmentation is achieved via collision-induced dissociation (CID), in which precursor ions undergo energetic collision with neutral gas molecules, leading to peptide bond cleavage and the formation of b/y fragment ions. CID is well established in proteomics and forms the basis of MS/MS.[44] The initial MS1 scan provides information about ion m/z values and intensities, which can be used for quantification and targeted analysis through extracted ion chromatograms (EICs).[45] In the subsequent MS/MS step, fragmentation ions are analyzed to deduce peptide sequences. This approach can be applied in both top-down and bottom-up proteomics.[46]

1.4.4 Detection

The final stage of the process is analyte detection. The detector registers the separated ion and converts the incoming ion stream into a digital signal. Historically, photographic plates were used for this purpose, but modern TOF instruments rely on advanced detectors such as microchannel plates, which provide high sensitivity, fast response times, and accurate signal conversion.[47]

1.5 Proteomics

Proteomics is described as the comprehensive investigation of proteins with respect to their structural and functional properties, providing valuable insights into biological systems.[48] Through this approach, it is aimed to identify and quantify potentially all proteins within a biological sample. Given the heterogeneity of

biological material, a range of methodological strategies is required for quantification, broadly classified into label-based and label-free proteomics.[49] Furthermore, proteomic techniques are useful for characterizing biological responses to drugs and metal-based drug candidates.[50] The present thesis focuses on bottom-up proteomic approaches, in which proteins are enzymatically digested into peptides prior to analysis by LC-MS.[51]

1.5.1 Data acquisition

In proteomics, two main strategies for mass spectrometry-based data acquisition are commonly applied: data-dependent acquisition (DDA) and data-independent acquisition (DIA). In DDA workflows, an initial MS1 survey scan is recorded across a user-defined m/z range. Based on this spectrum, the instrument selects a subset of precursor ions, typically those with the highest intensities for fragmentation in the collision cell. Afterwards, MS2 spectra of the resulting fragments are collected.[52,53] To avoid repeated fragmentation of the same species, already fragmented ions are temporarily placed on an exclusion list. While this strategy ensures broader coverage, a limitation of DDA is that ions of low abundance may not be selected for fragmentation, which can hinder their identification since MS2 information is lacking.[52] In contrast, quantitative information in DDA analyses primarily derives from MS1 intensities.[53] DIA methods, by comparison, aim to overcome such limitations by fragmenting all ions within defined m/z windows across the mass range, but may suffer from drawbacks with respect to false discovery rate calculations.[52]

1.5.2 Label-free proteomics

In contrast to label-based methods, label-free strategies do not require isotopic labeling and are commonly divided into two categories. Therefore, quantification is either based on chromatographic peak intensities or spectral counting. The latter, which estimates protein abundance by the number of peptide-to-spectrum matches (i.e. MS/MS spectra), is rarely applied today due to lower accuracy. The intensity-based approach, by contrast, quantifies peptides through chromatographic peak areas in the mass spectrum, where separation occurs according to peptide hydrophobicity and mass-to-charge (m/z) ratios.[49]

Label-free quantification (LFQ) offers several advantages over isotopic labeling. It enables the comparison of large numbers of samples, is cost-effective, provides a broad dynamic range and eliminates the need for specialized labeling reagents or time-intensive labeling steps.[54] However, since each sample must be measured separately, LFQ can be more time-consuming and the accuracy is generally lower compared to stable isotope-based methods.[55] For successful LFQ experiments, sample preparation workflows and cell culture conditions must be tightly controlled to minimize variance.[56]

2. Aim of this work

Previous studies have demonstrated that an investigational organometallic iridium(III) complex (**Ir1**, **Figure 2**) can catalyze hydride transfer reactions, potentially even within cells,[12] but the cellular consequences of this catalysis remain unclear. Therefore, the aim of this work is to examine the chemical and biological activity of **Ir1** under physiologically relevant conditions and in the SW480 colon carcinoma cell line.

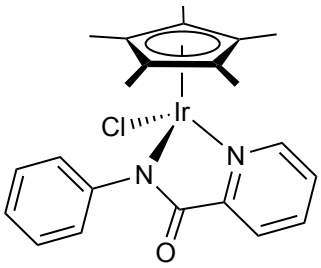

Figure 2: *Chemical structure of Ir1 (sum formula: $C_{22}H_{24}ClIrN_2O$, molecular weight = 559.5 g/mol).*

First, it is aimed to elucidate the mechanism of hydride transfer with hydride/deuteride donors, including nicotinamide adenine dinucleotide hydride (NADH) and formate towards reactive aldehydes, e.g. 4-HNE, under different conditions in a time-dependent manner by HPLC-MS/MS.

Then, viability assays will be performed in order to obtain dose-response curves for proliferation inhibition and for performing a dose-dependent proteomic assay with **Ir1** in SW480 cancer cells. This will enable conclusions about dose-dependent cellular responses and drug effects. Additionally, a combination treatment of **Ir1** and ATO will be investigated with respect to potential synergisms/antagonisms in viability assays and on the proteome level. It is expected that the combination of the reducing **Ir1** and the oxidizing ATO may produce antagonistic effects in cancer cells.

Finally, a 2',7'-dichlorodihydrofluorescein diacetate (DCFH-DA) assay will be performed for the time-dependent detection of reactive oxygen species (ROS) in SW480 cancer cells induced by ATO, **Ir1** and the combination treatment. DCFH is sensitive to the presence of ROS, especially peroxides, and the fluorescent reaction product enables their detection.

Within this thesis, aspects of cell culture, sample preparation, LC-MS data acquisition, and analysis strategies for large datasets will be integrated. Furthermore, fundamental chemical properties of **Ir1** will be related to biological effects in cancer cells.

3. Materials and Methods

3.1 Materials and Devices

3.1.1 Materials

The materials used for this thesis are listed below.

- Cell Medium: Minimum Essential Medium Eagle (MEM) [*Sigma-Aldrich*, LOT: RNBN0625, Cat. No. M4655-500ML] (+50 mL 10% FBS [*gibco*, LOT: B2741830 RP], + 5 mL Pen Strep [Sigma-Aldrich, LOT: 215793]
- Trypsin: StableCell™ Trypsin Solution [*Sigma-Aldrich*]
- Iridium compound was kindly provided by Prof. Dr. Loi Do from the Department of Chemistry, University of Houston (USA): **Ir1** (MW=559.5 g/mol)
- As_2O_3: Arsenic (III) oxide (*Sigma-Aldrich*, CAS-No.: 1327-53-3, LOT: MKBQ6516V, P-code: 1001712465)
- MTT salt: Thiazolyl Blue Tetrazolium Bromide [*Sigma-Aldrich*, CAS-No.: 298-93-1, Source/LOT: MKCS4540, P-code: 1003699373]
- HEPES Buffer: HEPES Ultrapure [*GERBU*, CAS: 7365-45-9, LOT: 170611]
- Guanidine hydrochloride [*Sigma*, CAS: 50-01-1, LOT: SLBX7252, P-code: 102066493]
- SDC-Buffer: Sodium deoxycholate [*Sigma*, CAS: 302-96-4, LOT: BCCD1238, P-code: 102241316]
- Bond-Breaker TCEP Solution [*Thermo* Scientific, Catalogue number: 77720, LOT: WG327380]
- 2M Tris-HCl pH 8.5
- VWR-H2O
- 5 M NaOH for pH adjustment
- DMSO: Dimethyl sulfoxide, puriss. P.a., dried [*Sigma-Aldrich*, CAS: 67-68-5, LOT: STBL0407]
- PBS (sterile)
- For Interaction studies:
    - L-Cysteine *[Aldrich, CAS: 52-90-4, LOT: 1415066, Filling code: 41709041]*
    - L-Histidine *[Fluka, CAS: 71-00-1, LOT: 1272044, Filling code: 13507180]*
    - Pyridoxal phosphate *[ROTH, CAS: 54-47-7, LOT: 1T9H.1]*
    - NADH Disodium salt *[ROTH, CAS: 606-68-8, LOT: AE12.1]*
    - Sodium formate D *[ROTH, CAS: 3996-15-4, LOT: 1L39]*
    - 4-Hydroxynonenal *[Sigma-Aldrich/Merck, CAS: 75899-68-2, LOT: 393204]*
    - Sodium formate [*ROTH*, CAS: 141-53-7, LOT: 393204]

- For DCFH-DA-Assays:
    - Tert-Butyl hydroperoxide solution (TBHP) *[Sigma Aldrich, CAS: 75-91-2, 458, LOT: BCCB8820, 458139-25 mL]*
    - Opti-MEM (Reduced Serum Medium) supplemented with +1% FCS (*Serana*) *[gibco, LOT: 2566871]*

- Hank's Balanced Salt Solution (HBSS) *[Sigma Aldrich]*
- DCFH-DA: 2.5 mM stock solution kindly provided by the Jakupec Group, Institute of Inorganic Chemistry, University of Vienna.

- **Composition of different buffers/solutions**
  - *Table 1: Composition of PBS buffer (pH = 7.4).*

Compound	**Concentration [mM]**
NaCl	137
Na_2HPO_4	2.70
KCl	10.0
KH_2PO_4	1.80
Water	-

  - *Table 2: Composition of 100 mL BCA-A reagent for protein quantification (pH = 11.25).*

Compound	**Concentration [mM]**
Bicinchoninic acid	29.00
Sodium carbonate	188.7
Sodium bicarbonate	113.0
Sodium tartrate	8.250
Water	-

  - *Table 3: Composition of 10 mL BCA-B reagent for protein quantification.*

Compound	**Amount**
Copper sulfate x 5 H_2O	0.5 g
Water	10 mL

  - *Table 4: Composition of 10 mL SDC lysis buffer.*

Compound	**Prepare for 10 mL**
SDC	0.4 g
Tris-HCl (2 M, pH = 8.5)	500 µL
Water	9500 µL

- *Table 5: Composition of SDB-RPS loading & wash buffer 1 for Cleanup.*

Compound	Amount [%vol/vol]
Trifluoroacetic acid	1
Isopropanol	99

- *Table 6: Table 7: Composition of SDB-RPS loading & wash buffer 2 for Cleanup.*

Compound	Amount [%vol/vol]
VWR water	94.8
Acetonitrile	5
Trifluoroacetic acid	0.2

- *Table 7: Composition of SDB-RPS elution buffer.*

Compound	Amount [%vol/vol]
Acetonitrile	59.7
VWR water	39.8
NH_4OH	0.5

- *Table 8: Composition of MS loading buffer.*

Compound	Amount [%vol/vol]
Trifluoroacetic acid	0.3
Acetonitrile	2
VWR water	97.7

3.1.2 Devices

The devices used for this master's thesis can be seen below.

- Centrifuge: Thermo Scientific: Heraeus Megafuge 16R Centrifuge
- Water quench: KISS: huber
- Cell counter: DeNovix Cell Drop BF (Brightfield Cell Counter)
- Photometer for MTT assays: Thermo Scientific: Multiskan GO
- Incubator: Thermo Scientific: Heracell 150i, CO2 incubator
- Waste: Integra Vacusafe
- pH meter: inoLab WTW Series Terminal 740

- Ultrasonicator: Bandelin Sonorex Digital 10 P
- Ultrasonic Stick: Bandelin electronic, Device for settings: Bandelin Sonoplus
- Eppendorf shaker: eppendorf ThermoMixer C
- Eppendorf vials centrifuges: Fisher Scientific accuSpin Micro 17, eppendorf Cenrtrifuge 5425 R
- speedvac: GeneVac miVac Duo concentrator
- Autosampler: Thermo scientific Dionex UltiMate 3000 RS Autosampled UHPLC+ focused
- LC: Thermo Scientific: Dionex UltiMate 3000 RSCLnano System
- MS: bruker timsTOF Pro (powered by PASEF)
- Microscope: ZEISS Primo Vert with AxioCamERc5s
- Microscope software for visualizing: ZEN (blue editicion), 2006-2011 Carl Zeiss MicroImaging
- Plate reading software: SkanIt RE for Multiskan GO 3.2
- Used software: Perseus 1.6.14, Skyline (64 bit), GraphPadPrism 8.0.1, ChemDraw 22.2.0
- Used websites: string-db.org, davidbioinformatics.nih.gov, synergyfinder.org

3.2 Cell-free interaction study

In the course of the interaction study, various compounds were combined in a cell-free environment using Eppendorf vials (eppis) and analyzed by uHPLC-MS/MS at six different time points (0 h, 4 h, 8 h, 12 h, 16 h, and 20 h) to monitor the temporal evolution of different species, including hydride donors, aldehydes, **Ir1** as a hydride transfer promoter, and amino acids involved in deactivation.

3.2.1 Experimental settings

For the evaluation of the seven different conditions, the compounds were dissolved in water (**Table 9**) and then combined in predetermined ratios (**Table 10**). **Ir1** was used catalytically at 10 mol% with respect to the reagents.

Table 9: *End concentrations of the compounds used for the interaction study.*

Compound	End Concentration
Ir1	50 µM
HNE+Py	500 µM
Cys+His	500 µM
NADH	2 mM
HCOONa	2 mM
DCOONa	2 mM

Table 10: *Interaction study conditions and reaction combinations (Con = Control, Rxn = Reaction, Deact = Deactivation, P.i. = Pre-incubate **Ir1** and Cys+His in H_2O for 24 h then add the rest).*

Con A	Compound	HNE + Py	NADH	H_2O			**V_{end}**
	Volume [µL]	20	20	160			200
Con B	Compound	HNE + Py	HCOONa	H_2O			
	Volume [µL]	20	20	160			200
Rxn A	Compound	HNE + Py	NADH	H_2O	Ir1		
	Volume [µL]	20	20	140	20		200
Rxn B	Compound	HNE + Py	HCOONa	H_2O	Ir1		
	Volume [µL]	20	20	140	20		200
Rxn C	Compound	HNE + Py	DCOONa	H_2O	Ir1		
	Volume [µL]	20	20	140	20		200
Deact A	Compound	HNE + Py	HCOONa	H_2O	Ir1	Cys + His	
	Volume [µL]	20	20	120	20	20	200
Deact B	Compound	HNE + Py	HCOONa	H_2O	Ir1	Cys + His	
P.i.	Volume [µL]	20	20	120	20	20	200

3.2.2 LC-MS/MS parameters

Chromatographic separation was carried out on a Thermo Scientific™ Vanquish™ UHPLC system equipped with a Kinetex® C18 column (2.6 µM XB-C18, 100 Å, 150 x 2.1 mm; Phenomenex Inc.). The mobile phase A consisted of water containing 0.2% formic acid (FA), while mobile phase B was composed of methanol with 0.2% FA. Each sample was analyzed for 5.5 min, with a column temperature of 25 °C and an injection volume of 5 µL.

Mass spectrometric detection was conducted using a Q Exactive™ HF Orbitrap (Thermo Fisher Scientific) equipped with a HESI source operating in both positive and negative ionization modes. The spray voltage was set to ± 3.2 kV, and the capillary temperature to 350 °C. Auxiliary gas and sheath gas were adjusted to 20 a.u. and 60 a.u., respectively. Full MS scans were recorded within an m/z range of 115-800 at a resolution of 45,000 (at m/z 200). Fragment ions were subsequently analyzed at the MS2 level with a resolution of 30,000 (at m/z 200). Xcalibur software was used to control the instrument.

3.2.3 Data evaluation

The received data was analyzed and evaluated using *Skyline*. For this purpose, it was necessary to select the reactants and potential product molecules. Based on this information and the corresponding chemical formulas, the selected species could be tracked across all samples. The chosen molecules, along with their chemical formulas and precursor adducts (**Table 11**) were imported into *Skyline* as a precursor list.

Table 11: *Precursor list of the interaction study for Skyline.*

Molecule name	Chemical formula	Adduct
NADH	$C_{21}H_{29}N_7O_{14}P_2$	[M+H]
NAD+	$C_{21}H_{28}N_7O_{14}P_2$	[M]+
4-HNE	$C_9H_{16}O_2$	[M+H]
4-HNE (I, +2)	$C_9H_{18}O_2$	[M+H]
4-HNE (II, +4)	$C_9H_{20}O_2$	[M+H]
4-HNE-D(I, +3)	$C_9H_{17}O_2H'$	[M+H]
4-HNE-D (II,+6)	$C_9H_{18}O_2H'_2$	[M+H]
4-HNE-D (III, +5)	$C_9H_{19}O_2H'$	[M+H]
Pyridoxalphosphate	$C_8H_{10}NO_6P$	[M+H]
Pyridoxalphosphate (I, +2)	$C_8H_{12}NO_6P$	[M+H]
Pyridoxalphosphate-D(I,+3)	$C_8H_{11}NO_6PH'$	[M+H]
Cysteine	$C_3H_7NO_2S$	[M+H]
Histidine	$C_6H_9N_3O_2$	[M+H]
Ir1	$C_{22}H_{21}ClIrN_2O$	[M+H]
Ir1	$C_{22}H_{21}ClIrN_2O$	[M-Cl]
Ir1 + Cysteine	$C_{25}H_{31}IrN_3O_3S$	[M]+
Ir1 + Histidine	$C_{28}H_{33}N_5O_3$	[M]+

3.3 Cell culture

The cell line used for this master's thesis was the colorectal cancer cell line SW480 (**Figure 3**). The adherent cells were cultured in Minimum MEM supplemented with Earle's salts, L-glutamine, and sodium bicarbonate, and further enriched with 10% fetal bovine serum (FBS) and 1% Penicillin-Streptomycin (PenStrep; 10,000

units penicillin and 10 mg/mL streptomycin, 0.1 µM filtered). SW480 cells were cultured in standard T75 flasks equipped with ventilated caps. All cell-culture procedures were carried out in HERASAFE KS laminar-flow cabinets (Thermo Fisher Scientific), and the cells were incubated in HERACELL 150i CO_2 incubators (Thermo Fisher Scientific) at 37 °C in a humidified atmosphere containing 5% CO_2.

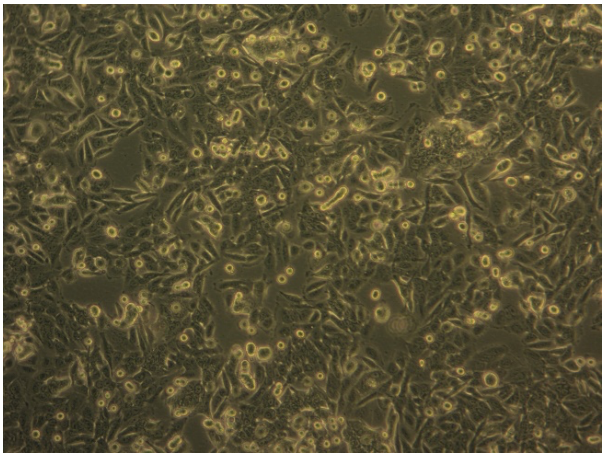

Figure 3: *SW480 colorectal cancer cells in culture under the microscope.*

3.3.1 General procedures

Frozen SW480 cancer cells (passage 15) were thawed, 1 mL of cell suspension was combined with 9 mL of Minimum Essential Medium (MEM) in a 15 mL falcon. The cells were centrifuged at 1100 rpm for 5 minutes at room temperature. Afterwards, the supernatant was lifted off, the cell pellet was suspended in 10 mL MEM and put into a T75 flask. To enable an even distribution of cells at the bottom of the flask, the flask was carefully rotated in an 8-shaped motion. The T75 flask was stored in the incubator at a temperature of 37 °C with 5% CO_2. Once the cells reached a confluence of around 80% and the color of the medium changed from bright pink to orange, the medium was removed, and the flask was washed with 5 mL PBS.

Thereafter, 3 mL of Trypsin-EDTA-Phenol red solution was added to detach the cells from the bottom of the flask, which was incubated at 37 °C with 5% CO_2 for 6 minutes. Trypsin was then deactivated by adding 7 mL MEM. To ensure an ideal suspension, the mixture was pipetted up and down several times and also against the bottom of the flask before transferring it to a 15 mL falcon, which was then centrifuged at 1100 rpm for 5 minutes at room temperature (RT). The supernatant was lifted off and to finish the passaging process, the required amount of the cell suspension was transferred into the T75, which already contained fresh medium to reach a total volume of 10 mL. The flask was put back in the incubator at 37 °C with 5% CO_2. For the final treatment, passage numbers 31 (antagonism study) and 18 (dose-resolved proteomics study) were used.

3.4 Cell counting and Viability Assay

To determine various IC (inhibitory concentration) values, defined as the concentration that inhibits cell growth by a certain percentage compared to untreated controls, viability assays were conducted.

3.4.1 MTT-Assays for preliminary experiments and dose-resolved proteomics

Therefore, the cells were counted after suspending the pellet in MEM following the centrifugation step. Ideally, the cell pellet was suspended in 1 mL medium, 10 µL of the cell suspension was added to 90 µL PBS. To this mixture, 100 µL Trypan-Blue dye was added and 10 µL of the final suspension were used for cell counting. With help of the DeNovix Cell Drop BF (Brightfield Cell Counter) cell counter, it was possible to calculate the needed amount of suspension to receive a dilution with the nutrient solution of 10,000 cells per 96 well-plate. Hundred microliters of the dilution were pipetted in the columns from B3 to G11, the wells from B2 to G2 remained empty. To each well at the edge of the plate, 100 µL PBS was added. Afterwards the plates were incubated for 24 h. Then, the wells from B2 to G11 were loaded with 100 µL of different compound concentrations, which were obtained from serial dilutions of stock solutions of 20 mM **Ir1** and 50 mM ATO. The concentrations were added from lowest to highest, with six replicates each (**Table 12**).

Table 12: *Final concentrations of each column of a 96-well-plate (one plate per compound).*

Well column	Ir1 final concentrations [µM]	ATO final concentrations [µM]
B2 – G2	Blank	Blank
B3 – G3	0	0
B4 – G4	10	2.5
B5 – G5	25	5
B6 – G6	35	10
B7 – G7	40	20
B8 – G8	50	40
B9 – G9	70	80
B10 – G10	80	120
B11 – G11	100	200

The prepared well plates were then incubated for 24 h. Afterwards, 20 µL MTT (3-(4,5-dimethylthioazol-2-yl)-2,5-diphenyltetrazolium bromide) was added to each well and incubated for 3 h. The entire supernatant was lifted off each well, whereby it was important not to withdraw the crystals on the bottom. The crystals were dissolved in 100 µL DMSO and photometrically measured at 570 nm. The desired values for (from IC_{10} up to IC_{90}) were determined using a sigmoidal fitting of the data points in GraphPad Prism (Version 8.0.1).

3.4.2 MTT-Assay for Antagonism study

Three 96 well-plate replicates were conducted with ATO and **Ir1** for the antagonism study. Different concentrations, determined by the single dose-experiments from **3.4.1**, of the mentioned compounds were mixed with one another and resulted in 36 different concentration ratios. **Ir1** was pipetted first and with increasing concentration from row 2 to 8, ATO was added with increasing concentrations from column B to

G (**Figure 4**) The cells were treated for 24 h, after which MTT was added. The resulting formazan crystals were dissolved in DMSO, and absorbance was measured photometrically.

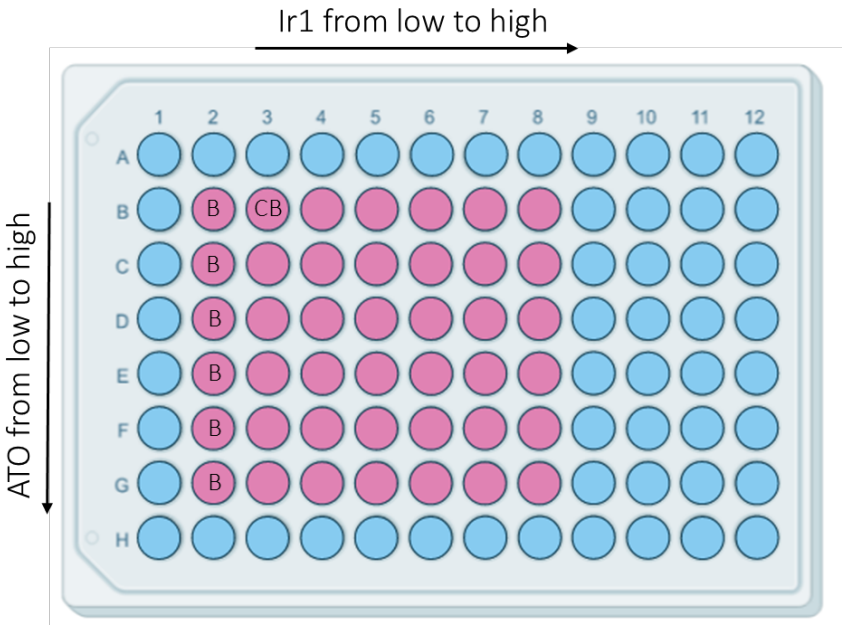

Figure 4: *Visual representation of antagonism MTT pipetting scheme (B=Blank, CB=Cell blank).*

After treating the cells, ensuring that they were first treated with **Ir1** and then with ATO, they were incubated for 24 h at 37 °C and 5% CO_2. On the next day, 20 µL MTT were added to each well. The plates were incubated for another 3 h at previous conditions, the supernatant was lifted off and the crystals were dissolved in 100 µL DMSO per well. They were measured at 570 nm with the photometer, and the results were evaluated via *SynergyFinder* ("start", choose data format: table, upload the according file, Specify response: Inhibition) to evaluate the different mixing ratios. In total, three different antagonism plates were conducted by three different people. Comparing the replicates to the average, the results remain the same. Hence only the data set containing the averages was analyzed further.

3.4.3 DCFH-DA Assay

Cell-containing assay

The DCFH-DA assays were performed on SW480 cancer cells. 25,000 cells/well needed to be seeded and then the plates were incubated for 24h at 37°C. On the next day the medium was removed, and the cells were washed with 200 µL HBSS (1% FCS) per well. To retrieve the staining solution, 2.5 mmol DCFH-DA stock solution in DMSO was further diluted in a 1:100 ratio with warm HBSS, resulting in a final concentration of 25 µM (80 µL stock solution in 8 mL HBSS). The cells were then stained for 45 minutes with 100 µL of the prepared staining solution at 37°C. In the meantime, the Synergy HT-Reader was started. Furthermore, two positive control solutions of TBHP were needed in the concentrations 90 µM and 200 µM, since those two concentrations were the highest used for single treatment with **Ir1** and ATO respectively. The two drugs were

diluted with colorless (phenol red-free) opti-MEM and the cells treated according to the scheme presented in **Figure 5**.

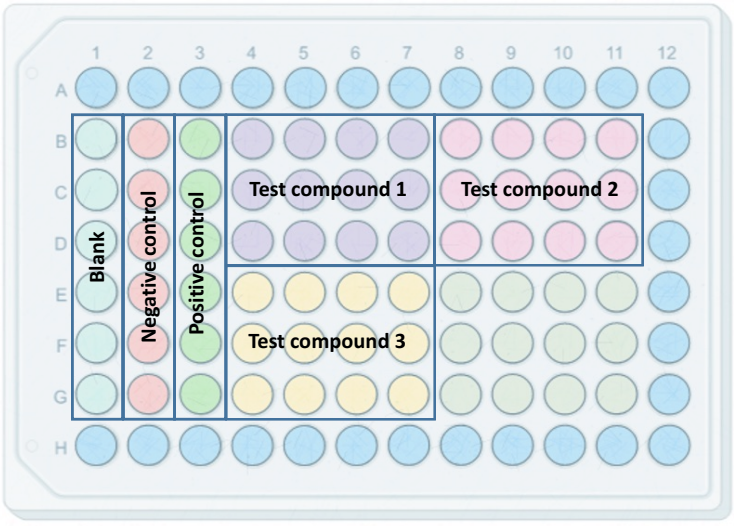

Figure 5: *Pipetting layout for DCFH-DA assay with Blank (colorless Opti-MEM without cells, light blue); negative control (colorless Opti-MEM, light red), positive control (2 dilutions of TBHP, bright green), test compound 1 (5 µM/IC_{25}, 50 µM/IC_{50}, 120 µM/IC_{75}, 200 µM/IC_{90} ATO, purple), test compound 2 (20 µM/IC_{25}, 45 µM/IC_{50}, 80 µM/IC_{75}, 90 µM/IC_{90} Ir1, pink), test compound 3 (20/45/80/90 µM + 20 µM Ir1+ATO, yellow).*

Blank represents the stained wells without cells on the bottom of the well, therefore the negative control contains only opti-MEM as "treatment" but with cells on the bottom of the wells. The positive control ensures the system is functioning correctly and producing reliable data. It serves as a benchmark to verify the cell response to known ROS inducers, which helps confirm the validity of the results and identify potential sources of error in the assay. The concentrations used for the positive control were 90 µM and 200 µM. The concentrations for **Ir1** (20 µM/IC_{25}, 45 µM/IC_{50}, 80 µM/IC_{75}, 90 µM/IC_{90} in triplicates per plate) and ATO (5 µM/IC_{25}, 50 µM/IC_{50}, 120 µM/IC_{75}, 200 µM/IC_{90} in triplicates per plate) were chosen according to MTT values. The treated cells were measured in the microplate reader every 10 min over a period of 2 h, without a lag phase. This procedure was performed with three consecutive plates. The blank corrected intensities were set into relation with the negative control to normalize the values, those including the standard deviation can be seen in the **Appendix.**

Cell-free assay

The basic principle for the cell-free DCFH-DA assays remained the same, only the washing steps were not included and no cells had to be prepared. 100 µL of DCFH-DA (50 µM) were measured with ATO, **Ir1** and **Ir1**+ATO respectively. The used concentrations were the same as in the cell-containing DCFH-DA assay and the pipetting scheme can be seen in **Figure 6**.

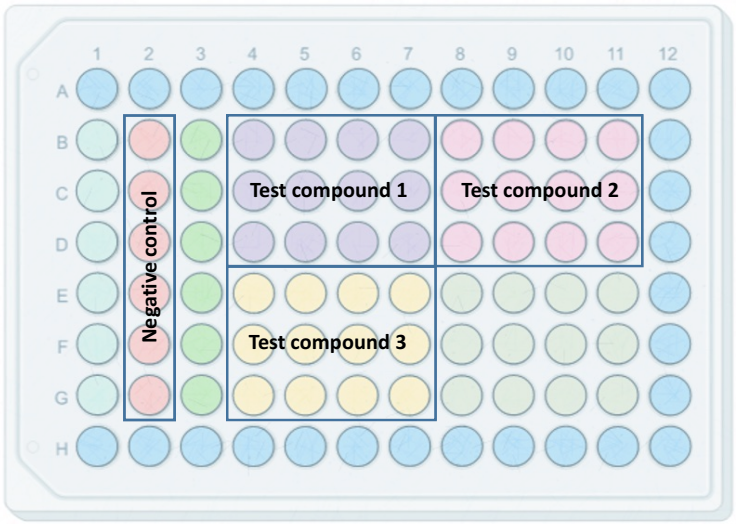

Figure 6: *Pipetting layout for DCFH-DA assay with Negative control (DCFH-DA, light red), test compound 1 (5 µM/IC_{25}, 50 µM/IC_{50}, 120 µM/IC_{75}, 200 µM/IC_{90} ATO, purple), test compound 2 (20 µM/IC_{25}, 45 µM/IC_{50}, 80 µM/IC_{75}, 90 µM/IC_{90} Ir1, pink), test compound 3 (20/45/80/90 µM + 20 µMIr1+ATO, yellow).*

The reaction mixtures were photometrically measured every 10 min over a period of 2 h and the data evaluated with Excel and GraphPadPrism. The blank corrected intensities were again set into relation with the negative control to normalize the values, those including the standard deviation can be seen in the **Appendix.**

3.5 Sample preparation

3.5.1 Cellular fractionation

As initial experiments, SW480 cells were treated with 20 µM **Ir1**, a concentration lower than the IC_{50} value from the MTT Assays. For this purpose, five T75 flasks were used to seed 6 x T25 flasks for CON and 6 x T75 for **Ir1** treatment, with 1.25 * 10^6 cells/T25flask. The flasks were left in the incubator at 37 °C and 5% CO_2 for 24 h. The next day, 36 mL medium were combined with 36 µL of 20 mM **Ir1** stock solution, creating a 20 µM treatment solution. As control treatment, 36 µL of DMSO were added into 36 mL of MEM. The medium from each T25 flask was lifted off, and 5 mL of either **Ir1**-medium or DMSO-medium mixture was added. The flasks were again incubated for 24 h at 37 °C and 5% CO_2.

After the treatment was completed, nucleocytoplasmic fractionation was performed at 4 °C. The first step was to remove the medium in each flask and wash twice with 3 mL PBS each time. Then, 1 mL of fractionation buffer (containing 1% PIC and 1% PMSF) was added and the flasks rested on ice. The cells were then scraped from the bottom of the flasks and transferred into 15 mL falcons with a syringe and a needle. To isolate the cytoplasm, the suspension was drawn up and down 12 times directly at the interior wall of the falcons. After some time, the falcons were centrifuged for 5 minutes at 3500 rpm and 4 °C. The cytoplasmic fraction (CYT, being represented by the supernatant) was transferred into different falcons, which already contained ice cold 99.9% EtOH in a final dilution ratio of 1:5. The falcons were closed immediately after adding the CYT,

inverted once, sealed with Parafilm and stored in the freezer at -20 °C until further usage. To the NE (nuclear) fractions, 100 µL TE-NaCl (1 mL, 10 mM Tris/HCl, 200 µL 1 mM EDTA, 10 mL 0.5 M NaCl, 100 mL of H_2O) was added and pipetted up and down and left on ice for 10 minutes. 900 µL of Triton X-100 was added to each sample (Triton X-100 and PMSF and PPC in a 1:100:100 ratio) and again after mixing put into the already precooled centrifuge for another 15 minutes. Afterwards the falcons were centrifuged with the same settings as previously used. The supernatant, representing the NE fraction, was transferred into new falcons already containing ice cold 99.9% EtOH as well. The falcons were closed, inverted once and also sealed with Parafilm and stored in the freezer at -20 °C until further usage.

3.5.2 Whole cell lysates

For whole cell lysates the experimental part was performed on ice as well, the supernatant was discarded after the 24 h treatment and the cells were washed twice with 1 mL of cold PBS each. After the washing solution was discarded, 80 µL of freshly prepared SDC buffer was added, the cells scraped and transferred into a 2 mL eppi. Then another 50 µL of buffer were pipetted onto each well and also collected in the corresponding eppi. The samples were then heated up and shaken at 95°C for 5 minutes and 1400 rpm. After cooling to room temperature, the samples were spun down and stored in the freezer at -20 °C until further usage.

When collecting the supernatant of high treatment concentrations, for the dose-resolved part of this thesis, it was not discarded but collected in 15 mL falcons and centrifuged for 5 min at 1100 rpm and 4 °C. The now "empty" wells were washed twice with PBS (1 mL for each washing step). Then 80 µL of freshly made SDC-buffer was added, the wells were scraped, the suspension transferred into 1.5 mL eppis, the wells scraped again, now with 15 µL of SDC buffer, and the suspension transferred into the corresponding eppi already containing the 80 µL. After the supernatants were finished centrifuging, the supernatant was lifted off completely, the pellet washed once with 1 mL PBS and centrifuged again for 2 min at 1100 rpm and 4 °C. The supernatant was again discarded, 110 µL of the 130 µL cell suspension in the eppis was used to solubilize the pellet and transfer it to the corresponding eppi. The samples were than shaken for 5 min at 1400 rpm and 95 °C, then left to cool at room temperature, spun down and stored in the freezer until further usage.

Generally, the samples (whole cells, supernatants and CYT and NE fractions) where then sonicated with the sonicating stick (1 pulse, 0.9 cycles, three times per sample) in 15 mL falcons. After the samples were done, they were centrifuged at 1000 g for 2 min and then transferred back into their corresponding eppis. All samples were shaken on the thermoshaker for 5 min at 95 °C and 300 rpm. Now the samples were ready for the BCA assay.

3.5.3 Protein quantification

The falcons containing NE and CYT fractions were centrifuged for 30 min and 5000 rpm at 4 °C. The supernatant was discarded and the falcons containing the protein pellets were placed upside down to dry for 2 h. The falcons were then dried in a desiccator for 15 min. 60 µL SDC buffer for CYT-pellets and 30 µL SDC buffer for NE-pellets was added and the falcons sonicated in a sonicating bath (15 min, RT, 100% power). After that, the falcons were centrifuged at 1000 rpm for 2 min and left over night at RT. The next day the pellets were suspended in the already existing SDC-buffer in the falcons, which worked for NE fractions but for CYT fractions more SDC buffer had to be added, resulting in a total volume of 200 µL SDC plus another 15 µL for washing the falcon. The suspensions were transferred into their corresponding eppis. This procedure was only necessary for fractionated samples, whole cell lysates were processed as followed. The next day, the samples were heated up and shaken for 5 min at 95 °C and 300 rpm. After letting them cool down, they were spun down at 10 000 g. To determine the protein concentrations of each sample, a BCA Assay was performed. After adding the working reagent, the 96 well plate was incubated at 60 °C for 30 min. The plate was then measured photometrically at 562 nm. After copying the extinction values into an excel sheet, the volumes needed for diluting the samples to obtain 20 µg of protein in a total volume of 90 µL SDC buffer per sample were determined. The "original" samples were then stored in the freezer at -20 °C. For the future workflow, only the diluted samples were used.

3.5.4 Protein digestion

After determination of all needed dilutions, 2 µL of 500 mM Bond-Breaker TCEP pH 7 was added and the eppi was vortexed immediately. The samples were then incubated at 45 °C for 5 min at 1200 rpm. To remove any condensate from the lid, all samples were centrifuged for a short term. For the alkylating step, 4 µL of 800 mM 2-CAM were added, the eppis vortexed and incubated at 45 °C for 5 min at 1200 rpm and again centrifuged briefly. The following steps were performed on ice. All samples were cooled, meanwhile a 0.1 µg/µL Trypsin/Lys-C enzyme stock was prepared. 10 µL of cold 0.1 µg/µL were added to each cold sample, the eppis vortexed immediately and put on the thermoshaker at 37 °C and 1200 rpm for 17 h. The next day, the samples were centrifuged shortly to remove any condensate from the lid.

3.5.5 StageTip clean up

To prepare the SDB-RPS (styrenedivinybenzene reverse phase sulfonate) StageTips for peptide cleanup, the following steps had to be conducted. Three discs of material had to be punched out with the syringe assembly. The three layers were filled into the pipette tip, paying attention to not compressing the material too tightly. To condition the tips, the adapters were placed onto 2 mL Eppendorf tubes. The StageTips were labeled and placed into the adapters. 150 µL of loading buffer were added and spun down for 5 min at 1000 g. Next, the volume of the digested samples was reduced in the SpeedVac (H_2O program at 45 °C) for 35 min.

After cooling to RT, 120 µL of loading & wash buffer 1 were added. The samples were vortexed, spun down and then transferred onto the previously conditioned SDB-RPS StageTips. For optimal binding, the samples were slowly centrifuged, first for 7 min and 500 g, then for 5 min at 1500 g. The loading buffer was discarded and 100 µL of wash buffer 1 was again pipetted onto the StageTip. The samples were centrifuged at 1500 g for 5 min, and then 100 µL of wash buffer 2 were added and centrifuged again at 1500 g for 8 min. The StageTips were transferred into 2 mL eppis with glass inlets. To receive all peptides out of the column, 30 µL elution buffer were added on top and centrifuged for 3 min at 500 g. This was repeated but at 1500 g for 8 min. The adapters including the StageTips were removed from the eppis and the samples dried in the SpeedVac for >1 h at 45 °C.

3.5.6 Peptide Reconstitution

The glass inlet, which contained the dried sample, was removed to add 400 µL of VWR H_2O to the 2 mL storage eppi. Afterwards, 5 µL of a 10 fmol/µL standard peptide mix was added to the dried sample then 40 µL of MS loading buffer were added and pipetted up and down multiple times to completely dissolve the dried sample. The glass inlet was reinserted into the storage tube and all samples were sonicated in the sonicating bath for 5 min, 40% power and RT. They were then centrifuged for 7 min at 5000 g and the glass inlet was finally ready to be transferred into the prepared MS glass vial. Now the samples were ready for measurement.

3.6 LC parameters

Peptide separation was carried out by using a Dionex UltiMate 3000 RSLCnano system (Thermo Fisher Scientific). For each run, 5 µL of the reconstituted peptide solution were injected onto a pre-column (Acclaim™ PepMap™ C18 100, Thermo Fisher Scientific) making use of solvent A (99.9% water, 0.1% formic acid) as the mobile phase at a flow rate of 10 µL/min. Subsequently, peptides were transferred from the pre-column to the analytical column (Aurora series emitter column, 1.6 µm C18, 25 cm · 75 µm, IonOpticks) and separated using a linear gradient from 12% to 42% solvent B (79.9% acetonitrile, 20% water, 0.1% formic acid) over 90 min at a flow rate of 300 nL/min. Including equilibration and washing steps, the overall chromatographic method lasted 140 minutes.

3.7 MS instrument parameters

Mass spectrometric detection was performed on a timsTOF Pro instrument (Bruker Daltonics) operated in parallel accumulation-serial fragmentation (PASEF) mode under DDA settings. Both MS1 and MS2 spectra were recorded within an m/z range of 100-1700. Ion mobility separation was achieved by scanning an inverse reduced ion mobility ($1/k_0$) range of 0.6-1.6 $Vs*cm^2$, with a ramp time of 100 ms per cycle. Each analytical cycle comprised ten PASEF MS/MS events, resulting in a total duty cycle of approximately 1.16 s.

3.8 Data processing

The raw data was searched using MaxQuant with the in-built Andromeda search engine using an UniProt fasta file. A false discovery rate (FDR) of 0.1 was applied on protein and peptide levels, along with a maximum of two missed cleavages per peptide. Additionally, carbamidomethylation of cysteine residues was set was a fixed modification, while the consideration of methionine oxidation was set as a dynamic modification. The resulting group file was further processed and analyzed using Perseus (Version 1.6.14.0). For further quantification the dataset containing the label-free quantification (LFQ) intensities of the wanted samples were selected. Subsequently, a filtering process was applied to eliminate contaminants, false positive results and palindromes. Following this, a logarithmic transformation was applied, and the data was categorized into two groups, one for the control cells and one for the treated cells. Furthermore, these groups underwent additional filtering, requiring each group to have a minimum of 70% out of the total amount of biological replicates for each condition. These filtered datasets were then employed to construct a profile plot. Moreover, for the creation of volcano and scatter plots, missing values in the dataset were populated with automatically generated values by imputation, establishing a Gaussian distribution to facilitate the statistical analysis. Statistically significant protein regulations between control and treatment conditions were calculated by multiple testing correction according to a FDR of 0.05 and S_0= 0.1.

The now filtered data was exported into Excel, where the proteins with significant value were separated from the ones, which do not show a significant difference to control samples. The remaining proteins were analyzed and split into up and down regulated proteins, each regulation from each treatment was then further analyzed depending on the wanted outcome.

Python scripts, which were used to generate some of the graphs in this thesis, were corrected and refined with the assistance of the AI model ChatGPT.

4. Results and Discussion

The goal of this Master thesis was to investigate the molecular effects of a catalytically active Iridium compound (**Ir1**) on the proteome in the colorectal cancer cell line SW480. Ir1 is a representative of SIMCats (small molecule intracellular metal catalysts). The first step was to perform interaction studies with **Ir1**, to fully characterize the mechanism of hydride transfer in a cell-free system using the metallodrug in combination with aldehydes and hydride/deuteride-donors.

Afterwards, SW480 cells were treated with a sub cytotoxic concentration of **Ir1** and cellularly fractionated. Because significantly regulated proteins were only detected in the nuclear fractions of the cells, it was determined to conduct further experiments on whole cell lysates only. As main topic of this thesis, a dose-resolved proteomics assay was established and performed with **Ir1**, at different concentrations with four replicates per treatment.

The combination treatment of **Ir1** with ATO was performed in order to elucidate potential synergistic/antagonistic effects in SW480 cancer cells. After confirming such effects on the viability of the cancer cells, molecular signatures were evaluated by proteomic profiling with six replicates of each mock-treated controls, cells treated with **Ir1**, cells treated with ATO, and cells treated with both **Ir1** and ATO. In addition, DCFH-DA-Assays with and without SW480 cells treated with **Ir1**, ATO and combination treatment were performed as well.

4.1 Interaction study

Iridium-based SIMCats, such as **Ir1**, catalyze hydride transfers between hydride donors and toxic aldehyde species, e.g. 4-HNE, to form non-toxic alcohols (**Figure 7**).

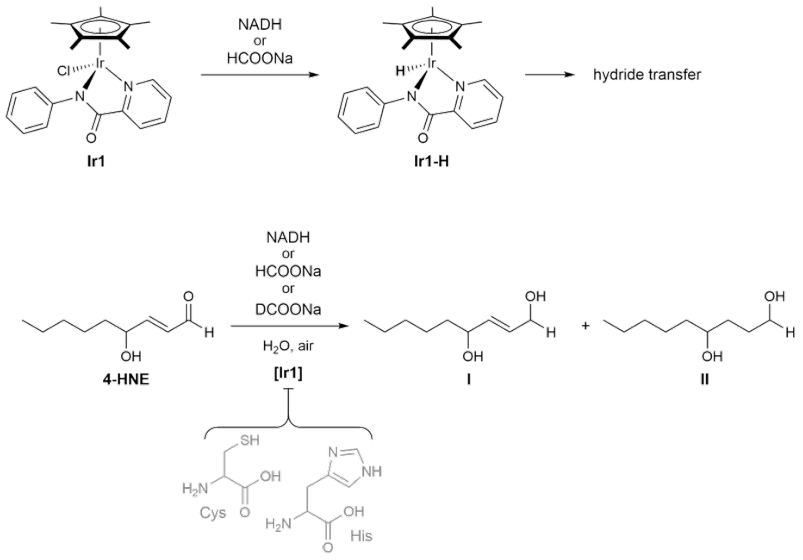

Figure 7: *Reaction scheme of Ir1 and 4-HNE in presence of hydride donors.*

For this thesis, **Ir1** as a catalyst for the mentioned transfer hydrogenation, 4-HNE as a reactive aldehyde, Pyridoxalphosphate (Py) as another aldehyde and NADH, HCOONa and DCOONa as hydride/deuteride donors were used.

Two conditions containing both aldehydes (4-HNE and Py), either NADH or HCOONa, and water were used as control reactions. This allowed the time-dependent behavior of the two hydride donors and the aldehydes to be monitored without **Ir1**. In addition, three conditions with Iridium as the hydride-transfer reagent, NADH, HCOONa, or DCOONa as the hydride/deuteride donors, and both aldehyde species were measured to observe the different reaction profiles in the presence of **Ir1**. Two deactivation reactions were carried out as well, therefore Cys+His were added to the reaction mixtures. These amino acids contain good nucleophiles that can bind more strongly to **Ir1** and therefore slow down hydride formation. The only difference between the deactivation reactions was that for Deact B, **Ir1**, Cys+His, and water were pre-incubated for 24 h.

The seven different conditions were mixed in eppis and measured in triplicates and at multiple time points (0h, 4h, 8h, 12h, 16h, 20h) in ESI-positive mode on the QExactive HF Orbitrap LC-MS/MS system.

Given the fact that the **Ir1** compound performs a hydride transfer to convert toxic aldehydes into alcohols, it was specifically focused on the signal intensities of 4-HNE and the resulting products 4-HNE (I, +2) and 4-HNE-D (I, +3). Py was measured as well, but not yet evaluated.

4-HNE (educt)

As shown in **Figure 8**, the intensity of 4-HNE decreases over time in the samples containing the **Ir1** compound and a hydride donor, i.e. Rxn A, Rxn B and Rxn C. In contrast, 4-HNE intensities remained stable for Con A and Con B, as well as Deact A and Deact B. In the latter, cysteine and histidine were added as potential deactivating ligands. Indeed, the intensity of 4-HNE remained relatively constant, supporting the assumption that coordination of these amino acids inhibits the catalytical activity of **Ir1**. Of note, preincubation of cysteine and histidine with **Ir1** (Deact B) completely abolished the catalytic activity, while co-incubation with hydride donors and aldehydes led to a competitive catalytic inhibition (Deact A). This confirms that the observed conversion is indeed **Ir1**-dependent and not due to spontaneous degradation or non-specific reactions.

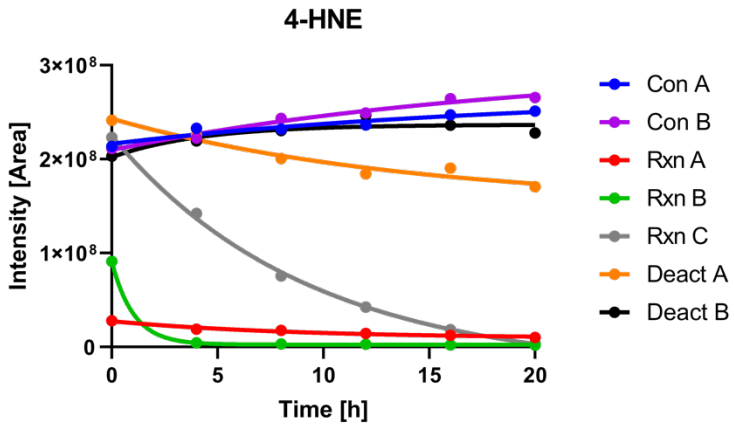

Figure 8: *Intensity courses of 4-HNE across all conditions over time.*

4-HNE (I, +2)

The formation of the reduced product 4-HNE (I, +2) is depicted in **Figure 9**. A clear time-dependent in intensity is observed in Rxn B, where **Ir1** is combined with HCOONa as the hydride donor. The signal rises sharply during the initial phase and reaches a plateau at a reaction time of 10 h, indicating progressive product accumulation and reaction completion. On the other hand, no product formation is observed in the control reactions, in the deactivated **Ir1** samples or in Rxn C. The lack of signal in Con A demonstrates the catalytic role of **Ir1** in mediating the hydride transfer.

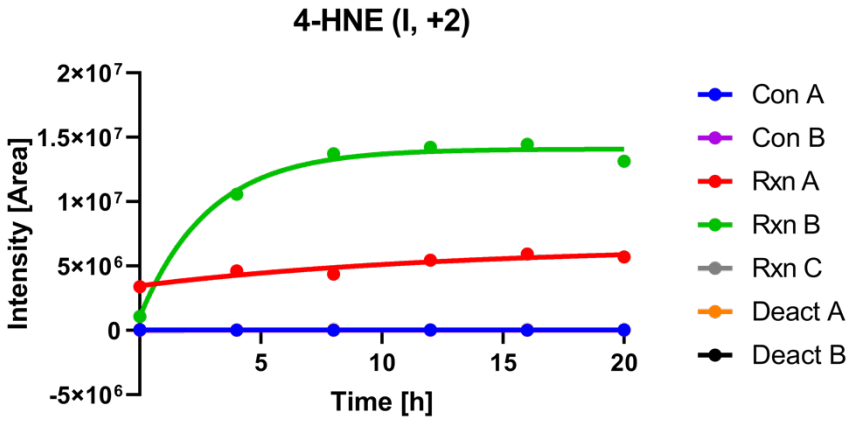

Figure 9: *Intensity courses of 4-HNE (I, +2) across all conditions over time.*

4-HNE-D (I, +3)

The deuterated analog shows a similar pattern in **Figure 10**. When DCOONa is used as a deuteride donor, Rxn C, the intensity of the product increases steadily over time, confirming the incorporation of deuterium into the reaction product. This is accompanied by a corresponding decrease in 4-HNE signal intensity, consistent with substrate conversion. As expected, the deuterated product is absent in all other reaction conditions.

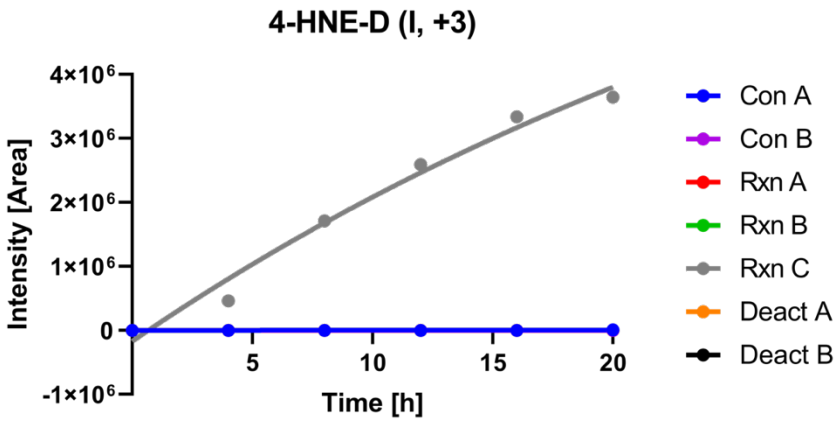

Figure 10: *Intensity courses of 4-HNE-D (I, +3) across all conditions over time.*

To ensure a better comparison between 4-HNE and its products for each reaction, individual graphs were generated for Rxn A, Rxn B and Rxn C (**Figure 11**).

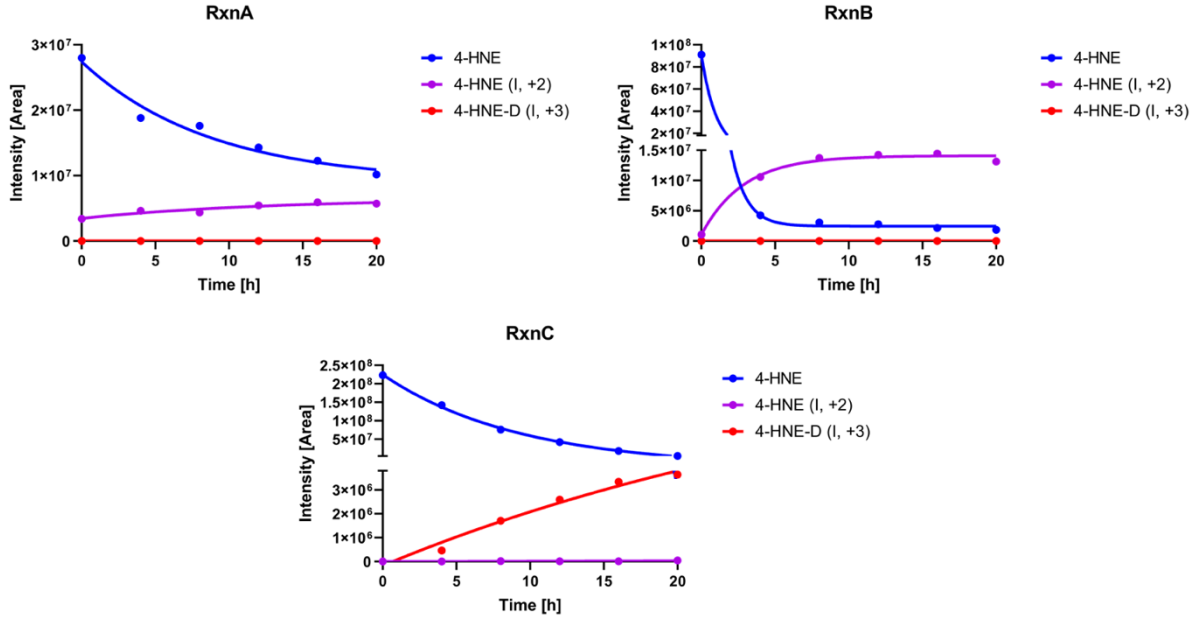

Figure 11: *Intensity courses of 4-HNE, 4-HNE (I, +2), 4-HNE-D (I, +3) across Rxn A (top left), Rxn B (top right), Rxn C (bottom middle) over time.*

The data clearly show that the intensity of 4-HNE decreases progressively over time in Rxn A, B, and C, accompanied by a corresponding increase in product intensity, 4-HNE (I, +2) in Rxn A and B, and 4-HNE-D (I, +3) in Rxn C. This indicates the successful conversion of the aldehyde to its respective reduced forms by **Ir1** in the presence of hydride donors.

4.2 Drug treatment

4.2.1. MTT Assays

The MTT-Assay is a colorimetric method to measure the capability of viable cells to convert a soluble tetrazolium salt, specifically [3-(4,5-dimethylthiazol-2-yl)-2,5-diphenyltetrazolium bromide] (MTT), into an insoluble formazan precipitate by mitochondrial reductase (**Figure 12**).[57,58]

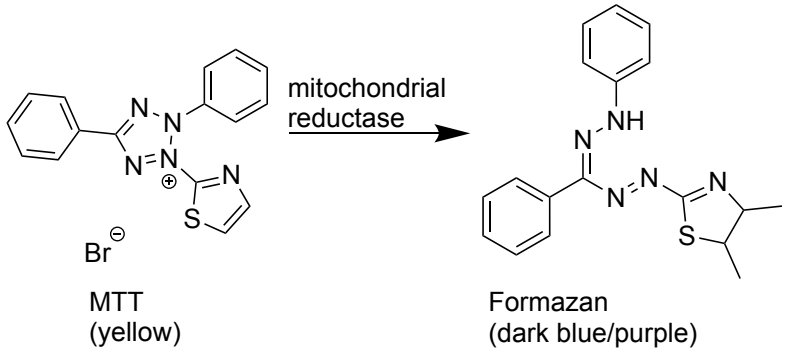

Figure 12: *Chemical reaction of MTT inside a viable cell.*[59]

Tetrazolium salts accept an electron from oxidized substrates or suitable enzymes, such as NADH and NADPH. MTT is reduced at the ubiquinone and cytochrome b and c sites of the mitochondrial electron transport chain, a process facilitated by succinate dehydrogenase. This reaction converts the yellow salts into blue-colored formazan crystals, which can be dissolved in an organic solvent.[57] After re-dissolving the crystals, the concentration is measured by optical density at 570 nm. This method results in a sensitive assay with linearity accommodating up to 10^6 cells per well.[58]

To determine the IC_{50} concentration of **Ir1** and ATO, various MTT assays in 96-well-plates were performed. The final concentrations of the wells were 0-10-25-35-40-50-70-80-100 µM **Ir1** and 0-2.5-5-10-20-40-80-120 µM ATO. "Blank" is for reference and does not contain any cells, whereas the "0 µL" columns in the wells do. After treating the SW480 cells for 24 h with each compound, and evaluating the data through sigmoidal curve fitting, the IC_{50} values were determined for each compound, concluding an IC_{50} value of 45 µM for **Ir1** and 50 µM for ATO.

4.2.2 Single-dose proteomics/perturbation

Furthermore, SW480 were treated with 20 µM **Ir1** (approximately IC_{25}) as pre-experiment to establish whether nucleocytoplasmic fractionation was necessary for further experiments. After a 24 h treatment, the cells were collected, fractionated into nucleus and cytoplasm and further processed by in solution digestion and StageTip workup. The samples were analyzed on a nanoHPLC-MS/MS and the results evaluated using the software MaxQuant and Perseus 1.6.14.0. When analyzing the data, it appeared that there were no significantly regulated proteins in the cytoplasmic fractions but only in the nuclear fractions (**Figure 13**). Since

there was no regulation information in the cytoplasmic fraction, the following experiments were processed as whole cell lysates. This also reduces the experimental burden of a nucleocytoplasmic fractionation and allows to carry out a larger number of different conditions.

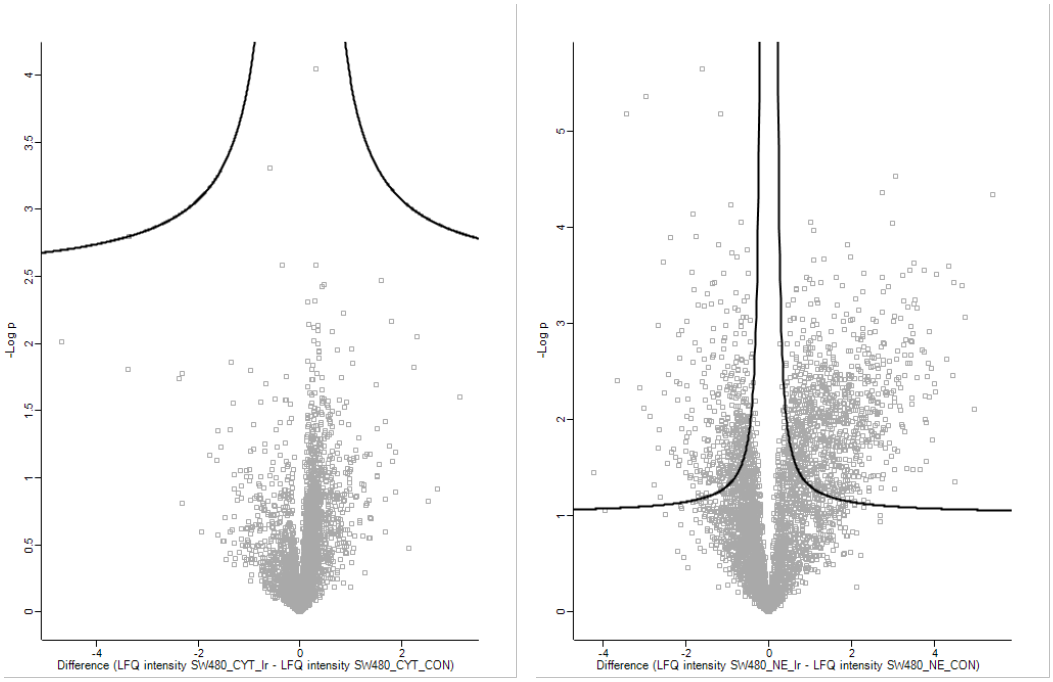

Figure 13: *Volcano plots of cytoplasmic (left) and nuclear (right) fractions from pre-experiments treating SW48 cancer cells with* ***Ir1*** *(20 µM for 24 h).*

4.2.3 Dose-resolved proteomics

To achieve a thorough characterization of dose-resolved effects of **Ir1** on the proteome of SW480 cancer cells, 9 different concentrations of the metallodrug were selected (**Table 13**) from the initial MTT-Assay, namely IC_{10} (5 µM), IC_{20} (10 µM) IC_{30} (23 µM), IC_{40} (35 µM), IC_{50} (45µM), IC_{60} (56 µM), IC_{70} (75 µM), IC_{80} (85 µM) and IC_{90} (90 µM). The cells were seeded according to a 250,000 cells/well count in 6-well plates and four replicates per condition in a total of 40 samples.

Table 13: *Used concentrations for dose-resolved proteomics.*

Inhibitory concentration	Concentration [µM]
IC10	5
IC20	10
IC30	23
IC40	35
IC50	45

IC60	56
IC70	75
IC80	85
IC90	90

SW480 cells were treated with the concentrations from IC_{10}-IC_{90} in 10% increments and mock-treated with DMSO for 24 h. To ensure the treatment worked, every condition was photographed after 24 h with ZEN through the microscope and documented (**Figure 14**).

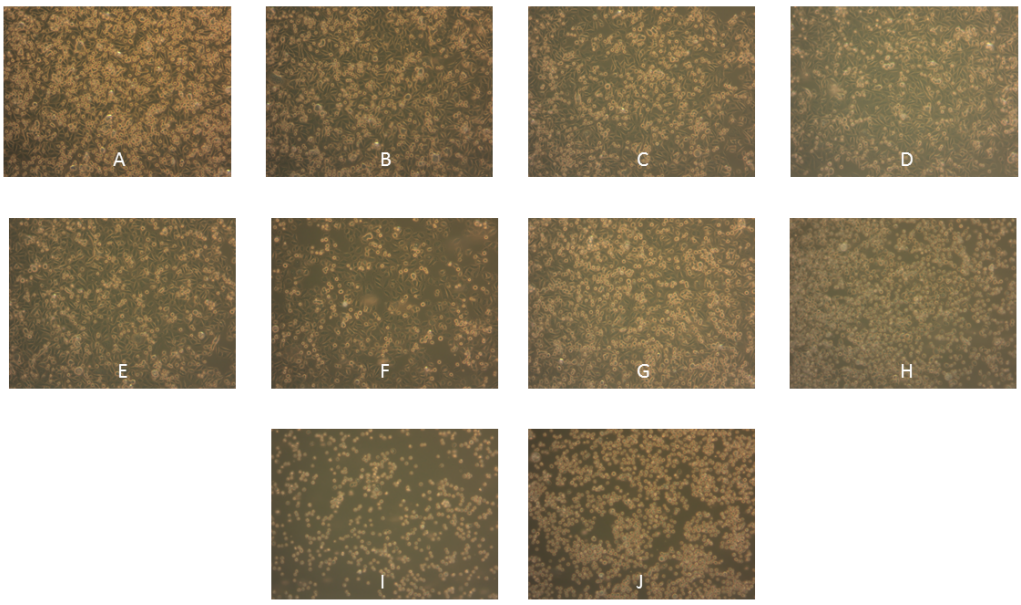

Figure 14: *SW480 cells after 24h treatment. A: Control (DMSO), B: IC_{10}, C: IC_{20}, D: IC_{30}, E: IC_{40}, F: IC_{50}, G: IC_{60}, H: IC_{70}, I: IC_{80}, J: IC_{90}.*

The microscopy images show that, at concentrations ≥IC_{60}, an increasing number of cells detach from the surface of the culture flask and float freely in the medium. Because these detached cells are located at different focal planes, they can no longer be properly visualized under the microscope. This observation indicates that treatment at higher concentrations induced cell death, as expected. To ensure sufficient protein yield, not only adherent cells but also the supernatant containing the detached cells were collected for concentrations ≥IC_{60}. Whole cell lysates were collected of the 40 samples and the total protein amounts were determined by the BCA assay for each sample as well as the volumes required to normalize to 20 µg protein in 90 µL buffer, which are listed in the **Appendix**

The samples were processed similarly to the established protocol by in-solution digestion. Then, the processed samples were analyzed by nLC-MS/MS on a timsTOF Pro mass spectrometer, and the data was searched using MaxQuant and evaluated using Perseus, STRING, David bioinformatics and GraphPad, revealing a total of 5842 proteins being identified in all 40 samples. Plotting the data as a PCA (Principal

Component Analysis, **Figure 15**) indicated a dose-dependent behavior across the treatment concentrations and underlining the variance of the different groups across the experiment.

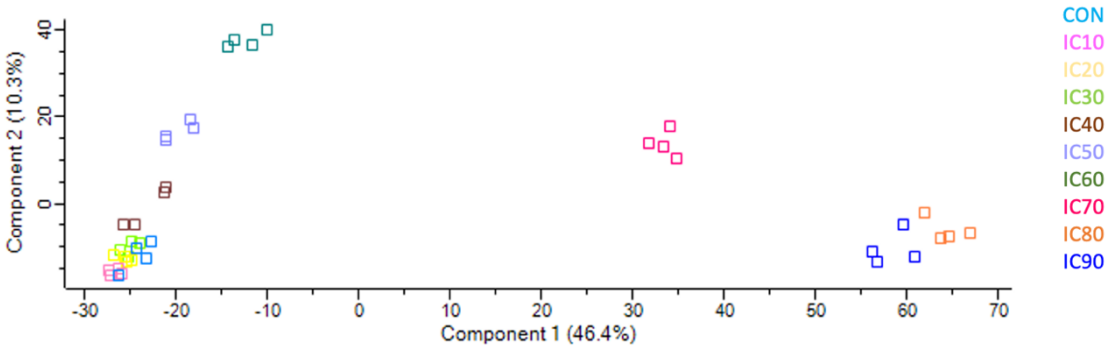

Figure 15: *PCA of the dose-resolved experiment including the color-codes for each concentration (component 1 representing cell death, component 2 representing cellular stress response).*

More detailed information on each concentration and its significantly up- and down-regulated proteins can be seen in **Table 14**. It is evident that at concentrations ≤IC_{30} no significantly regulated (s.r.) proteins could be detected. Starting from IC_{40}, however, the number of s.r. proteins steadily increases and reaches its maximum at IC_{90}, which is not surprising since the cell attempts to counteract the stress induced by the treatment at such high concentrations. Considering these data together with the PCA, it can be concluded that ≤IC_{60} the cell still engages in a cellular stress response, whereas from IC_{70} onwards it begins to shift more towards cell death.

Table 14: *Number of significantly up- and down-regulated proteins, including the total amount of proteins, per treatment.*

Concentration	Upregulated Proteins	Downregulated Proteins	Total Amount
IC10	0	2	2
IC20	0	0	0
IC30	0	0	0
IC40	62	74	136
IC50	537	660	1197
IC60	687	1152	1839
IC70	1577	1862	3493
IC80	1878	1756	3634
IC90	2285	1754	4039

Overview of dose-dependent effects

To obtain a comprehensive overview of the dose-dependent perturbation effects on the proteome, significantly up- and downregulated proteins from each treatment were analyzed using DAVID Bioinformatics with respect to gene ontology (GO) term enrichments according to different concentrations. It was especially focused on terms related to GO biological processes. Only terms that were enriched in a statistically significant manner after multiple-testing correction (Benjamini-Hochberg) are considered. Since treatment of IC_{10}-IC_{30} did not lead to a strong perturbation, those concentrations were not included in the following analysis

Upregulated Proteins

The top three enriched GO terms for each concentration from IC_{40}-IC_{90} for significantly upregulated proteins, were visualized using a Python-based plotting approach (**Figure 16**).

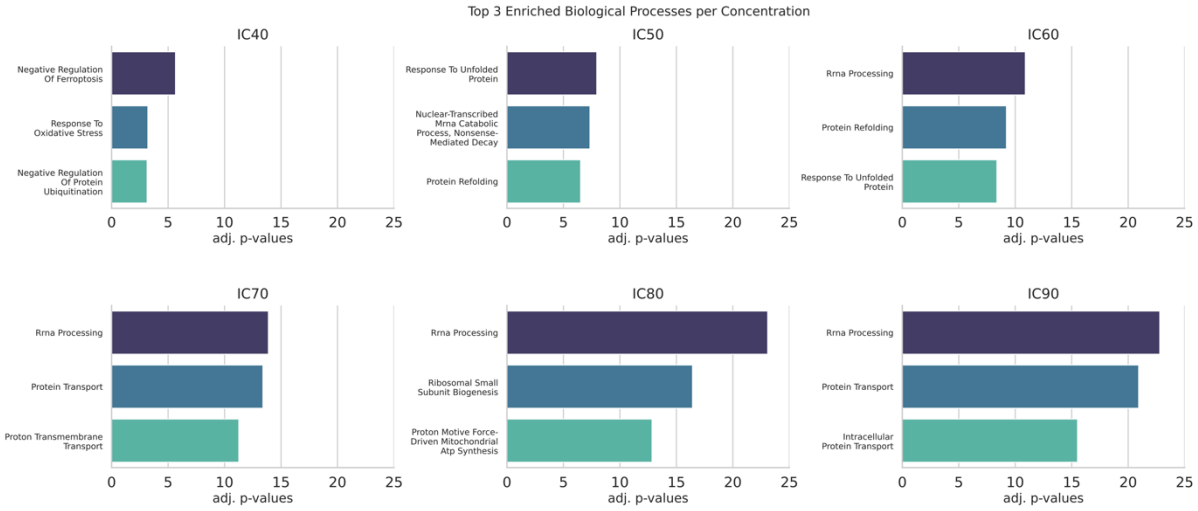

Figure 16: *Top 3 enriched GO biological processes per concentration (x-axis = adj. p-values for the enrichment GO biological processes of upregulated proteins, y-axis = top three terms).*

The enrichment analysis revealed a clear concentration-dependent progression of cellular stress responses in the treated cancer cells, as discussed previously. At IC_{40}, the data indicate an early adaptive phase characterized by activation of antioxidant defenses and mechanisms that counteract stress. This suggests that the cells initially engage redox-balancing and protective signaling to preserve viability under mild treatment conditions, which might be directly related to the transfer hydrogenation property of **Ir1** affecting the redox balance in cancer cells. Early cytoprotective responses are also typical for malignant cells, which often maintain an equilibrium between pro-oxidant metabolism and antioxidant buffering to support proliferation while resisting therapeutic stressors. As described by Jomova et al.,[60] cancer cells generate reactive oxygen species (ROS) through pro-oxidant metabolism but simultaneously activate antioxidant defenses to preserve redox balance and survive under stress.[60]

At IC_{50} and IC_{60}, enrichment patterns pointed toward a strong activation of proteostasis and RNA quality-control networks. These findings imply that the treatment induces stress and accumulation of misfolded proteins, triggering the unfolded protein response and associated molecular chaperone systems. Simultaneously, pathways responsible for monitoring and degrading unusual mRNA transcripts are activated to restore translational accuracy. In the context of cancer cell biology, this stage likely presents an adaptive state where the proteome maintenance machinery attempts to moderate rising proteotoxic stress and sustain cellular integrity.

At higher concentrations, $IC_{70\text{-}90}$, the cellular dynamics shifted toward processes associated with ribosome biogenesis, intracellular transport and mitochondrial energy metabolism. These enrichments suggest that persistent or overwhelming stress disrupts fundamental biosynthetic and bioenergetic functions. Impaired ribosomal activity and rRNA processing indicate nucleolar stress, a well-established trigger of p53-dependent apoptosis as a hallmark of translational collapse. At the same time, alterations in mitochondrial ATP production and protein trafficking point to energy shortage and organellar dysfunction, consistent with the transition from adaptive stress to terminal stress responses and induction of cell death pathways. The cumulative effect likely reflects a breakdown of cellular homeostasis, where compensatory mechanisms fail. The overall summary of the top upregulated processes across the treatment concentration from IC_{40}-IC_{90} as bar plots can be seen in **Figure 33** in the **Appendix**.

The results suggest that the compound initially has no effects on the proteome up until IC_{30}, and then elicits reversible stress adaption but progressively drives the cells toward energetic exhaustion and cell death at higher doses. This transition mirrors a broader principle of cancer cell stress biology in which survival at low stress levels depends on homeostatic networks, while excessive perturbation of these same systems ultimately exposes the intrinsic fragility of the malignant phenotype. To visualize the results more clearly, the data were additionally plotted as a heatmap (**Figure 17**).

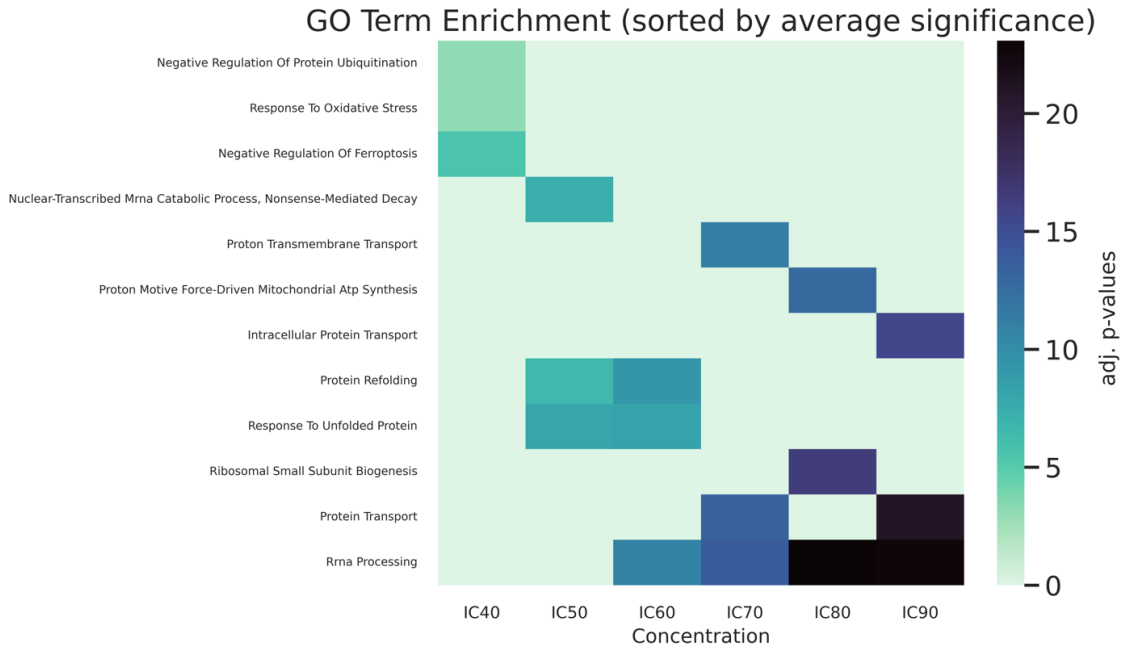

Figure 17: *Heatmap of Gene-Ontology Term enrichment of top 3 biological processes sorted by average significance (upregulated proteins).*

Overview of Dose-dependent effects (downregulated proteins)

The GO enrichment analysis of downregulated proteins according to biological processes revealed a clear, concentration-dependent suppression of key cellular processes in SW480 cells. An overview of the top 3 biological processes per concentration, **Figure 18** was created with Python.

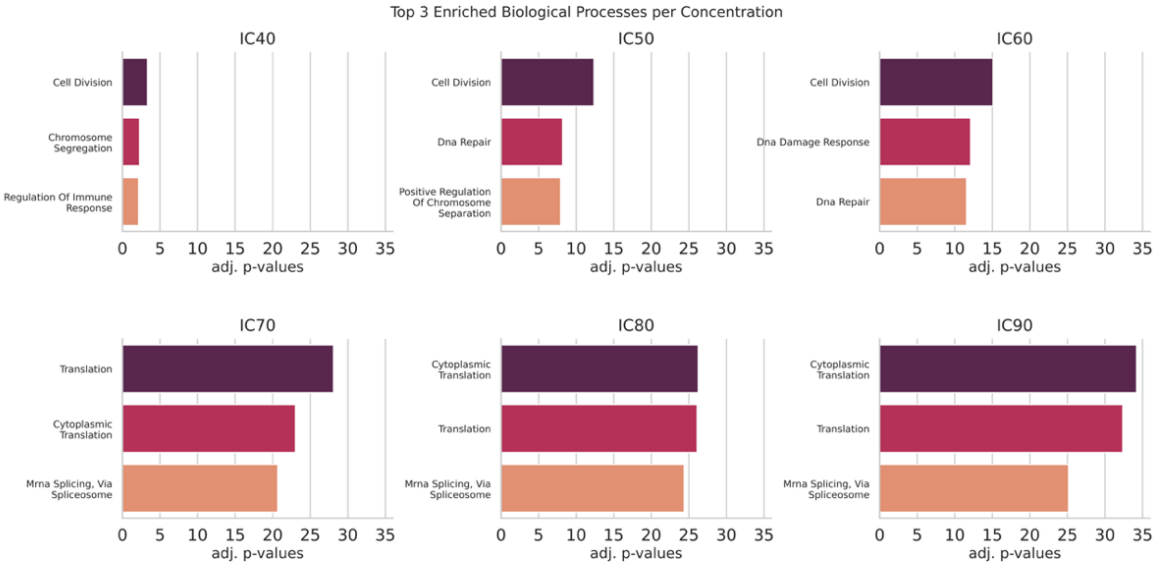

Figure 18: *Top 3 enriched biological processes per concentration (x-axis = adj. p-values for the enrichment GO biological processes of downregulated proteins, y-axis = top-three terms).*

At lower concentrations, IC_{40}-IC_{60}, the treatment primarily affects pathways associated with cellular division and immune regulation, suggesting an early interference with the proliferative machinery and cellular surveillance systems. Such modulation at sublethal doses indicates that the compound begins to exert stress on repair mechanisms, likely slowing the cell cycle progression and reducing the ability of cell to maintain a proliferative state.

As the treatment concentration increases, from IC_{70} onwards, this effect extended toward a more global inhibition of translation and RNA processing pathways, reflecting a shutdown of the biosynthetic capacity required for sustained growth and proliferation. The data imply that the compound disrupts not only the replication dynamics but also the metabolic and transcriptional activity of the cells. This progressive pattern of downregulation suggests that the compound acts through a dual mechanism, initially affecting proliferative maintenance functions and subsequently inducing a metabolic and translational arrest at higher doses. **Figure 34**, which can be seen in the **Appendix**, serves as an overview of the biological processes across the concentration range from IC_{40}-IC_{90}.

Overall, these findings indicate that the treatment drives colon carcinoma cells towards a state of proliferative and translational arrest, consistent with a potent cytostatic or anti-proliferative mode of action. To provide a more intuitive overview of the data, the results were further visualized as a heatmap (**Figure 19**).

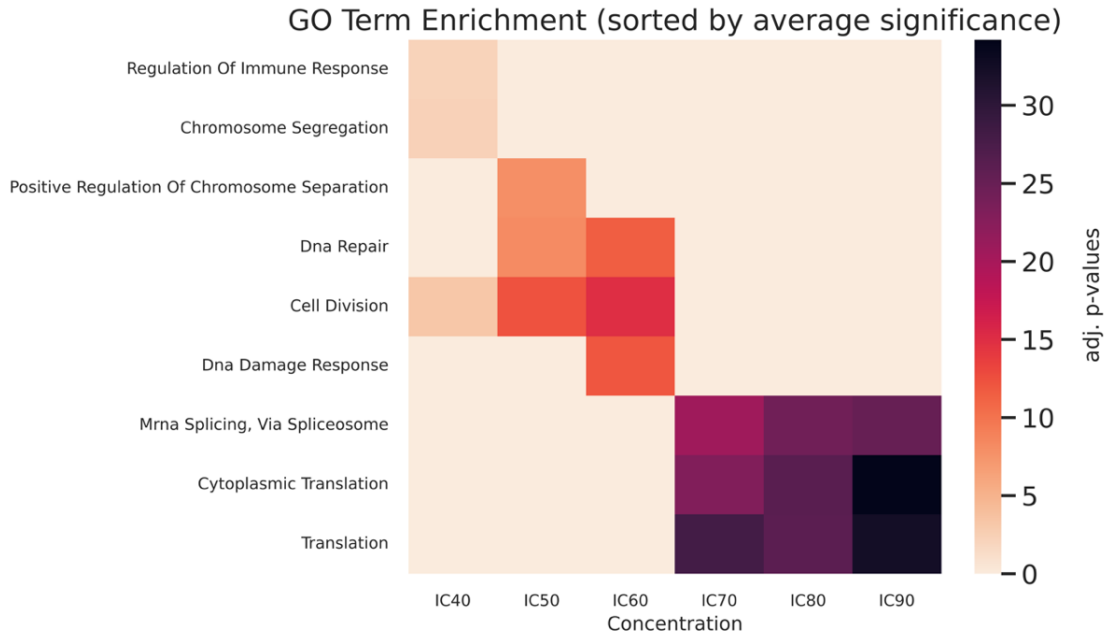

Figure 19: *Heatmap of Gene-Ontology Term enrichment of top 3 biological processes sorted by average significance (downregulated proteins).*

Main processes mediated by dose-dependent treatment

Combining the insights from the previous overview on the affected biological processes together with the examination of protein profiles in Perseus, revealed interesting dose-dependent trends also on the single protein level: stress response (NRF2 pathway, UPR and heat shock proteins), metabolic reactions (Glycolysis, Pentose Phosphate Pathway and One-Carbon Metabolism) and apoptosis. Within each category, distinct some general patterns of dose-dependent regulation were observed including:

1. Continuous decrease with increasing concentration
2. Continuous increase with increasing concentration
3. Increase up to a certain concentration, followed by a decrease and vice versa
4. Appearance only at specific concentrations
5. Mixed or atypical response patterns

Analysis of the NRF2 Pathway

Functional annotation using DAVID revealed that the most enriched biological processes among NRF2-related proteins included redox homeostasis, response to oxidative stress and more. Proteins that decreased in abundance with higher concentrations were mainly involved in antioxidant defense, ROS detoxification, and cellular redox maintenance. Their levels remained stable until IC_{60}, where they collectively began to decline, consistent with the expected breakdown of the antioxidant defense at high stress levels. In contrast, only one protein, solute carrier family 2 (SLC2A1), showed a dose-dependent increase. This glucose transporter is known to be overexpressed in many cancer cell types, where it enhances glucose uptake to fuel growth, proliferation, and therapy resistance.[61] The observed upregulation likely reflects an adaptive attempt of the cancer cells to support their metabolic needs under increasing treatment stress.

Other NRF2 regulated proteins displayed a temporary activation before declining again. They are typically involved in oxidative stress regulation, heme catabolism, and detoxification pathways. For example, heme oxygenase 1 (HMOX1), which degrades heme and promotes tumor progression, shows a bell-shaped pattern with a maximal intensity at IC_{60}. It is induced as part of the antioxidant response but cannot be established once stress becomes overwhelming.

Two additional NRF2-related proteins, early growth response protein 1 (EGR1) and transcription factor MAFK (MAFK), appeared only at specific concentrations. EGR1 acts as a transcription factor regulating growth, survival and p53 activation. Its late appearance at higher concentrations is consistent with a compensatory stress response focused at activating tumor-suppressive pathways. MAFK, a small Maf protein, can dimerize with other transcription factors and act as a competitive repressor within redox and heme regulation networks.

Analysis of Heat Shock Proteins

Heat shock proteins (HSPs) are categorized into five groups: 70 kDA HSPs, DNAJ family members, small HSPs, 90 kDa HSPs, and chaperonins.[62]

Many HSPs maintained stable expression up to approximately IC_{50} after which their intensities began to increase slightly, followed by a decline beyond IC_{60}-IC_{70}. This pattern mirrors the response of most NRF2-related proteins and aligns with the shared role of both systems in managing cellular stress. According to Qi et al.,[63] downregulation of DnaJ homolog subfamily B member 1 (DNAJB1) in cancer cells suppresses the p53 signaling pathway, weakening the cell's ability to control damage. At the same time, this downregulation enhances Rb/E2F signaling, thereby promoting proliferation. This suggests that reduced DNAJB1 may contribute to uncontrolled cell growth under stress conditions.

TNF receptor-associated protein 1 (TRAP1), a mitochondrial chaperone involved in apoptotic signaling in colon cancer cells,[64] showed elevated levels in LFQ intensity at IC_{70} and above, indicating activation of a mitochondrial stress response that could help cells resist apoptosis under intense oxidative conditions. A similar trend was observed for DnaJ homolog subfamily A member 3 (DNAJA3).

Previously, heat shock protein family A member 6 (HSPA6) was identified as a potential contributor to colorectal cancer progression. In this experiment, HSPA6 expression was first detected at IC_{50}, increased at IC_{60}, and declined at higher concentrations. This profile likely reflects a protective response that collapses under severe stress, consistent with mitochondrial dysfunction or apoptosis.

To visualize the different courses of the proteins more clearly, the LFQ intensities of selected NRF2-pathway proteins and heat shock-proteins were visualized as profile plots (**Figure 20**).

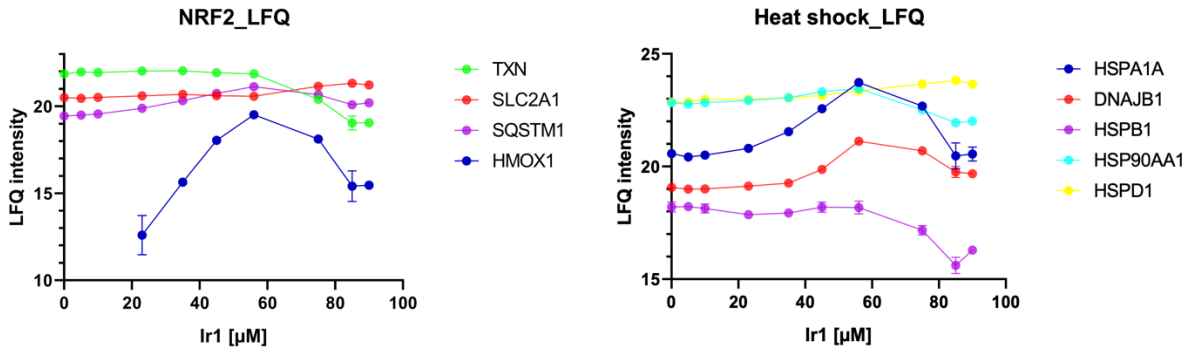

Figure 20: *LFQ intensities of specifically chosen proteins of NRF2 pathway (left) and heat shock (right).*

Analysis of Apoptosis-Related Proteins

In contrast to previous pathways, apoptotic proteins exhibited more complex and less uniform intensity patterns. This may be expected as apoptosis is governed by caspases that cleave and inactivate specific

substrates, but which may not be uniformly regulated. Tumor protein p53 (TP53), a key tumor suppressor, showed a unique trend. Its abundance remained stable until IC60, dropped sharply, and then recovered from IC_{70} onwards. Given its central role in DNA damage response and cell fate regulation,[65,66] this transient decline might indicate a temporary suppression or post-translational regulation at the limit of irreversible stress.

An interesting interaction was observed between transmembrane Bax Inhibitor motif-containing 6 (TMBIM6) and BCL-2-interacting killer (BIK). TIMBIM6, also known as Bax inhibitor, promotes cell survival and modulates ROS signaling, whereas BIK acts as a pro-apoptotic factor.[67,68] In this study, TMBIM6 disappeared after IC_{50}, while BIK expression increased from IC_{40} onwards, suggesting a shift from anti-apoptotic to pro-apoptotic signaling as treatment intensity increased. This opposing regulation illustrates how the cancer cells initially attempt to resist cytotoxic stress but eventually activate death pathways once damage becomes unbearable and irreparable.

Cytochrome c somatic (CYCS), a mitochondrial electron carrier and apoptosis effector, also showed dynamic regulation. Its disappearance between IC_{40} and IC_{60}, followed by more stable expression at IC_{70} and beyond, suggests that mitochondrial membrane integrity and apoptotic signaling fluctuate with treatment severity.

Analysis of Glycolysis

Glycolytic proteins generally maintained stable expression at low to intermediate concentrations but decreased beyond IC_{60}. This is consistent with the role of glycolysis in promoting tumor growth, metastasis, and therapy resistance.[69] Suppression of glycolytic enzymes at higher concentrations indicates metabolic collapse and loss of the cancer cells' adaptive energy advantage.

Phosphoglucomutase 1 (PGM1), which catalyzes the reversible conversion between glucose-1-phosphate and glucose-6-phosphate, disappeared at concentrations of IC_{70} and above. Given its central role in carbohydrate metabolism and glycan biosynthesis,[70] this loss is consistent with the disruption of cellular energy homeostasis.

Similarly, hexokinase domain containing 1 (HKDC1), a hexokinase-like enzyme involved in glucose homeostasis and cancer progression,[71] showed strong activation before disappearing after IC_{40}, although it already starts fluctuating at IC_{40}. The rapid decline beyond IC_{40} suggests that the stress conditions quickly exceeded the threshold at which HKDC1 can maintain its metabolic and pro-survival functions.

Analysis of Pentose Phosphate Pathway

The Pentose Phosphate Pathway (PPP) is essential for nucleotide synthesis and antioxidant defense in proliferating tumor cells.[72] In this project, most PPP-related proteins decreased in abundance from IC_{60} onwards, consistent with loss of biosynthetic and redox capacity under strong treatment stress.

Transketolase-like-1 (TKTL1), which is frequently overexpressed in certain cancers, disappeared at concentrations ≥IC_{50}. As TKTL1 activation is associated with PPP upregulation and enhanced cell survival,[73] its disappearance indicates inhibition of this pro-survival branch and suppression of cancer cell metabolism at high concentrations.

Analysis of One-Carbon Metabolism

Similar to other pathways, most proteins associated with one-carbon (1C) metabolism showed decreasing abundance with increasing concentrations, with a few exceptions.

Thymidylate synthase (TYMS), a key enzyme in thymidylate synthesis and a known determinant of chemoresistance,[74] initially decreased up to IC_{50}, followed by a concentration-dependent rebound from IC_{60} onward. This rebound likely represents a compensatory mechanism to restore nucleotide pools and DNA synthesis under metabolic stress.

Two enzymes, cystathionine-β-synthase (CBS) and betaine-homocysteine methyltransferase (BHMT), displayed inverse regulation. Both are central to homocysteine metabolism. CBS channels homocysteine toward cysteine and glutathione synthesis, enhancing antioxidant defense, whereas BHMT remethylates homocysteine to methionine, supporting methylation reactions.[75] CBS remained abundant until IC_{70}, while BHMT appeared only from IC_{50} onward. This opposite behavior suggests a metabolic shift from redox defense towards methylation and repair processes at higher doses. It is a transition from acute stress response to adaptive metabolic reprogramming under cytotoxic pressure.

4.2.4 Antagonism study

The purpose of the antagonism study was to examine whether the combination treatment displayed antagonistic interactions, since ATO acts pro-oxidant and **Ir1** pro-reducing. Therefore, a concentration matrix with 36 different mixtures of various ATO and **Ir1** concentrations (**Table 15**) was employed as a viability assay.

Table 15: *Treatment concentrations for antagonism MTT.*

IC (inhibitory concentration)	Ir1 final concentrations [µM]	ATO final concentrations [µM]
Blank	0	0
Cell blank	0	0
IC10	5	3
IC25	20	5
IC50	45	50
IC75	80	120
IC90	90	200

The results of the MTT-Assay with **Ir1** and ATO were evaluated via *SynergyFinder* to evaluate the different mixing ratios. The data set was analyzed with four different synergy score calculation systems. However, since they all work with different mechanisms only ZIP was selected for further evaluation, since ZIP integrates aspects of both Bliss and Loewe and can identify synergistic and antagonistic interactions across different concentration ranges.

To establish the concentration with the highest antagonistic effect, the CI (=combination index) was considered. A combination index >1 indicated an antagonistic effect and <1 a synergistic effect. The highest combination index 1.5 was achieved when cells were treated with 3 µM ATO and 45 µM **Ir1**. Since standard treatments with ATO are performed with 5 µM, further experiments containing both compounds were conducted with 5 µM ATO and 50 µM **Ir1**. The used concentration for **Ir1** is slightly above IC_{50} but was chosen to fit the higher concentration of ATO, leading to a CI of around 1.1. Furthermore, the dose response matrix and a three-dimensional model indicating synergy, when cells are treated with both compounds, were created (**Figure 21**) concluding an antagonistic relation between **Ir1** and ATO.

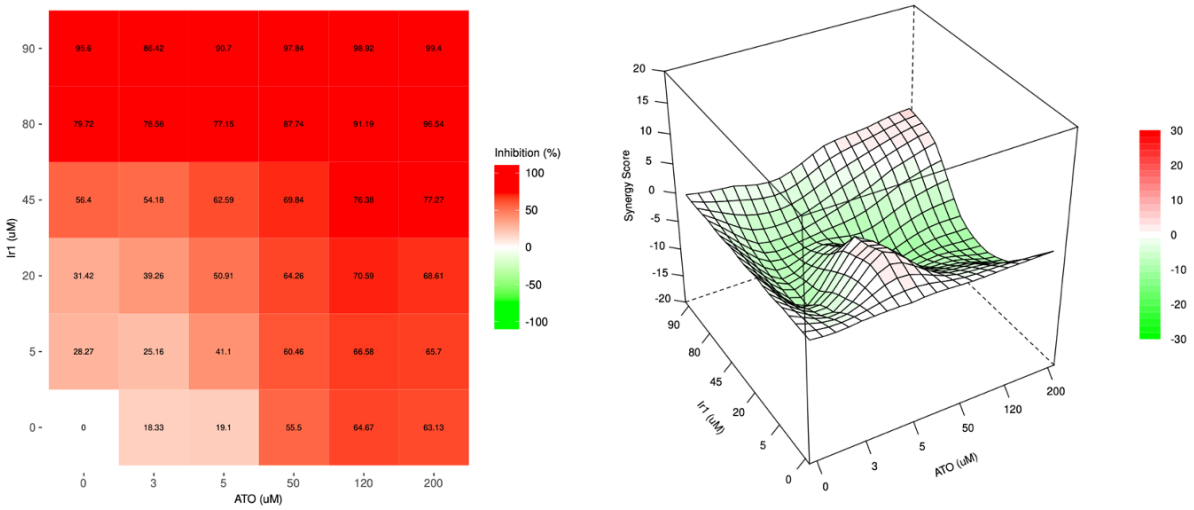

Figure 21: *Dose-response matrix (left, red: high inhibition, green: low inhibition) and ZIP synergy score (right, red: synergistic effect, green: antagonistic effect) for combination treatment.*

After confirming that **Ir1** and ATO share an antagonism, a proteomic experiment was performed to investigate the responsible molecular determinant. For this purpose, SW480 cancer cells were treated with A) DMSO as control, B) 5 µM ATO, C) 50 µM **Ir1**, and D) 50 µM **Ir1** + 5 µM ATO in 6 replicates in 6 well-plates for 24 h. The sample were processed as whole cell lysates and analyzed and evaluated similarly as mentioned above, leading to a total of 5482 identified proteins.

To determine the variance of the different groups, a PCA plot containing the replicates of each treatment (**Figure 22**) was created. The replicates align in a diagonal line in each treatment. Evidently, **Ir1** treatment had only a minor impact on the proteome and these samples clustered close to the controls, while the ATO-

treated cells formed a distinct group. Finally, the combination treatment responsible for the antagonism showed the largest perturbation in the proteome compared to the controls.

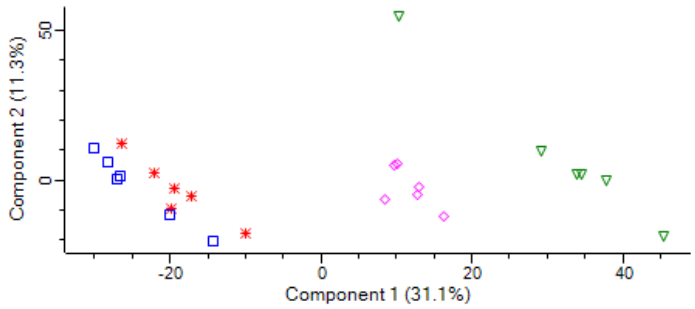

Figure 22: *PCA-plot of WCL antagonism study (blue = control, red = Ir1, pink = ATO, green = combination therapy).*

For further investigation, a coefficient of variation (CV) plot of the data set was generated via Python code (**Figure 23**). The CV distribution shows the CVs of all identified proteins in each condition. Through a CV, the normalized standard deviation is employed. It compares the standard deviation to a measured mean, for proteomics it compares how close multiple measurements from different samples are to each other. The smaller the CV, the lower the deviation compared to the mean and the lower the dispersion. Lower CVs hint to increased reproducibility and increased data quality. Of note, the CV distribution of the combination treatment is slightly worse compared to the controls or single treatments. This can also be seen in the median CV values for each treatment.

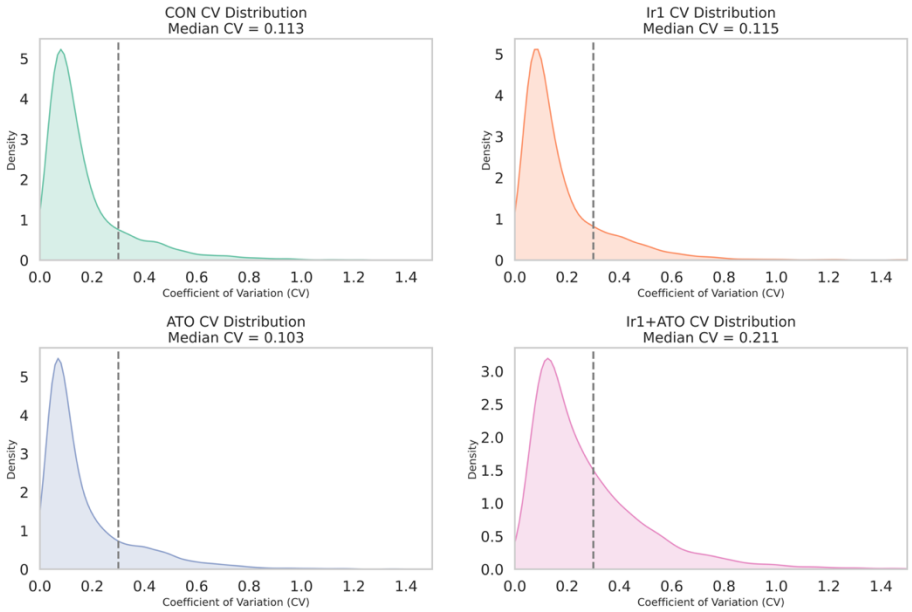

Figure 23: *CV Distribution for each treatment (Control = top left, Ir1 = top right, ATO = bottom left, Combination = bottom right). n=6, 5482 proteins.*

The CVs showed a generally good distribution across all treatment groups. Only the combination treatment data appeared lower in quality compared to the others but was still considered acceptable. In analytical

sciences, a CV of ≤0.3 is generally regarded as the threshold for acceptable reproducibility, as higher values indicate excessive variability and unreliable results, hence the dashed line at 0.3 in the graphs above.[76]

Upregulated proteins

Combination treatment

The goal of the antagonism study is to determine combination specific effects on SW480 cells. To accomplish this, a volcano plot was created to divide the proteins into significantly and non-significantly regulated proteins. Afterwards, the significantly regulated proteins where also filtered into up- and down-regulated proteins. Analysis was started with up-regulated proteins, where proteins were filtered based on their LFQ intensities. The intensities had to be higher in combination therapy than in CON, **Ir1** and ATO treated cells in at least five out of six replicates. Starting from 5362 proteins in total, 2531 were significantly regulated (850 up- and 1691 down-regulated) and only 306 proteins met all the desired criteria. The heatmap with LFQ intensities displayed as Z-scores for each protein is illustrated in **Figure 24**, where each row represents one protein. These proteins were upregulated in the combination treatment versus control and both single treatments are representative of the molecular determinants of the antagonism.

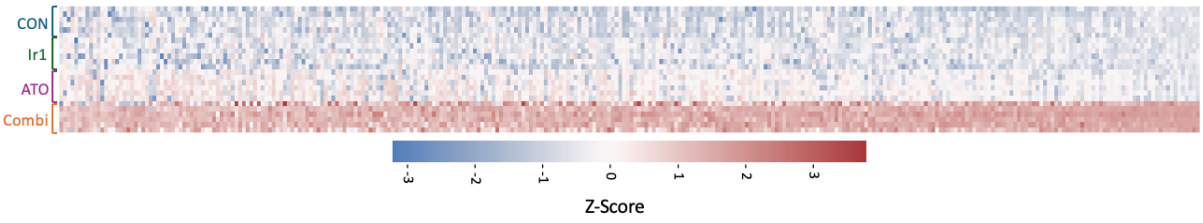

Figure 24: *Heatmap of all proteins where the LFQ-intensities/Z-scores are higher through combination therapy (Combi) than with other treatments (CON=Control, Ir1 = Iridium, ATO = Arsenic trioxide).*

The received 306 proteins list were then uploaded to DAVID, and proteins were sorted into GO biological processes mediated by combination therapy and the top enriched biological processes were displayed as bar plots (**Figure 25**).

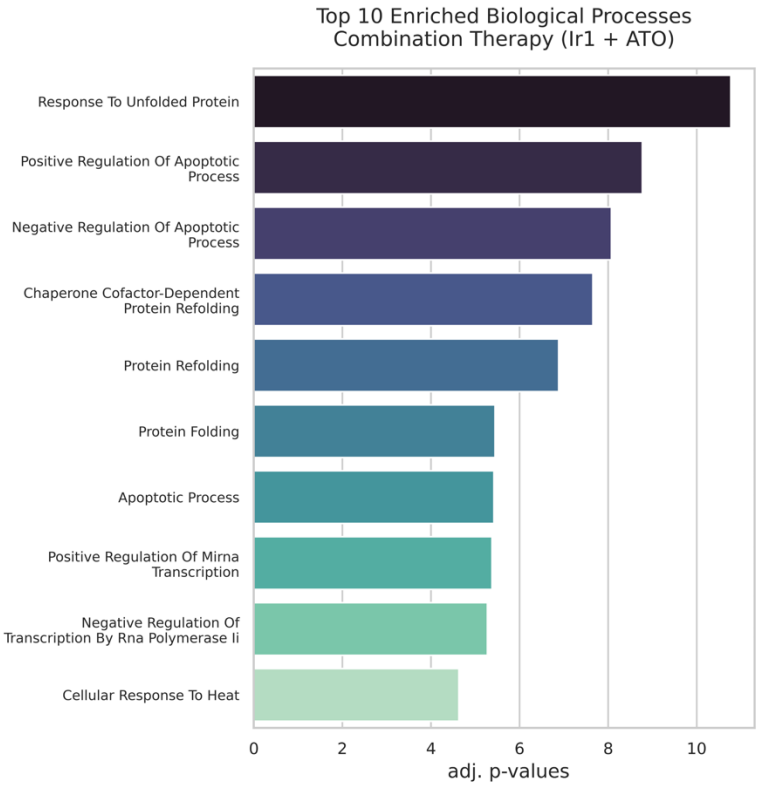

Figure 25: *Top enriched biological processes in SW480 cancer cells trough combination therapy based on significantly upregulated proteins with LFQ intensities higher than in CON, Ir1, ATO in at least 5 out of 6 replicates.*

Unfolded protein response, chaperone-dependent protein folding and heat shock

The unfolded protein response (UPR) is a cellular mechanism that maintains protein-folding homeostasis within the ER. Under normal conditions, the UPR remains inactive, however, it can be triggered by various forms of cellular stress that lead to the accumulation of unfolded or misfolded proteins. In response, the UPR reduces the load of newly synthesized secretory proteins by downregulating their transcription.[77] Combination treatment induces increased reactions to proteotoxic stress, triggering unfolded protein responses and upregulation of molecular chaperones, which is consistent with cellular stress and ER stress and often happens in cancer cells under therapeutic pressure.

Plotting the protein intensities which are associated with the UPR in a heatmap as Z-scores, yielded the results illustrated in **Figure 26**, where each row represents one protein.

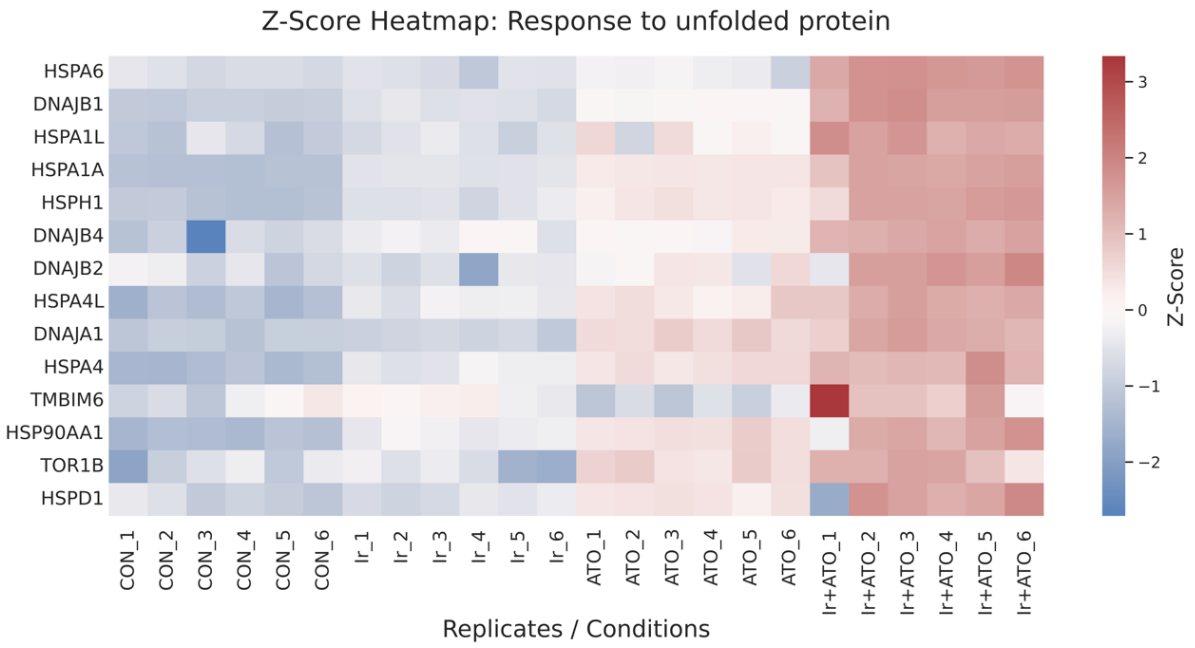

Figure 26: *Heatmap of protein LFQ intensities calculated as Z-Scores for UPR (x-axis = replicates/conditions, y-axis = Gene names).*

The data clearly indicate that the combination therapy results in higher Z-scores than the other treatment conditions. This implies, that the corresponding LFQ intensities are likewise elevated.

Chaperones are like helpers assisting with correct protein folding. They attach to proteins only briefly, relying on non-covalent interactions rather than forming permanent bonds. Certain chaperones also depend on helper molecules called cofactors. With the support of these cofactors and by using energy, they help misfolded proteins back into their proper structure so they can function normally again. The combination treatment led to a stronger upregulation of this process, which suggests that it induces a higher burden of misfolded protein, leading cells to activate chaperone-mediated refolding pathways. The observed effect likely reflects a synergistic interaction between the treatment components.

Cellular response to heat and chaperone mediated protein complex assembly reinforces that combination treatment induces increased response proteotoxic stress, leading to the activation of chaperone systems and heat shock pathways to maintain protein homeostasis.

Apoptotic processes

Furthermore, complex cell death pathways occur. While combination therapy potently activates apoptotic pathways, tumor cells simultaneously mobilize survival responses. Simultaneous pro- and antiapoptotic regulations were detected, where the cancer cell tries to counterbalance the induced stress and maintain viability with a negative regulation of the apoptotic process. As observed for the UPR, the Z-scores for the apoptotic processes also clearly differ under the combination therapy compared to other treatments (**Figure 27**).

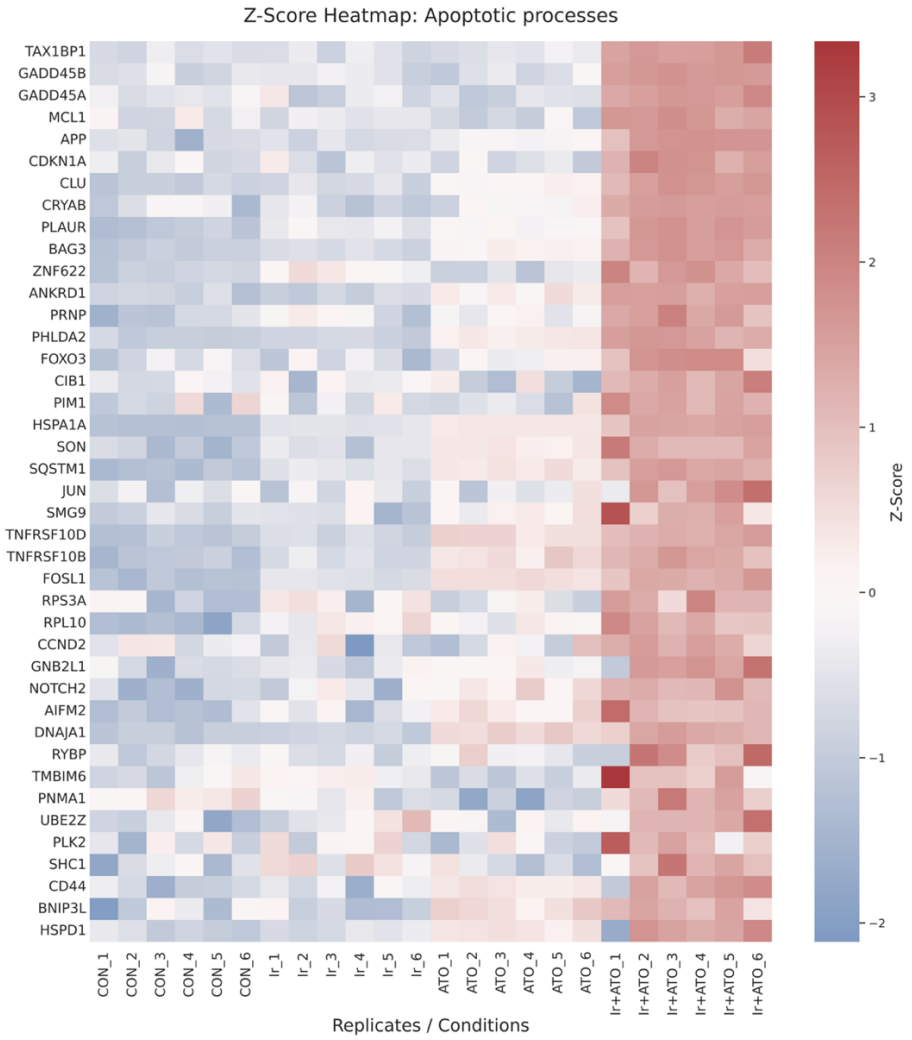

Figure 27: *Heatmap of protein LFQ intensities calculated as Z-Scores for apoptotic processes (x-axis = Gene names, y-axis = replicates/conditions).*

The higher LFQ intensities for proteins involved in positive and negative regulation of apoptosis suggest that the treatment affects several parts of the apoptotic mechanisms at the same time. Cells often activate pro-apoptotic signals and counteracting survival pathways when they experience stress. This pattern likely reflects a mixed cellular response, where apoptosis is triggered, but protective mechanisms are also engaged. This indicates that the combination treatment influences apoptosis in a more complex way than the single treatments. However, the simultaneous regulation of both processes was also observed in the dose-resolved study at IC_{40}-IC_{60} of **Ir1**. The concentration of **Ir1** used for the combination treatment was 50 µM, which is within the concentration range needed for the same effect to be observed in the dose-resolved experiment.

Positive regulation of miRNA transcription (***Figure 28***)

MicroRNAs help reduce or stop the production of proteins that the cell does not currently need, by binding to their messenger RNAs. When this process is positively regulated, a transcription factor detects cellular stress and moves to the DNA, where it activates a gene that produces a specific miRNA. As a result, the cell makes more of this miRNA, which then suppresses the translation of unnecessary proteins. This allows the

cell to adjust its protein production efficiently under stress conditions. The higher LFQ intensities with **Ir1**+ATO regarding positive regulation of miRNA transcription indicate an enhanced activation of post-transcriptional gene regulatory mechanisms.

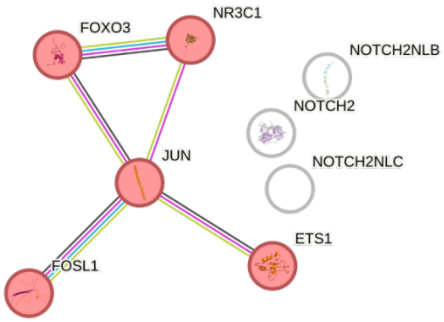

Figure 28: *Positive regulation of miRNA transcription (gene count: 9. Combination treatment, WCL, significantly upregulated proteins, LFQ intensity higher in at least 5 out of 6 replicated than with other treatment).*

Furthermore, proteins appearing in combination treatment only were also filtered and displayed with R (**Figure 29**).

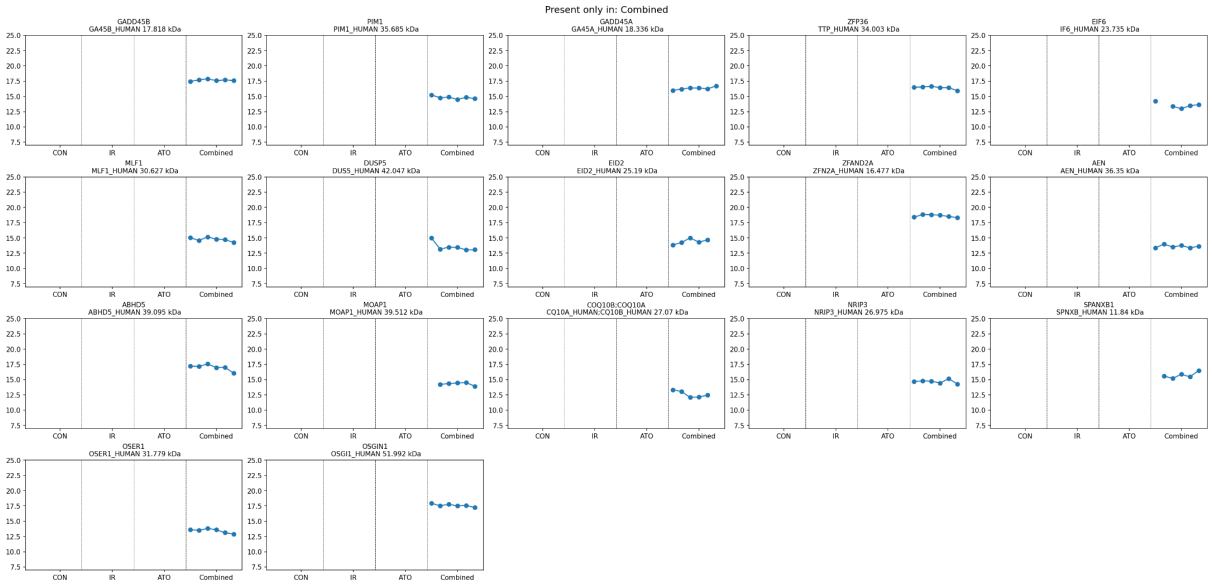

Figure 29: *Proteins appearing in combination treatment only in at least 5 out of 6 replicates. Protein IDs first row (from left to right): GADD45B, PIM1, GADD45A, ZFP36, EIF6. Second row: MLF1, DUSP5, EID2, ZFAND2A, AEN. Third row: ABHD5, MOAP1, COQ10B; COQ10A, NRIP3, SPANXB1. Fourth row: OSER1, OSGIN1.*

Several proteins were detected exclusively in the combination treatment, some of which are associated with central cellular stress pathways, including mitogen-activated protein kinase (MAPK), p53, nuclear factor kappa-light-chain-enhancer of activated B cells (NF-kappa-B) and forkhead-box O (FoxO) signaling pathways. This suggests that, despite the antagonistic combination, the combined treatment induces a unique and more complex stress response that was not triggered by either compound alone. The upregulation of proteins such as growth arrest and DNA-damage-inducible 45 alpha (GADD45A), growth arrest and DNA-damage-inducible protein 45 beta (GADD45B), AEN and modulator of apoptosis 1 (MOAP1) indicates that the combination

treatment led to a state of oxidative stress, as these proteins are established makers of DNA damage signaling and p53 activation. Proteins associated with MAPK-dependent stress responses, including dual-specificity phosphatase 5 (DUSP5), zinc finger protein 36 (ZFP36), zinc finger AN1-type containing 2A (ZFAND2A), oxidative stress-induced growth inhibitor 1 (OSGIN1), and oxidative stress-responsive serine-rich protein 1 (OSER1), point to an intensified activation of adaptive signaling pathways. Although the combination of **Ir1** and ATO produced an antagonistic effect on SW480 cells concerning cell viability, the proteomic profile reveals a pathway synergy. The simultaneous induction of DNA damage, MAPK, NF-kB and FoxO indicates that the combination increasingly activates stress and apoptosis programs more strongly than either agent alone. This highlights the importance of multi-layered readouts in combination studies, as molecular synergism or pathways may occur independently of, and sometimes in opposition to the initial hypothesis.

4.2.5 DCFH-DA Assay

In healthy cells, reactive oxygen species (ROS) are generated in a precisely regulated manner, playing key roles in controlling processes like cell division, immune response, autophagy, inflammation, and stress reactions. However, when ROS production becomes unregulated, it can cause oxidative stress and cytotoxicity, leading to impaired cellular functions and the onset of various diseases, including cancer. ROS have the potential to either promote cell growth or trigger cell death, depending on the level or location of the oxidative burst and the efficiency of the antioxidant system. The impact of ROS on cell growth and cell death largely depends on the strength or duration of redox signaling and the cell's antioxidant defenses. Higher ROS levels in mitochondria can stimulate cell proliferation, survival, migration, and epithelial-mesenchymal transition through pathways like MAPK and Ras-ERK activation.[78]

To assess oxidative stress by quantifying total reactive oxygen species including hydroxyl radicals and nitrogen dioxide, 2',7'-dichlorodihydrofluorescein diacetate (DCFH-DA) staining can be employed. This method involves preparing the DCFH-DA solution, incubating cells with it, and then measuring the normalized fluorescence intensity. DCFH-DA staining is a cost-effective and straightforward approach to detect ROS levels within cells. It is particularly useful for evaluating ROS generation during and post chemical treatments or genetic modifications, thereby aiding in the analysis of cellular oxidative stress under varying environmental conditions and facilitating deeper mechanistic investigations.[79]

DCFH-DA enters cells and undergoes hydrolysis by cellular esterases, releasing DCFH, which cannot escape from the cells anymore. ROS oxidize DCFH to form DCF, which emits green fluorescence at excitation and emission wavelengths of 485 nm and 530 nm, respectively (**Figure 30**). Compared to fluorescence detection with flow cytometry and other methods, using a fluorescence microscope or a plate reader offers distinct advantages. It yields clear fluorescent images and is straightforward, efficient, and cost-effective.[79]

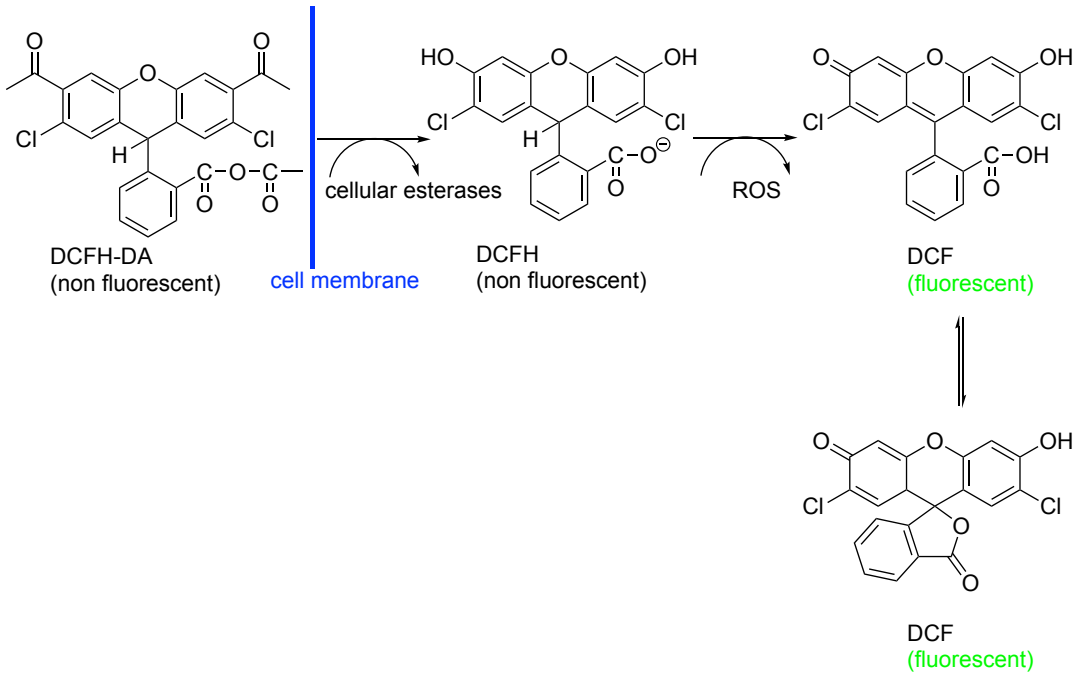

Figure 30: *Chemical reaction of DCFH-DA to DCF inside a viable cell.*[80,81]

The DCFH-DA assays were carried out to determine whether **Ir1** and ATO induce oxidative stress, measured as fluorescence intensity, in SW480 cells and to assess possible effects in combination treatments. After conducting the assays, the results were evaluated with Excel and GraphPadPrism.

The graphs (**Figure 31**) clearly show that, irrespective of the concentration used, ATO induces almost no change in the recorded intensity corresponding to ROS stress. In contrast, treatment with **Ir1** results in a steady increase in relative intensity across all concentrations, with higher concentrations appearing to reinforce this effect. When examining the combination therapy, a noteworthy trend in ROS generation can be observed. The combination of IC_{50} **Ir1** and IC_{25} ATO results in a weaker increase of fluorescence intensity over time than other concentration combinations. Although the effect of the combination therapy on ROS levels did not correlate with prior expectations or assumptions, the observed reduction in intensity increase within this particular combination is reasonable. As discussed in the antagonism study, this specific concentration range induces antagonistic interactions, in which **Ir1** can exert its effect in opposition to ATO.

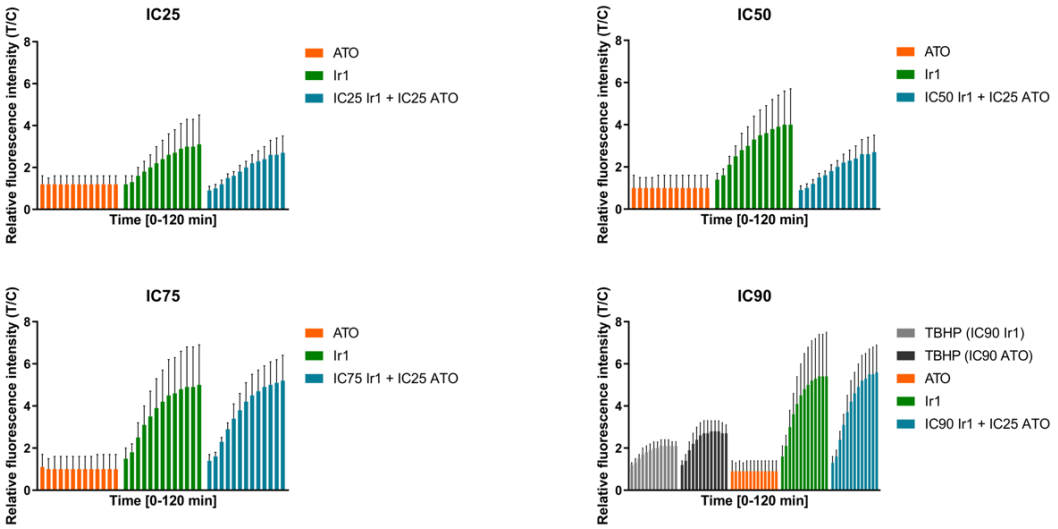

Figure 31: *Bar plots of the relative fluorescence intensities (treatment/control) for each treatment at every measured timepoint. Standard deviations were calculated by three independent replicates (each in triplicates).*

Contrary to all expectation, no ROS species could be detected upon treatment with ATO alone. This raised the question of which ROS species are measured by the DCFH-DA assay, in this case soluble peroxides. ROS species that are membrane- or protein bound cannot be detected using this method. Thus, the DCFH-DA assay is not suitable for detecting oxidative stress specifically induced by ATO, since the ROS species produced by ATO are not of peroxide nature.

The relative fluorescence intensity observed for IC_{90} **Ir1** and the combination of IC_{90} **Ir1** with IC_{25} ATO was even higher than the one measured for the 200 µM (=IC_{90} ATO) positive control. To investigate this, the structure of the fluorescent probe DCFH-DA was analyzed. The dye contains a hydrogen atom that enables fluorescence upon interaction with ROS. As discussed earlier, **Ir1** can convert hydrides, therefore it is reasonable to believe that the assay did not measure the actual ROS production but rather the conversion of DCFH to its fluorescent analogue DCF by **Ir1**. This implies that the intracellular hydride transfer mediated by **Ir1** could potentially be monitored via the reaction of **Ir1** with DCFH-DA over time, thereby providing evidence for its occurrence within cells.

To test this hypothesis, an additional ROS assay was conducted, this time in the absence of cells, to measure the fluorescence intensity resulting solely from the interaction between **Ir1** and DCFH-DA while keeping all other assay conditions identical. The obtained results (**Figure 32**), showed that **Ir1** can indeed directly induce a fluorescence signal in the presence of only DCFH-DA. This provides evidence that the increase in DCF-fluorescence in the presence of **Ir1** may indeed indicate hydride transfer in the cells, contrary to previous studies stating that the high intensities where indicative of immense ROS-stress mediated by Ir(III).[82–84]

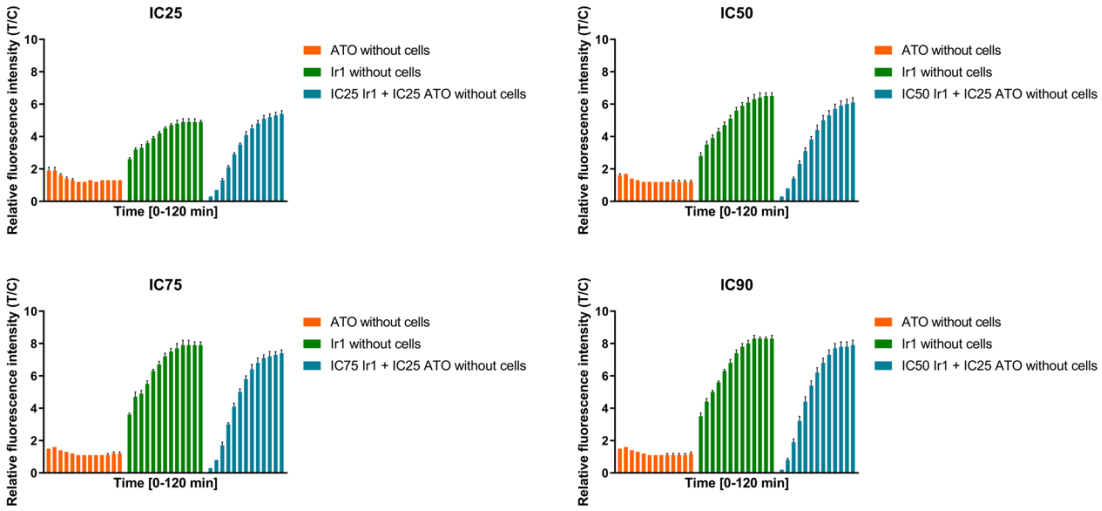

Figure 32: *Bar plots of the relative fluorescence intensities (treatment/control) for each treatment at every measured timepoint without SW480 cancer cells.*

Comparing the cell-free and cell-containing assays with one another, leads to the conclusion that the signal intensity in the cell-free approach were higher compared to the cell-based approach as no washing steps were conducted. The initial hypothesis was approved, nonetheless.

5. Conclusion

This thesis provides a detailed characterization of the catalytic iridium(III) compound **Ir1**, highlighting its chemical and biological activity in the colorectal cancer cell line SW480. At chemical level, **Ir1** was shown to act as a detoxifying agent by mediating hydride transfer reactions that convert reactive aldehyde species, such as 4-HNE, into non-toxic alcohols.

Biologically, **Ir1** displayed a clear dose-dependent response profile in SW480 cancer cells. At $\leq IC_{50}$ concentrations, the proteome reflected subtle metabolic and stress-response adjustments, suggesting that the cells were able to adapt to the presence of the compound. Intermediate treatment concentration, such as IC_{60}, triggered more pronounced changes, including the induction of proteins linked to oxidative stress, mitochondrial remodeling and cell-cycle regulation. Concentrations $\geq IC_{60}$, led to increased apoptosis-related processes, particularly through Bax-associated pathways, indicating that the threshold for irreversible cell death had been surpassed. These results establish **Ir1** as a compound capable of modulating multiple cellular processes in a concentration-dependent manner, with three major biological pathways consistently affected: stress-response signaling (NRF2 and heat shock), apoptosis, and metabolic reactions (Glycolysis, Pentose phosphate pathway, one-carbon metabolism). The regulation of these pathways may represent proteome effects induced by the **Ir1**-mediated hydride transfer.

This motivated the investigation of a combination treatment of **Ir1** exhibiting reducing effects with ATO, which induces oxidative effects, in SW480 cancer cells. Indeed, an antagonistic effect was observed in viability assays, and proteomic profiling demonstrated that the combination treatment activated stress-responses more strongly than either agent alone. Functional annotation highlighted processes including the unfolded protein response and heat shock mechanisms as the primary driver of the antagonistic effect.

ROS assays provided further insights on the oxidate stress in SW480 cancer cells induced by **Ir1** and ATO. While ATO did not induce peroxide-based ROS stress under the tested conditions, **Ir1** and **Ir1**+ATO combination were apparently potent inducers of ROS. However, cell-free studies revealed that these strong fluorescent signals were not due to cellular ROS generation but to a chemical reaction between **Ir1** and the DCFH-DA dye, where the dye serves as a hydride donor. Unexpectedly, these results prove that **Ir1**-mediated transfer hydrogenation reactions occur in cells.

Future research may focus on time-resolved proteomic to capture the dynamic sequence of molecular events triggered by **Ir1**, providing a deeper insight into the temporal regulation of stress-response and apoptotic pathways. Moreover, the beneficial effects of deactivating reactive aldehydes by **Ir1** may be investigated in mouse models.

Taken together, the results of this thesis demonstrate that **Ir1** is a promising catalytic metallodrug with complex biological activity. It combines chemical detoxification capacity with dose-dependent modulation of stress-response, apoptotic and metabolic pathways. The proven mechanism of transfer hydrogenation in cells sets it apart from other traditional chemotherapeutics, offering a novel approach for therapy.

References

(1) Franz, K. J.; Metzler-Nolte, N. Introduction: Metals in Medicine. *Chem. Rev.* **2019**, *119* (2), 727–729. https://doi.org/10.1021/acs.chemrev.8b00685.

(2) Kostova, I. Cytotoxic Organometallic Iridium(III) Complexes. *Molecules* **2025**, *30* (4), 801. https://doi.org/10.3390/molecules30040801.

(3) Yang, T.; Zhu, M.; Jiang, M.; Yang, F.; Zhang, Z. Current Status of Iridium-Based Complexes against Lung Cancer. *Front. Pharmacol.* **2022**, *13*, 1025544. https://doi.org/10.3389/fphar.2022.1025544.

(4) Romero-Canelón, I.; Sadler, P. J. Next-Generation Metal Anticancer Complexes: Multitargeting via Redox Modulation. *Inorg. Chem.* **2013**, *52* (21), 12276–12291. https://doi.org/10.1021/ic400835n.

(5) Szymaszek, P.; Tyszka-Czochara, M.; Ortyl, J. Iridium(III) Complexes as Novel Theranostic Small Molecules for Medical Diagnostics, Precise Imaging at a Single Cell Level and Targeted Anticancer Therapy. *Eur. J. Med. Chem.* **2024**, *276*, 116648. https://doi.org/10.1016/j.ejmech.2024.116648.

(6) Kyrkou, S. G.; Vrettos, E. I.; Gorpas, D.; Crook, T.; Syed, N.; Tzakos, A. G. Design Principles Governing the Development of Theranostic Anticancer Agents and Their Nanoformulations with Photoacoustic Properties. *Pharmaceutics* **2022**, *14* (2), 362. https://doi.org/10.3390/pharmaceutics14020362.

(7) Liu, Z.; Romero-Canelón, I.; Qamar, B.; Hearn, J. M.; Habtemariam, A.; Barry, N. P. E.; Pizarro, A. M.; Clarkson, G. J.; Sadler, P. J. The Potent Oxidant Anticancer Activity of Organoiridium Catalysts. *Angew. Chem. Int. Ed.* **2014**, *53* (15), 3941–3946. https://doi.org/10.1002/anie.201311161.

(8) Jana, R. D.; Ngo, A. H.; Bose, S.; Do, L. H. Organoiridium Complexes Enhance Cellular Defense Against Reactive Aldehydes Species. *Chem. – Eur. J.* **2023**, *29* (36), e202300842. https://doi.org/10.1002/chem.202300842.

(9) Uchida, K. 4-Hydroxy-2-Nonenal: A Product and Mediator of Oxidative Stress. *Prog. Lipid Res.* **2003**, *42* (4), 318–343. https://doi.org/10.1016/S0163-7827(03)00014-6.

(10) Ahmed Laskar, A.; Younus, H. Aldehyde Toxicity and Metabolism: The Role of Aldehyde Dehydrogenases in Detoxification, Drug Resistance and Carcinogenesis. *Drug Metab. Rev.* **2019**, *51* (1), 42–64. https://doi.org/10.1080/03602532.2018.1555587.

(11) Sayre, L. M.; Perry, G.; Smith, M. A. Oxidative Stress and Neurotoxicity. *Chem. Res. Toxicol.* **2008**, *21* (1), 172–188. https://doi.org/10.1021/tx700210j.

(12) Jana, R. D.; Ngo, A. H.; Bose, S.; Do, L. H. Organoiridium Complexes Enhance Cellular Defense Against Reactive Aldehydes Species. *Chem. – Eur. J.* **2023**, *29* (36), e202300842. https://doi.org/10.1002/chem.202300842.

(13) Yang, S.; Raza, F.; Li, K.; Qiu, Y.; Su, J.; Qiu, M. Maximizing Arsenic Trioxide's Anticancer Potential: Targeted Nanocarriers for Solid Tumor Therapy. *Colloids Surf. B Biointerfaces* **2024**, *241*, 114014. https://doi.org/10.1016/j.colsurfb.2024.114014.

(14) De Almeida, T. D.; Evangelista, F. C. G.; Sabino, A. D. P. Acute Promyelocytic Leukemia (APL): A Review of the Classic and Emerging Target Therapies towards Molecular Heterogeneity. *Future Pharmacol.* **2023**, *3* (1), 162–179. https://doi.org/10.3390/futurepharmacol3010012.

(15) Trisennox: Arsenic Trioxide, 2017.

(16) Stevens, J. J.; Graham, B.; Dugo, E.; Sumner, B. B.; Ndebele, K.; Tchounwou, P. B. Arsenic Trioxide Induces Apoptosis via Specific Signaling Pathways in HT- 29 Colon Cancer Cells. *J. Cancer Sci. Ther.* **2017**, *09* (01). https://doi.org/10.4172/1948-5956.1000432.

(17) Sun, Z.; Li, M.; Bai, L.; Fu, J.; Lu, J.; Wu, M.; Zhou, C.; Zhang, Y.; Wu, Y. Arsenic Trioxide Inhibits Angiogenesis in Vitro and in Vivo by Upregulating FoxO3a. *Toxicol. Lett.* **2019**, *315*, 1–8. https://doi.org/10.1016/j.toxlet.2019.08.009.

(18) Caesar, L. K.; Cech, N. B. Synergy and Antagonism in Natural Product Extracts: When 1 + 1 Does Not Equal 2. *Nat. Prod. Rep.* **2019**, *36* (6), 869–888. https://doi.org/10.1039/C9NP00011A.

(19) Pemovska, T.; Bigenzahn, J. W.; Superti-Furga, G. Recent Advances in Combinatorial Drug Screening and Synergy Scoring. *Curr. Opin. Pharmacol.* **2018**, *42*, 102–110. https://doi.org/10.1016/j.coph.2018.07.008.

(20) Saputra, E. C.; Huang, L.; Chen, Y.; Tucker-Kellogg, L. Combination Therapy and the Evolution of Resistance: The Theoretical Merits of Synergism and Antagonism in Cancer. *Cancer Res.* **2018**, *78* (9), 2419–2431. https://doi.org/10.1158/0008-5472.CAN-17-1201.

(21) Yin, N.; Ma, W.; Pei, J.; Ouyang, Q.; Tang, C.; Lai, L. Synergistic and Antagonistic Drug Combinations Depend on Network Topology. *PLoS ONE* **2014**, *9* (4), e93960. https://doi.org/10.1371/journal.pone.0093960.

(22) Previtali, V.; Bagnolini, G.; Ciamarone, A.; Ferrandi, G.; Rinaldi, F.; Myers, S. H.; Roberti, M.; Cavalli, A. New Horizons of Synthetic Lethality in Cancer: Current Development and Future Perspectives. *J. Med. Chem.* **2024**, *67* (14), 11488–11521. https://doi.org/10.1021/acs.jmedchem.4c00113.

(23) Ngoi, Y. L. N.; Gallo, D.; Torrado, C.; Nardo, M.; Durocher, D.; Yap, T. A. Synthetic Lethal Strategies for the Development of Cancer Therapeutics. *Nat. Rev. Clin. Oncol.* **2025**, No. 22, 46–64. https://doi-org.uaccess.univie.ac.at/10.1038/s41571-024-00966-z.

(24) Schäffer, A. A.; Chung, Y.; Kammula, A. V.; Ruppin, E.; Lee, J. S. A Systematic Analysis of the Landscape of Synthetic Lethality-Driven Precision Oncology. *Med* **2024**, *5* (1), 73-89.e9. https://doi.org/10.1016/j.medj.2023.12.009.

(25) Duarte, D.; Vale, N. Evaluation of Synergism in Drug Combinations and Reference Models for Future Orientations in Oncology. *Curr. Res. Pharmacol. Drug Discov.* **2022**, *3*, 100110. https://doi.org/10.1016/j.crphar.2022.100110.

(26) Yadav, B.; Wennerberg, K.; Aittokallio, T.; Tang, J. Searching for Drug Synergy in Complex Dose–Response Landscapes Using an Interaction Potency Model. *Comput. Struct. Biotechnol. J.* **2015**, *13*, 504–513. https://doi.org/10.1016/j.csbj.2015.09.001.

(27) Vlot, A. H. C.; Aniceto, N.; Menden, M. P.; Ulrich-Merzenich, G.; Bender, A. Applying Synergy Metrics to Combination Screening Data: Agreements, Disagreements and Pitfalls. *Drug Discov. Today* **2019**, *24* (12), 2286–2298. https://doi.org/10.1016/j.drudis.2019.09.002.

(28) Tang, J.; Wennerberg, K.; Aittokallio, T. What Is Synergy? The Saariselkä Agreement Revisited. *Front. Pharmacol.* **2015**, *6*. https://doi.org/10.3389/fphar.2015.00181.

(29) Yin, N.; Ma, W.; Pei, J.; Ouyang, Q.; Tang, C.; Lai, L. Synergistic and Antagonistic Drug Combinations Depend on Network Topology. *PLoS ONE* **2014**, *9* (4), e93960. https://doi.org/10.1371/journal.pone.0093960.

(30) Chen, J.; Lin, A.; Jiang, A.; Qi, C.; Liu, Z.; Cheng, Q.; Yuan, S.; Luo, P. Computational Frameworks Transform Antagonism to Synergy in Optimizing Combination Therapies. *Npj Digit. Med.* **2025**, *8* (1), 44. https://doi.org/10.1038/s41746-025-01435-2.

(31) Han, X.; Aslanian, A.; Yates, J. R. Mass Spectrometry for Proteomics. *Curr. Opin. Chem. Biol.* **2008**, *12* (5), 483–490. https://doi.org/10.1016/j.cbpa.2008.07.024.

(32) Domon, B.; Aebersold, R. Mass Spectrometry and Protein Analysis. *Science* **2006**, *312* (5771), 212–217. https://doi.org/10.1126/science.1124619.

(33) Tesfaye, E.; Ashenef, A.; Hymete, A.; Niguss, T. Theory and Recent Applications of Nano-Liquid Chromatography. In *Relevant Applications of High-Performance Liquid Chromatography in Food, Environmental, Clinical and Biological Fields*; Núñez, O., Ed.; IntechOpen, 2024. https://doi.org/10.5772/intechopen.1006657.

(34) Asensio-Ramos, M.; Fanali, C.; D'Orazio, G.; Fanali, S. Nano-Liquid Chromatography. In *Liquid Chromatography*; Elsevier, 2017; pp 637–695. https://doi.org/10.1016/B978-0-12-805393-5.00027-0.

(35) Berg, J. M.; Tymoczko, J. L.; Gatto, G. J.; Stryer, L. *Stryer Biochemie*; Springer Berlin Heidelberg: Berlin, Heidelberg, 2018. https://doi.org/10.1007/978-3-662-54620-8.

(36) Chen, T.; Yao, Q.; Nasaruddin, R. R.; Xie, J. Electrospray Ionization Mass Spectrometry: A Powerful Platform for Noble-Metal Nanocluster Analysis. *Angew. Chem. Int. Ed.* **2019**, *58* (35), 11967–11977. https://doi.org/10.1002/anie.201901970.

(37) Konermann, L.; Ahadi, E.; Rodriguez, A. D.; Vahidi, S. Unraveling the Mechanism of Electrospray Ionization. *Anal. Chem.* **2013**, *85* (1), 2–9. https://doi.org/10.1021/ac302789c.

(38) Bruker. *CaptiveSpray 2 and CaptiveSpray Ultra 2*. https://www.bruker.com/en/products-and-solutions/mass-spectrometry/ion-sources/captivespray.html (accessed 2025-11-21).

(39) Time-of-Flight Mass Spectrometry : Technical Overview, 2011.

(40) Arevalo, R.; Ni, Z.; Danell, R. M. Mass Spectrometry and Planetary Exploration: A Brief Review and Future Projection. *J. Mass Spectrom.* **2020**, *55* (1), e4454. https://doi.org/10.1002/jms.4454.

(41) Schermann, J. P. Spectroscopy and Modelling of Biomolecular Building Blocks; Elsevier Science, 2008; pp 129–207.

(42) Yu, F.; Haynes, S. E.; Teo, G. C.; Avtonomov, D. M.; Polasky, D. A.; Nesvizhskii, A. I. Fast Quantitative Analysis of timsTOF PASEF Data with MSFragger and IonQuant. *Mol. Cell. Proteomics* **2020**, *19* (9), 1575–1585. https://doi.org/10.1074/mcp.TIR120.002048.

(43) Meier, F.; Beck, S.; Grassl, N.; Lubeck, M.; Park, M. A.; Raether, O.; Mann, M. Parallel Accumulation–Serial Fragmentation (PASEF): Multiplying Sequencing Speed and Sensitivity by Synchronized Scans in a Trapped Ion Mobility Device. *J. Proteome Res.* **2015**, *14* (12), 5378–5387. https://doi.org/10.1021/acs.jproteome.5b00932.

(44) Jacobs, A.; Andreoiu, C.; Bergmann, J.; Brunner, T.; Dickel, T.; Dillmann, I.; Dunling, E.; Flowerdew, J.; Graham, L.; Gwinner, G.; Hockenbery, Z.; Kootte, B.; Lan, Y.; Leach, K. G.; Leistenschneider, E.; Lykiardopoulou, E. M.; Monier, V.; Mukul, I.; Paul, S. F.; Plaß, W. R.; Reiter, M. P.; Scheidenberger, C.; Thompson, R.; Tracy, J. L.; Will, C.; Wieser, M. E.; Yavor, M.; Dilling, J.; Kwiatkowski, A. A. Collision-Induced Dissociation at TRIUMF's Ion Trap for Atomic and Nuclear Science. *Int. J. Mass Spectrom.* **2022**, *482*, 116931. https://doi.org/10.1016/j.ijms.2022.116931.

(45) Kellmann, M.; Muenster, H.; Zomer, P.; Mol, H. Full Scan MS in Comprehensive Qualitative and Quantitative Residue Analysis in Food and Feed Matrices: How Much Resolving Power Is Required? *J. Am. Soc. Mass Spectrom.* **2009**, *20* (8), 1464–1476. https://doi.org/10.1016/j.jasms.2009.05.010.

(46) Rogers, J. C.; Bomgarden, R. D. Sample Preparation for Mass Spectrometry-Based Proteomics; from Proteomes to Peptides. In *Modern Proteomics – Sample Preparation, Analysis and Practical Applications*; Mirzaei, H., Carrasco, M., Eds.; Advances in Experimental Medicine and Biology; Springer International Publishing: Cham, 2016; Vol. 919, pp 43–62. https://doi.org/10.1007/978-3-319-41448-5_3.

(47) Mathew, A.; Eijkel, G. B.; Anthony, I. G. M.; Ellis, S. R.; Heeren, R. M. A. Characterization of Microchannel Plate Detector Response for the Detection of Native Multiply Charged High Mass Single Ions in Orthogonal-time-of-flight Mass Spectrometry Using a TIMEPIX Detector. *J. Mass Spectrom.* **2022**, *57* (4), e4820. https://doi.org/10.1002/jms.4820.

(48) Al-Amrani, S.; Al-Jabri, Z.; Al-Zaabi, A.; Alshekaili, J.; Al-Khabori, M. Proteomics: Concepts and Applications in Human Medicine. *World J. Biol. Chem.* **2021**, *12* (5), 57–69. https://doi.org/10.4331/wjbc.v12.i5.57.

(49) Megger, D. A.; Bracht, T.; Meyer, H. E.; Sitek, B. Label-Free Quantification in Clinical Proteomics. *Biochim. Biophys. Acta BBA - Proteins Proteomics* **2013**, *1834* (8), 1581–1590. https://doi.org/10.1016/j.bbapap.2013.04.001.

(50) Kreutz, D.; Bileck, A.; Plessl, K.; Wolrab, D.; Groessl, M.; Keppler, B. K.; Meier, S. M.; Gerner, C. Response Profiling Using Shotgun Proteomics Enables Global Metallodrug Mechanisms of Action To Be Established. *Chem. – Eur. J.* **2017**, *23* (8), 1881–1890. https://doi.org/10.1002/chem.201604516.

(51) Jiang, Y.; Rex, D. A. B.; Schuster, D.; Neely, B. A.; Rosano, G. L.; Volkmar, N.; Momenzadeh, A.; Peters-Clarke, T. M.; Egbert, S. B.; Kreimer, S.; Doud, E. H.; Crook, O. M.; Yadav, A. K.; Vanuopadath, M.; Hegeman, A. D.; Mayta, M. L.; Duboff, A. G.; Riley, N. M.; Moritz, R. L.; Meyer, J. G. Comprehensive Overview of Bottom-Up Proteomics Using Mass Spectrometry. *ACS Meas. Sci. Au* **2024**, *4* (4), 338–417. https://doi.org/10.1021/acsmeasuresciau.3c00068.

(52) Guo, J.; Huan, T. Comparison of Full-Scan, Data-Dependent, and Data-Independent Acquisition Modes in Liquid Chromatography–Mass Spectrometry Based Untargeted Metabolomics. *Anal. Chem.* **2020**, *92* (12), 8072–8080. https://doi.org/10.1021/acs.analchem.9b05135.

(53) Fernández-Costa, C.; Martínez-Bartolomé, S.; McClatchy, D. B.; Saviola, A. J.; Yu, N.-K.; Yates, J. R. Impact of the Identification Strategy on the Reproducibility of the DDA and DIA Results. *J. Proteome Res.* **2020**, *19* (8), 3153–3161. https://doi.org/10.1021/acs.jproteome.0c00153.

(54) Anand, S.; Samuel, M.; Ang, C.-S.; Keerthikumar, S.; Mathivanan, S. Label-Based and Label-Free Strategies for Protein Quantitation. In *Proteome Bioinformatics*; Keerthikumar, S., Mathivanan, S., Eds.; Methods in Molecular Biology; Springer New York: New York, NY, 2017; Vol. 1549, pp 31–43. https://doi.org/10.1007/978-1-4939-6740-7_4.

(55) Bantscheff, M.; Schirle, M.; Sweetman, G.; Rick, J.; Kuster, B. Quantitative Mass Spectrometry in Proteomics: A Critical Review. *Anal. Bioanal. Chem.* **2007**, *389* (4), 1017–1031. https://doi.org/10.1007/s00216-007-1486-6.

(56) Bortel, P.; Hagn, G.; Skos, L.; Bileck, A.; Paulitschke, V.; Paulitschke, P.; Gleiter, L.; Mohr, T.; Gerner, C.; Meier-Menches, S. M. Memory Effects of Prior Subculture May Impact the Quality of Multiomic Perturbation Profiles. *Proc. Natl. Acad. Sci.* **2024**, *121* (29), e2313851121. https://doi.org/10.1073/pnas.2313851121.

(57) O'Hare, S.; Atterwill, C. K. In Vitro Toxicity Testing Protocols. In *Methods in Molecular Biology*; Humana Press Inc, 1995; pp 137–149.

(58) Kumar, P.; Nagarajan, A.; Uchil, P. D. Analysis of Cell Viability by the MTT Assay. *Cold Spring Harb. Protoc.* **2018**, *2018* (6), pdb.prot095505. https://doi.org/10.1101/pdb.prot095505.

(59) Kuete, V.; Karaosmanoğlu, O.; Sivas, H. Anticancer Activities of African Medicinal Spices and Vegetables. In *Medicinal Spices and Vegetables from Africa: Therapeutic Potential against Metabolic, Inflammatory, Infectious and Systemic Diseases*; Elsevier Inc., 2017; pp 271–297.

(60) Jomova, K.; Alomar, S. Y.; Valko, R.; Fresser, L.; Nepovimova, E.; Kuca, K.; Valko, M. Interplay of Oxidative Stress and Antioxidant Mechanisms in Cancer Development and Progression. *Arch. Toxicol.* **2025**. https://doi.org/10.1007/s00204-025-04146-5.

(61) Zheng, H.; Long, G.; Zheng, Y.; Yang, X.; Cai, W.; He, S.; Qin, X.; Liao, H. Glycolysis-Related SLC2A1 Is a Potential Pan-Cancer Biomarker for Prognosis and Immunotherapy. *Cancers* **2022**, *14* (21), 5344. https://doi.org/10.3390/cancers14215344.

(62) Kampinga, H. H.; Hageman, J.; Vos, M. J.; Kubota, H.; Tanguay, R. M.; Bruford, E. A.; Cheetham, M. E.; Chen, B.; Hightower, L. E. Guidelines for the Nomenclature of the Human Heat Shock Proteins. *Cell Stress Chaperones* **2009**, *14* (1), 105–111. https://doi.org/10.1007/s12192-008-0068-7.

(63) Qi, M.; Zhang, J.; Zeng, W.; Chen, X. DNAJB1 Stabilizes MDM2 and Contributes to Cancer Cell Proliferation in a P53-Dependent Manner. *Biochim. Biophys. Acta BBA - Gene Regul. Mech.* **2014**, *1839* (1), 62–69. https://doi.org/10.1016/j.bbagrm.2013.12.003.

(64) Bhasin, N.; Dabral, P.; Senavirathna, L.; Pan, S.; Chen, R. Inhibition of TRAP1 Accelerates the DNA Damage Response, Activation of the Heat Shock Response and Metabolic Reprogramming in Colon Cancer Cells. *Front. Biosci.-Landmark* **2023**, *28* (9), 227. https://doi.org/10.31083/j.fbl2809227.

(65) Chen, X.; Zhang, T.; Su, W.; Dou, Z.; Zhao, D.; Jin, X.; Lei, H.; Wang, J.; Xie, X.; Cheng, B.; Li, Q.; Zhang, H.; Di, C. Mutant P53 in Cancer: From Molecular Mechanism to Therapeutic Modulation. *Cell Death Dis.* **2022**, *13* (11), 974. https://doi.org/10.1038/s41419-022-05408-1.

(66) Gao, K.; Yu, L.; Wang, L.; Gao, L.; Li, T.; Sun, J. Investigation of Biomarkers and Associated Molecular Mechanism Shared between Colorectal Cancer and Lung Adenocarcinoma. *Discov. Oncol.* **2025**, *16* (1), 1540. https://doi.org/10.1007/s12672-025-03240-5.

(67) Robinson, K. S.; Sennhenn, P.; Yuan, D. S.; Liu, H.; Taddei, D.; Qian, Y.; Luo, W. TMBIM6/BI-1 Is an Intracellular Environmental Regulator That Induces Paraptosis in Cancer via ROS and Calcium-Activated ERAD II Pathways. *Oncogene* **2025**, *44* (8), 494–512. https://doi.org/10.1038/s41388-024-03222-x.

(68) Chinnadurai, G.; Vijayalingam, S.; Rashmi, R. BIK, the Founding Member of the BH3-Only Family Proteins: Mechanisms of Cell Death and Role in Cancer and Pathogenic Processes. *Oncogene* **2008**, *27* (S1), S20–S29. https://doi.org/10.1038/onc.2009.40.

(69) Zhou, D.; Duan, Z.; Li, Z.; Ge, F.; Wei, R.; Kong, L. The Significance of Glycolysis in Tumor Progression and Its Relationship with the Tumor Microenvironment. *Front. Pharmacol.* **2022**, *13*, 1091779. https://doi.org/10.3389/fphar.2022.1091779.

(70) Backe, P. H.; Laerdahl, J. K.; Kittelsen, L. S.; Dalhus, B.; Mørkrid, L.; Bjørås, M. Structural Basis for Substrate and Product Recognition in Human Phosphoglucomutase-1 (PGM1) Isoform 2, a Member of the α-d-Phosphohexomutase Superfamily. *Sci. Rep.* **2020**, *10* (1), 5656. https://doi.org/10.1038/s41598-020-62548-0.

(71) Zapater, J. L.; Lednovich, K. R.; Khan, Md. W.; Pusec, C. M.; Layden, B. T. Hexokinase Domain-Containing Protein-1 in Metabolic Diseases and Beyond. *Trends Endocrinol. Metab.* **2022**, *33* (1), 72–84. https://doi.org/10.1016/j.tem.2021.10.006.

(72) Ghanem, N.; El-Baba, C.; Araji, K.; El-Khoury, R.; Usta, J.; Darwiche, N. The Pentose Phosphate Pathway in Cancer: Regulation and Therapeutic Opportunities. *Chemotherapy* **2021**, *66* (5–6), 179–191. https://doi.org/10.1159/000519784.

(73) Xu, X.; Zur Hausen, A.; Coy, J. F.; Löchelt, M. Transketolase-like Protein 1 (TKTL1) Is Required for Rapid Cell Growth and Full Viability of Human Tumor Cells. *Int. J. Cancer* **2009**, *124* (6), 1330–1337. https://doi.org/10.1002/ijc.24078.

(74) Geng, Y. Unveiling the Oncogenic Significance of Thymidylate Synthase in Human Cancers. *Am. J. Transl. Res.* **2024**, *16* (10), 5228–5247. https://doi.org/10.62347/IRUZ1011.

(75) Huang, X.; Li, D.; Zhao, Q.; Zhang, C.; Ren, B.; Yue, L.; Du, B.; Godfrey, O.; Wang, X.; Zhang, W. Association between BHMT and CBS Gene Promoter Methylation with the Efficacy of Folic Acid Therapy in Patients with Hyperhomocysteinemia. *J. Hum. Genet.* **2019**, *64* (12), 1227–1235. https://doi.org/10.1038/s10038-019-0672-7.

(76) Ensuring Reproducibility in Proteomics: Why Coefficient of Variation Is a Critical Metric, 2023.

(77) Read, A.; Schröder, M. The Unfolded Protein Response: An Overview. *Biology* **2021**, *10* (5), 384. https://doi.org/10.3390/biology10050384.

(78) Sahoo, B. M.; Banik, B. K.; Borah, P.; Jain, A. Reactive Oxygen Species (ROS): Key Components in Cancer Therapies. *Anticancer Agents Med. Chem.* **2022**, *22* (2), 215–222. https://doi.org/10.2174/1871520621666210608095512.

(79) Kim, H.; Xue, X. Detection of Total Reactive Oxygen Species in Adherent Cells by 2',7'-Dichlorodihydrofluorescein Diacetate Staining. *J. Vis. Exp.* **2020**, No. 160, 60682. https://doi.org/10.3791/60682.

(80) Nova, Z.; Skovierova, H.; Strnadel, J.; Halasova, E.; Calkovska, A. Short-Term versus Long-Term Culture of A549 Cells for Evaluating the Effects of Lipopolysaccharide on Oxidative Stress, Surfactant Proteins and Cathelicidin LL-37. *Int. J. Mol. Sci.* **2020**, *21* (3), 1148. https://doi.org/10.3390/ijms21031148.

(81) Ezequiel, J.; Nitschke, M. R.; Laviale, M.; Serôdio, J.; Frommlet, J. C. Concurrent Bioimaging of Microalgal Photophysiology and Oxidative Stress. *Photosynth. Res.* **2023**, *155* (2), 177–190. https://doi.org/10.1007/s11120-022-00989-6.

(82) Banerjee, S.; Sadler, P. J. Transfer Hydrogenation Catalysis in Cells. *RSC Chem. Biol.* **2021**, *2* (1), 12–29. https://doi.org/10.1039/D0CB00150C.

(83) Soldevila-Barreda, J. J.; Romero-Canelón, I.; Habtemariam, A.; Sadler, P. J. Transfer Hydrogenation Catalysis in Cells as a New Approach to Anticancer Drug Design. *Nat. Commun.* **2015**, *6* (1), 6582. https://doi.org/10.1038/ncomms7582.

(84) Fry, M. E.; Alsaif, S. A.; Khanom, Y.; Keirle, A. K.; Pheasey, C. E.; Song, J. I.; Bedford, R. A.; Romero-Canelon, I.; Sadler, P. J.; Coverdale, J. P. C. Ir(III) Diamine Transfer Hydrogenation Catalysts in Cancer Cells. *ChemCatChem* **2025**, *17* (2), e202401490. https://doi.org/10.1002/cctc.202401490.

Appendix

Dose-resolved proteomics

Table 16: Protein quantification of dose-resolved proteomics samples with BCA-Assay.

Sample Nr.	Condition	c [µg/µl]	Approx. total sample V [µl]	Protein amount [µg]	V for 20µg Protein [µl]	Add SDC to reach a total V of 90µl [µl]
1	SW480_WCL_CON1	1.79	90	20	11.2	78.8
2	SW480_WCL_CON2	1.85	90	20	10.8	79.2
3	SW480_WCL_CON3	2.10	90	20	9.5	80.5
4	SW480_WCL_CON4	1.85	90	20	10.8	79.2
5	SW480_WCL_IC10_1	2.07	90	20	9.7	80.3
6	SW480_WCL_IC10_2	2.08	90	20	9.6	80.4
7	SW480_WCL_IC10_3	1.92	90	20	10.4	79.6
8	SW480_WCL_IC10_4	2.08	90	20	9.6	80.4
9	SW480_WCL_IC20_1	1.75	90	20	11.5	78.5
10	SW480_WCL_IC20_2	2.29	90	20	8.7	81.3
11	SW480_WCL_IC20_3	2.27	90	20	8.8	81.2
12	SW480_WCL_IC20_4	2.27	90	20	8.8	81.2
13	SW480_WCL_IC30_1	1.80	90	20	11.1	78.9
14	SW480_WCL_IC30_2	2.05	90	20	9.8	80.2
15	SW480_WCL_IC30_3	1.90	90	20	10.5	79.5
16	SW480_WCL_IC30_4	1.90	90	20	10.5	79.5
17	SW480_WCL_IC40_1	2.00	90	20	10.0	80.0
18	SW480_WCL_IC40_2	1.90	90	20	10.5	79.5
19	SW480_WCL_IC40_3	1.90	90	20	10.5	79.5
20	SW480_WCL_IC40_4	1.70	90	20	11.8	78.2
21	SW480_WCL_IC50_1	1.45	90	20	13.8	76.2
22	SW480_WCL_IC50_2	1.56	90	20	12.8	77.2
23	SW480_WCL_IC50_3	1.72	90	20	11.7	78.3
24	SW480_WCL_IC50_4	1.56	90	20	12.8	77.2
25	SW480_WCL_IC60_1	2.30	90	20	8.7	81.3
26	SW480_WCL_IC60_2	2.19	90	20	9.1	80.9
27	SW480_WCL_IC60_3	1.91	90	20	10.5	79.5
28	SW480_WCL_IC60_4	2.25	90	20	8.9	81.1
29	SW480_WCL_IC70_1	1.09	90	20	18.3	71.7
30	SW480_WCL_IC70_2	1.18	90	20	16.9	73.1
31	SW480_WCL_IC70_3	1.26	90	20	15.9	74.1
32	SW480_WCL_IC70_4	0.96	90	20	20.8	69.2
33	SW480_WCL_IC80_1	1.18	90	20	16.9	73.1
34	SW480_WCL_IC80_2	1.15	90	20	17.4	72.6
35	SW480_WCL_IC80_3	1.03	90	20	19.5	70.5
36	SW480_WCL_IC80_4	0.91	90	20	22.0	68.0
37	SW480_WCL_IC90_1	1.02	90	20	19.6	70.4

38	SW480_WCL_IC90_2	1.04	90	20	19.2	70.8
39	SW480_WCL_IC90_3	1.20	90	20	16.6	73.4
40	SW480_WCL_IC90_4	1.21	90	20	16.5	73.5

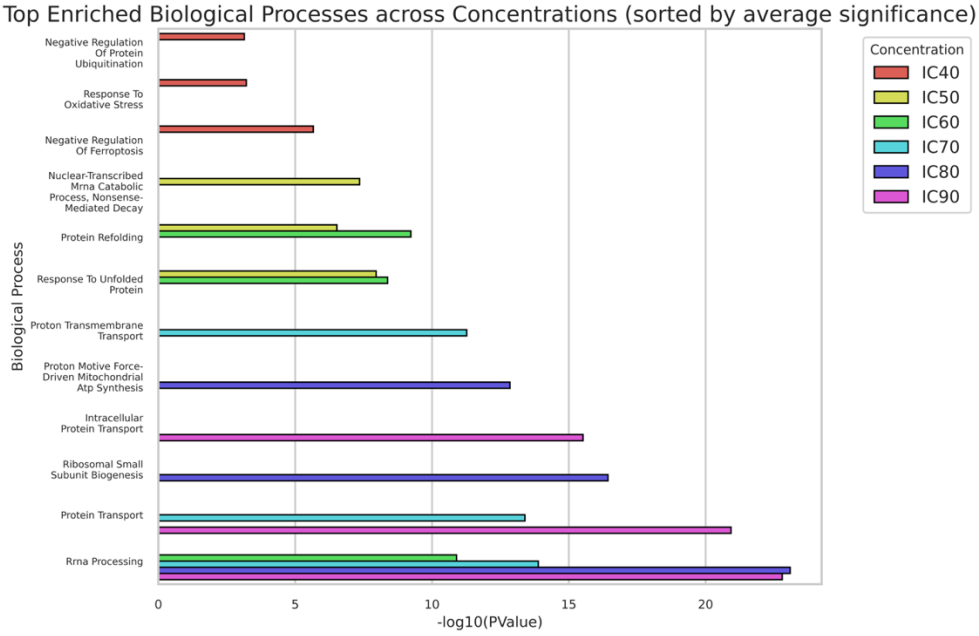

Figure 33: *Top enriched biological processes across IC40-IC90 sorted by average significance (upregulated proteins).*

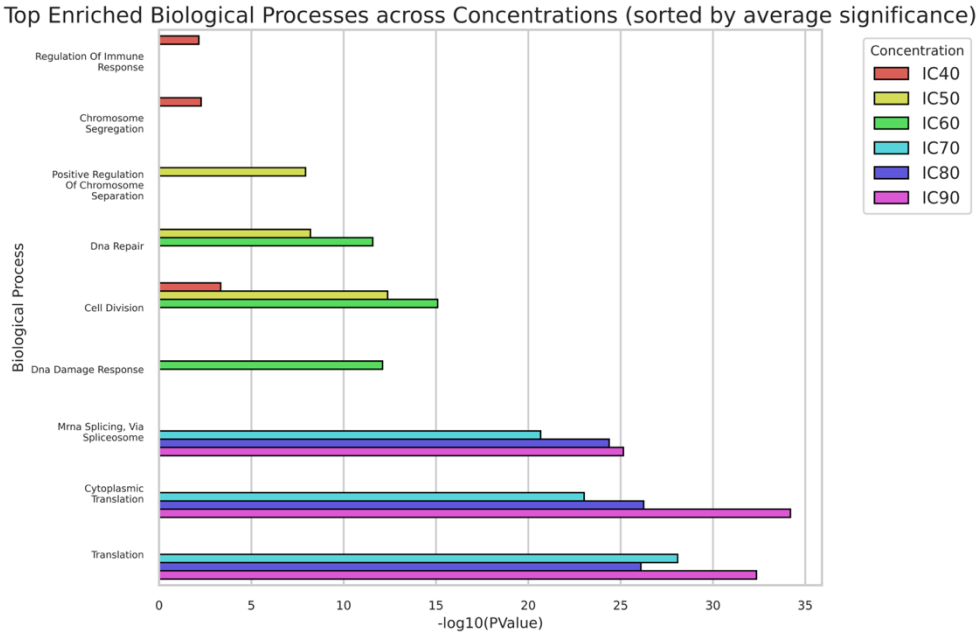

Figure 34: *Top enriched biological processes across IC40-IC90 sorted by average significance (downregulated proteins).*

Antagonism study

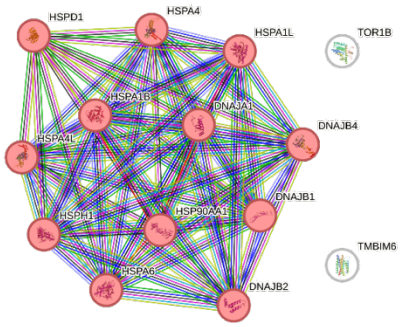

Figure 35: *String cluster of response to unfolded protein (gene count: 14. Combination treatment, WCL, significantly upregulated proteins, LFQ intensity higher in at least 5 out of 6 replicated than with other treatment).*

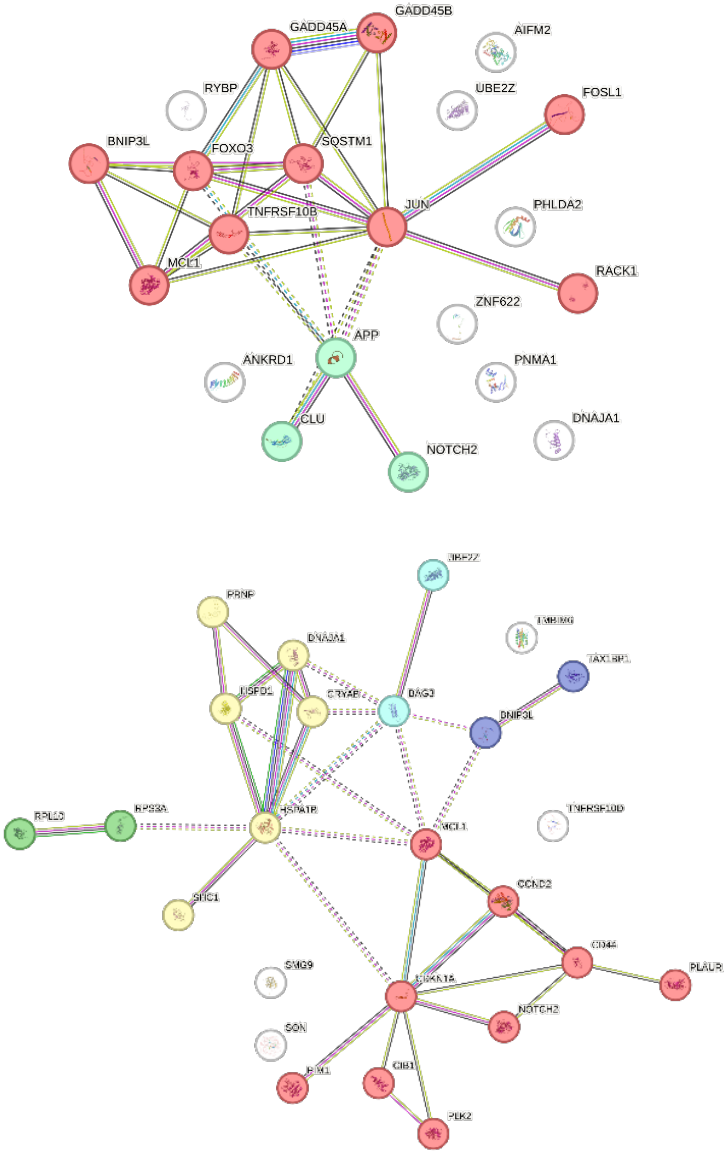

Figure 36: *Positive (top, gene count: 21) and negative (bottom, gene count: 25) regulation of apoptotic processes (combination treatment, WCL, significantly upregulated proteins, LFQ intensity higher in at least 5 out of 6 replicated than with other treatment).*

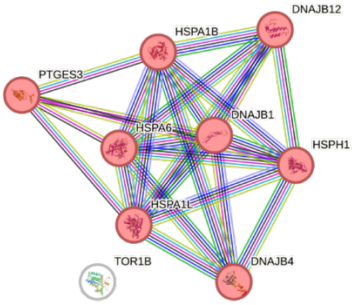

Figure 37: *Chaperone cofactor-dependent protein refolding (gene count: 9. Combination treatment, WCL, significantly upregulated proteins, LFQ intensity higher in at least 5 out of 6 replicated than with other treatment).*

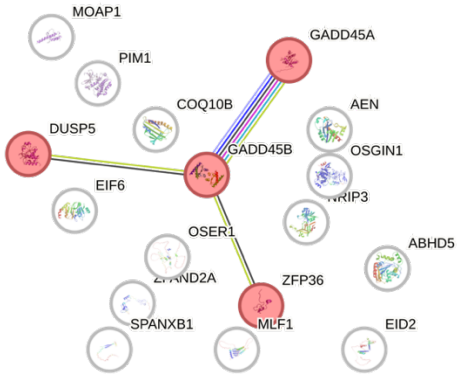

Figure 38: *Cluster of proteins present through combination therapy only.*

ROS-Assay data

Positive control with cells

Table 17: Data for the graphs created for ROS-Assay evaluation (positive control, triplicates, with cells).

Pos. control				
Conc.	**90 µM**		**200** µM	
Timepoint	Average	Std. dev.	Average	Std. dev.
00:00:00	1.2	0.1	1.2	0.2
00:10:00	1.3	0.2	1.4	0.3
00:20:00	1.5	0.2	1.9	0.4
00:30:00	1.7	0.3	2.2	0.5
00:40:00	1.8	0.3	2.4	0.6
00:50:00	1.9	0.3	2.6	0.6
01:00:00	2.0	0.3	2.7	0.6
01:10:00	2.0	0.3	2.7	0.6
01:20:00	2.1	0.3	2.8	0.5
01:30:00	2.1	0.3	2.8	0.5
01:40:00	2.1	0.3	2.8	0.5
01:50:00	2.1	0.2	2.7	0.5
02:00:00	2.1	0.2	2.7	0.4

ATO with cells

Table 18: Data for the graphs created for ROS-Assay evaluation (Arsenic trioxide, triplicates, with cells).

ATO								
Conc.	**5** µM / IC25		**50** µM / IC50		**120** µM / IC75		**200** µM / IC90	
Timepoint	Average	Std. dev.	Average	Std. dev.	Average	Std. dev.	Average	Std. dev.
00:00:00	1.2	0.4	1.0	0.6	1.1	0.6	0.9	0.5
00:10:00	1.2	0.3	1.0	0.5	1.0	0.5	0.9	0.4
00:20:00	1.2	0.4	1.0	0.5	1.0	0.6	0.9	0.5
00:30:00	1.2	0.4	1.0	0.5	1.0	0.6	0.9	0.4
00:40:00	1.2	0.4	1.0	0.6	1.0	0.6	0.9	0.5
00:50:00	1.2	0.4	1.0	0.6	1.0	0.6	0.9	0.5
01:00:00	1.2	0.4	1.0	0.6	1.0	0.6	0.9	0.5
01:10:00	1.2	0.4	1.0	0.6	1.0	0.6	0.9	0.5
01:20:00	1.2	0.4	1.0	0.6	1.0	0.6	0.9	0.5
01:30:00	1.2	0.4	1.0	0.6	1.0	0.7	0.9	0.5
01:40:00	1.2	0.4	1.0	0.6	1.0	0.7	0.9	0.5
01:50:00	1.2	0.4	1.0	0.6	1.0	0.7	0.9	0.5
02:00:00	1.2	0.4	1.0	0.6	1.0	0.7	0.9	0.5

Ir1 with cells

Table 19: Data for the graphs created for ROS-Assay evaluation (Ir1, triplicates, with cells).

Ir1								
Conc.	**20** µM / IC25		**45** µM / IC50		**80** µM / IC75		**90** µM / IC90	
Timepoint	Average	Std. dev.	Average	Std. dev.	Average	Std. dev.	Average	Std. dev.
00:00:00	1.2	0.4	1.4	0.3	1.5	0.5	1.6	0.5
00:10:00	1.3	0.3	1.6	0.3	1.8	0.4	2.1	0.5
00:20:00	1.6	0.4	2.1	0.4	2.5	0.7	3.0	0.8
00:30:00	1.8	0.5	2.5	0.5	3.1	0.9	3.6	1.0
00:40:00	2.0	0.6	2.8	0.8	3.5	1.2	4.1	1.3
00:50:00	2.2	0.8	3.0	0.9	3.9	1.4	4.5	1.5
01:00:00	2.4	0.9	3.3	1.1	4.2	1.5	4.8	1.7
01:10:00	2.6	1.0	3.5	1.2	4.5	1.7	5.0	1.8
01:20:00	2.7	1.1	3.6	1.3	4.6	1.7	5.2	1.9
01:30:00	2.9	1.2	3.8	1.4	4.8	1.8	5.3	1.9
01:40:00	3.0	1.3	3.9	1.5	4.9	1.9	5.4	2.0
01:50:00	3.0	1.3	4.0	1.6	4.9	1.9	5.4	2.0
02:00:00	3.1	1.4	4.0	1.7	5.0	1.9	5.4	2.1

Ir1 + ATO with cells

Table 20: Data for the graphs created for ROS-Assay evaluation (Ir1+ATO, triplicates, with cells).

Ir1 + ATO								
Conc.	**IC25 Ir1 + IC25 ATO**		**IC50 Ir1 + IC25 ATO**		**IC75 Ir1 + IC25 ATO**		**IC90 Ir1 + IC25 ATO**	
Timepoint	Average	Std. dev.	Average	Std. dev.	Average	Std. dev.	Average	Std. dev.
00:00:00	0.9	0.2	1.2	0.3	1.4	0.3	1.3	0.3
00:10:00	1.0	0.2	1.3	0.3	1.6	0.2	1.6	0.3
00:20:00	1.2	0.2	1.8	0.3	2.3	0.2	2.4	0.4
00:30:00	1.5	0.2	2.2	0.4	2.9	0.3	3.1	0.5
00:40:00	1.6	0.2	2.4	0.5	3.4	0.7	3.7	0.8
00:50:00	1.8	0.3	2.7	0.6	3.8	0.8	4.2	1.0
01:00:00	2.0	0.3	3.0	0.7	4.2	0.9	4.6	1.0
01:10:00	2.2	0.4	3.2	0.9	4.5	1.0	4.9	1.1
01:20:00	2.3	0.5	3.4	1.0	4.7	1.0	5.2	1.2
01:30:00	2.4	0.6	3.6	1.1	4.9	1.0	5.3	1.2
01:40:00	2.6	0.7	3.7	1.2	5.0	1.1	5.5	1.2
01:50:00	2.6	0.8	3.8	1.3	5.1	1.1	5.5	1.3
02:00:00	2.7	0.8	3.9	1.4	5.2	1.2	5.6	1.3

ATO without cells

Table 21: Data for the graphs created for ROS-Assay evaluation (ATO, technical triplicates, without cells).

ATO								
Conc.	**5** µM / IC25		**50** µM / IC50		**120** µM / IC75		**200** µM / IC90	
Timepoint	Average	Std. dev.	Average	Std. dev.	Average	Std. dev.	Average	Std. dev.
00:00:00	1.9	0.2	16	0.1	1.5	0.0	1.5	0.0
00:10:00	1.9	0.2	1.7	0.0	1.6	0.0	1.6	0.0
00:20:00	1.6	0.1	1.4	0.0	1.4	0.0	1.4	0.0
00:30:00	1.4	0.1	1.3	0.0	1.3	0.0	1.3	0.0
00:40:00	1.3	0.1	1.2	0.0	1.2	0.0	1.2	0.0
00:50:00	1.2	0.0	1.2	0.0	1.1	0.0	1.1	0.0
01:00:00	1.2	0.0	1.2	0.0	1.1	0.0	1.1	0.0
01:10:00	1.3	0.0	1.2	0.0	1.1	0.0	1.1	0.0
01:20:00	1.2	0.0	1.2	0.0	1.1	0.0	1.1	0.1
01:30:00	1.3	0.0	1.2	0.1	1.1	0.0	1.1	0.1
01:40:00	1.3	0.0	1.2	0.1	1.1	0.1	1.1	0.1
01:50:00	1.3	0.0	1.2	0.1	1.2	0.1	1.1	0.1
02:00:00	1.3	0.0	1.2	0.1	1.2	0.1	1.2	0.1

Ir1 without cells

Table 22: Data for the graphs created for ROS-Assay evaluation (Ir1, technical triplicates, without cells).

Ir1								
Conc.	**20** µM / IC25		**45** µM / IC50		**80** µM / IC75		**90** µM / IC90	
Timepoint	Average	Std. dev.	Average	Std. dev.	Average	Std. dev.	Average	Std. dev.
00:00:00	3.2	0.1	3.5	0.2	4.7	0.3	4.4	0.2
00:10:00	3.3	0.2	3.9	0.2	4.9	0.2	5.0	0.1
00:20:00	3.6	0.1	4.3	0.2	5.5	0.2	5.6	0.1
00:30:00	3.9	0.1	4.7	0.2	6.3	0.1	6.3	0.1
00:40:00	4.2	0.1	5.1	0.2	6.7	0.2	6.8	0.2
00:50:00	4.5	0.1	5.6	0.2	7.2	0.2	7.4	0.2
01:00:00	4.7	0.1	5.9	0.2	7.5	0.2	7.8	0.2
01:10:00	4.8	0.2	6.1	0.3	7.7	0.3	8.0	0.2
01:20:00	4.9	0.2	6.3	0.3	7.9	0.3	8.3	0.2
01:30:00	4.9	0.2	6.4	0.3	7.9	0.3	8.3	0.1
01:40:00	4.9	0.2	6.5	0.2	7.9	0.2	8.3	0.1
01:50:00	4.9	0.1	6.5	0.2	7.9	0.2	8.3	0.2
02:00:00	3.2	0.1	3.5	0.2	4.7	0.3	4.4	0.2

Ir1 + ATO without cells

Table 23: Data for the graphs created for ROS-Assay evaluation (Ir1+ATO, technical triplicates, without cells).

Ir1 + ATO								
Conc.	**IC25 Ir1 + IC25 ATO**		**IC50 Ir1 + IC25 ATO**		**IC75 Ir1 + IC25 ATO**		**IC90 Ir1 + IC25 ATO**	
Timepoint	Average	Std. dev.	Average	Std. dev.	Average	Std. dev.	Average	Std. dev.
00:00:00	0.7	0.0	0.8	0.0	0.8	0.0	0.8	0.1
00:10:00	1.4	0.1	1.4	0.2	1.7	0.2	1.9	0.2
00:20:00	2.1	0.2	2.4	0.2	3.0	0.2	3.3	0.3
00:30:00	2.9	0.1	3.2	0.2	4.2	0.2	4.5	0.3
00:40:00	3.5	0.1	3.9	0.2	5.0	0.2	5.5	0.3
00:50:00	4.1	0.1	4.6	0.3	5.9	0.3	6.4	0.3
01:00:00	4.6	0.2	5.1	0.3	6.4	0.3	7.0	0.3
01:10:00	4.9	0.2	5.4	0.3	6.8	0.3	7.4	0.3
01:20:00	5.2	0.2	5.8	0.3	7.2	0.3	7.8	0.3
01:30:00	5.3	0.1	6.0	0.3	7.3	0.3	7.9	0.2
01:40:00	5.4	0.1	6.1	0.3	7.4	0.3	7.9	0.2
01:50:00	5.5	0.1	6.2	0.3	7.5	0.3	8.1	0.2
02:00:00	0.7	0.0	0.8	0.0	0.8	0.0	0.8	0.1

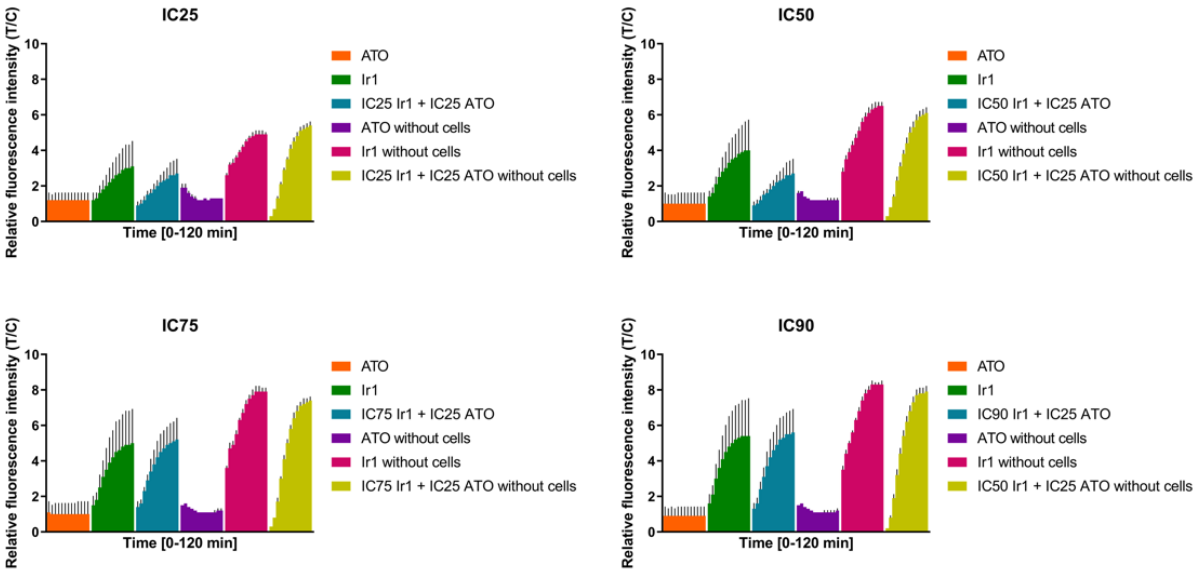

Figure 39: *Comparison of ROS intensities from cell-containing and cell-free assays.*

Abbreviations

(u/nano)HPLC	(Ultra/Nano)High-Performance Liquid Chromatography
1C-metabolism	One-Carbon metabolism
4-HNE	4-hydroxynonenal
ABHD5	Alpha/beta-hydrolase domain-containing protein 5
AKR	Aldoketo reductases
ALDH	Aldehyde dehydrogneases
APL	Acute promyeloxytic leukemia
ATO	Arsenic trioxide
ATRA	All trans retinoic acid
BHMT	Betaine-Homocysteine Methyltransferase
BIK	Bax-inhibitor
CBS	Cystathionine-β-synthase
CI	Combiantion index
CID	Collision-induced dissocitation
CO2	Carbondioxide
CON	Control
CV	Coefficient of Variation
CYCS	Cytochrome c, somatic
DCFH-DA	2',7'-dichlorodihydrofluorescein diacetate

DCOONa	Deuterated sodium formate
DDA	Data dependent acqusition
DDSs	Drug delivery systems
Deact	Deacitvation
DIA	Data independent acqusition
DMSO	Dimethyl sulfoxide
DNA	Deoxribonucleic acid
DNAJA3	DnaJ homolog subfamily A member 3
DNAJB1	DnaJ homolog subfamily B member 1
DUSP5	Dual-Specificity Phosphatase 5
E	kinetic energy
EC	Effective concentration
EDTA	Ethylenediaminetetraacetic aci
EGR1	Early growth response protein 1
EICs	extracted ion chromatograms
EID2	EP300 Interacting Inhibitor Of Differentiation 2
EIF6	Eukaryotic Initiation Factor 6
Eppi	Eppendorf vial
ER	Endoplasmic reticulum
FasL	Fas ligand

FoxO	Forkhead-Box O
FBS	Fetal bovine serum
FoxO3a	Forkhead-box O3a
GADD45A	Growth Arrest and DNA-Damage-Inducible 45 Alpha
GADD45B	Growth Arrest and DNA-Damage-Inducible protein 45 beta
GSH	Glutathione
H_2O	Water
HBSS	Hank's Balanced Salt Solution
HCOONa	Sodium formate
HEPES	4-(2-hydroxyethyl)-1-piperazineethanesulfonic acid
HKDC1	Hexokinase domain containing 1
HMOX1	Heme Oxygenase-1
HSP	Heat-shock protein
HSPA6	Heat Shock Protein Family A Member 6
IC	Inhibitiory concentration
Ir	Iridium
KCl	Potassium chloride
KH_2PO_4	Potassium Dihydrogen Phosphate
LC	Liquid chromatography
LFQ	Label free quantification

m	mass
m/z	Mass to charge
MAPK	Mitogen-Activated Protein Kinase
MEM	Minimum Essential Medium Eagle
MLF1	Myeloid Leukemia Factor 1
MOAP1	Modulator of Apoptosis 1
MS	Mass Spectrometry
MTT	[3-(4,5-dimethylthiazol-2-yl)-2,5-diphenyltetrazolium bromide]
Na_2HPO_4	Sodium Hydrogen Phosphate
NaCl	Sodium chloride
NADH	Nicotinaminde adenine dinucleotide
NaOH	Sodium hydroxide
NF-kB	Nuclear Factor kappa-light-chain-enhancer of activated B cells
NH_4OH	Ammonium Hydroxide
NRF2	Nuclear Factor Erythroid 2-Related Factor 2
NRIP3	Nuclear Receptor Interacting Protein 3
OSER1	Oxidative Stress-Responsive Serine-Rich Protein 1
OSGIN1	Oxidative Stress-Induced Growth Inhibitor 1
PASEF	parallel accumulation-serial fragmentation
PBS	Phosphate-Buffered Saline

PDT	Photodynamic Therapy
PenStrep	Penicillin-Streptomycin
PGM1	Phosphoglucomutase 1
PIC	Phosphatase inhibior cocktail
PMSF	Phenylmethylsulfonyl fluoride
PPP	Pentose-Phosphate Pathway
PTT	Photothermal Therapy
Ras-ERK	Ras-Extracellular signal-regulated kinase
RASP	Reactive aldehyde species
ROS	Reactive oxygen species
rpm	Rotations per minute
RT	Room temperature
Rxn	Reaction
s.d.r.	Significantly downregulated
s.r.	Significantly regulated
s.u.r.	Significantly upregulated
SDC	Sodium deoxycholate
SIMCats	Small molecule intracellular metal catalysts
SLC2A1	Solute Carrier Family 2
SPANXB1	Sperm Protein Associated with the Nucleus on the X Chromosome B1

TBHP	Tertbutylhydroxyperoxide
TCEP	Tris(2-carboxyethyl)phosphine
tims	Trapped ion mobility mass spetrometer
TKTL1	Transketolase-like-1
TMBIM6	Transmembrane Bax Inhibitor Motif-containing 6
TNF	Tumor necrosis factor
TOF	time-of-flight
TP53	Tumor Protein p53
TRAP1	NF receptor-associated protein 1
Tris-HCl	Tris(hydroxymethyl)aminomethane - Hydrochloride
TYMS	Thymidylate Synthase
UPR	Unfolded protein response
v	Velocity
ZFAND2A	Zinc Finger AN1-Type Containing 2A
ZFP36	Zinc finger protein 36
ZIP	Zero interaction potency

In the course of this thesis, the AI language model, deepL, was utilized to assist in achieving the provided written English style.

Python scripts used to generate some of the graphs in this thesis were corrected and reviewed with the help of the AI model ChatGPT.